Photoelectrode design principles for efficient photo-charging of solar redox flow batteries

In partial fulllment of the requirements for the degree of

Master of Science
Sustainable Energy Technology

Gerasimos Kanellos

September, 2019

Materials for Energy Conversion and Storage, Faculty of Applied Sciences,
Delft University of Technology

Graduate
Gerasimos Kanellos (4718453)
MSc Sustainable Energy Technology
Faculty of Electrical Engineering, Mathematics and Computer Science (EEMCS), Delft University of Technology
gerasimos.kanellos@gmail.com

SET3901 Graduation Project: Department of Materials for Energy Conversion and Storage, Faculty of Applied Sciences

Supervisors
Assoc. Prof. Dr. Wilson A. Smith
Dr. Dowon Bae

Msc Thesis Committee
Prof. Dr. Bernard Dam, TU Delft (MECS group)
Prof. Dr. Fokko Mulder, TU Delft (MECS group)
Assoc. Prof. Dr. Arjan J. Houtepen, TU Delft (OM group)

List of original publications
This thesis is partly based on the following original publications, which have been published, accepted, submitted or prepared for publication and are cited throughout the text with Latin numbers.

I D. Bae, G. M. Faasse, G. Kanellos, W. A. Smith, "Unravelling the practical solar charging performance limits of redox flow battery based on the single photon device system", *Sustainable Energy & Fuels*, 3, 2399–2408, 2019.

II D. Bae, G. Kanellos, G. M. Faasse, E. Drazevic, A. Venugopal, W. A. Smith, "Design principles for efficient photoelectrodes in solar rechargeable redox flow battery applications", *Submitted*.

III D. Bae, G. Kanellos, W. A. Smith, "Composition controlled MoOx and effect on energy-level alignment with n-GaP", *Under process for publication*.

Preface

The basis for this research originated from my passion for the field of electrochemistry. During my search for a suitable thesis topic, i focused on the field of sustainable energy storage. Therefore, Materials for Energy Conversion and Storage (MECS) at the Delft University of Technology was the ideal option to contribute to research in an interesting and growing field, as well as further develop my skills. Considering that my thesis topic would also involve research in semiconductors for photoelectrochemical purposes, I was enthralled by the opportunity to apply my theoretical knowledge gained from my M.Sc. "Solar Energy" specialization combined with "Energy Storage" applications.

Photoelectrochemical cells coupled with battery storage envelope multiple disciplines, like electrochemistry, semiconductor physics, materials science as well as physical chemistry and kinetics. This thesis was therefore a real challenge, but also a great opportunity to achieve personal growth and deeper understanding of various processes. In truth, I would be unable to attain this positive outcome without a strong, supporting group. First of all, my family, for their love and patience throughout the years of my studies, which they made possible and supported in every step. Special gratitude to my supervisor, Dr. Dowon Bae, for all his daily help, support and advice throughout the experiments and for how much i learned from him during this learning process. I would also like to express my appreciation to my supervisor, Wilson A. Smith, for making this opportunity possible and for his support over the course of my thesis project, as well as my committee members Dr. B. Dam, Dr. F. Mulder and Dr. A. J. Houtepen, each of whom provided interesting insight into my research. Last but not least, I want to thank all the people and support staff within the MECS research group, for the useful advice, the chats during the coffee breaks and the nice atmosphere.

Abstract

In connection with attempts to increase the Solar Redox Flow Battery (SRFB) viability, an investigation was done into the charge carrier transport mechanisms entailed at the photoelectrode interlayer interfaces. On the basis of a preliminary study, the investigation focused on the development of a suitable conducting layer at the electrolyte/electrode interface as well as the development and control of a hole extraction layer, based on the device electronic structure and energy levels matching.

Research was conducted into the properties of various prospective materials that could improve charge carrier transport at the electrolyte/photoelectrode interface. Once the optimal configuration is determined, the photoelectrode and redox couples are prepared and characterized and the photocharging performance of the device is optimized. Furthermore, the control of the formation conditions of a hole extraction layer took place, in order to yield improved internal charge carrier separation and transport. Various hole transport layers were assessed in SRFB system in relation to the photo-charging performance.

The described process resulted in the development of a conducting layer through the growth of well distributed islands, which led to a high solar-to-chemical conversion of 9.4%. Through the control of the formation conditions of the hole extraction layer, better spatial separation of the photogenerated charge carriers was achieved, leading to improved device performance. Despite the enhanced viability of each device in terms of efficiency, further research into the long-term stability is essential for its practical implementation. This mainly relates to electrolyte degradation to form solid precipitates and photocorrosion of the absorber semiconductor materials in acidic conditions.

Contents

Nomenclature

Abbreviations

$SRFB$	Solar redox flow battery
RFB	Redox flow battery
PEC	Photoelectrochemical cell
SOC	State of charge
AM	Air mass
SRH	Shockley-Read-Hall (recombination)
BPA	Back-side photoanode
BPC	Back-side photocathode
FPA	Front-side photoanode
FPC	Front-side photocathode
FF	Fill factor
HTL	Hole transport layer
ETL	Electron transport layer
TCO	Transparent conducting oxide
KE	Kinetic energy
BE	Binding energy
CA	Chronoamperometry

Latin letters

E_{photon}	Photon energy [eV]
v	Photon frequency [Hz]
$I_{e\lambda}$	Spectral irradiance [Wm^2]
E	Energy density [Ah/L]
z	Number of electrons involved in reaction [-]
C	Concentration [mol L^{-1}]
E_{cell}	Cell potential at non-standard state conditions [V]
E^0_{cell}	Standard state cell potential [V]
T	Temperature [K]
P_{max}	Maximum power [W]
V_{oc}	Open circuit voltage [V]

J_{sc}	Short circuit current [mA cm^{-2}]
I_{in}	Incident irradiance [Wm^2]
n	Efficiency [-]
I_{in}	Incident irradiance [Wm^2]
J_0	Reverse saturation current density [mA cm^{-2}]
n_i	Intrinsic carrier concentration [cm^{-3}]
D	Diffusion coefficient [m$^2 s^{-1}$]
L	Diffusion length [m]
N	Particle density [m^{-3}]
E_i	Energy [eV]
V_{bi}	Built-in voltage [eV]
N	Doping concentration [cm^{-3}]
l	Depletion region width [m]
W	Total depletion region width [m]
$n(x)$	Electron density [C m^{-3}]
$p(x)$	Hole density [C m^{-3}]
A	Absorbance [-]
T	Transmittance [-]
R	Reflectance [-]
a	Optical absorption coefficient [m^{-1}]
d	Sample thickness [m]
m	Diffraction order [m^{-1}]
C_c	Interface capacitance [F]
V_f	Flat band potential [V]
N_i	Effective density of states [eV]

Greek letters

λ	Wavelength [m]
$\Phi_{ph}(\lambda)$	Spectral photon flux [m$^2 s^{-1}$]
ϵ_i	Material relative permittivity [-]
ξ	Electron affinity [kJ mol^{-1}]
ϕ	Work function [J]
τ	Charge carrier lifetime [s]
θ	Bragg's angle [°]
μ	Carrier mobility [cm$^2 V^{-1} s^{-1}$]
$\Xi(x)$	Electric field distribution [Vm^{-1}]
ρ	Charge density [C m^{-3}]

Subscripts

0	in vacuo
C	conduction band
V	valence band
G	band gap
F	fermi level
d	donor
a	acceptor

Constants

e	Elementary charge [C]
R	Gas constant [J $\mathrm{mol}^{-1} K^{-1}$]
h	Planck constant [$\mathrm{m}^2 kgs^{-1}$]
k_B	Boltzmann constant [$\mathrm{m}^2 kgs^{-2} K^{-1}$]
ϵ_0	Vacuum permittivity [F m^{-1}]
F	Faraday constant [As mol^{-1}]

List of Figures

List of Tables

1. Introduction

In this chapter an introduction alongside the fundamental theoretical background is provided in order to have a better understanding of the work done during this thesis. Firstly, an introduction on the energy challenge is given followed by the incentive for this research. Finally, the ultimate objectives are presented along with the research questions of this work.

1.1 The Energy Challenge

Until the 19th century, society covered its energy needs by using exclusively renewable energy sources such as wind, hydro and geothermal energy. With the industrial revolution, however, fossil fuels, namely coal, oil, gas, have become the primary forms of energy for human society and the economy. The rapid development of technology has resulted in the direct dependence of mankind on it and consequently on the non-renewable energy sources on which modern technology was built. Over time and the proliferation of industrialization, energy needs have multiplied and new problems have emerged. These concern the depletion of mineral reserves, the impact on the environment of the use of fossil fuels as well as the fluctuations in their prices and the socio-political problems caused by their claim. These problems make immediate the need for substitution with alternative, renewable forms of energy before exhaustion.

Out of several initiatives that have emerged regarding the promotion of renewable energy sources [4], the Paris agreement stands out, being a global response to climate change indications and setting a long-term goal to maintain the increase of the average global temperature below 2°C above the pre-industrial levels [5]. Nonetheless, there exist multiple factors that squander this ultimate objective. It is projected that the world population will surpass 10 billion by 2050, an increase that is attributed mostly to a small number of countries in Asia and Africa [6]. This is estimated to result in an increase of the global energy demand by more than a quarter, surpassing 800 quadrillion Btu annually [7, 8]. Moreover, early stage industrialization of the developing countries has led to higher and rapidly rising shares of anthropogenic greenhouse gas (GHG) emissions compared to that of industrialized countries [9]. In order for the Paris agreement to be implemented, the energy scheme has to tackled the root cause and change drastically, based on key pillars for coordinated progress. These can be new policy implementations in favor of renewable sources, a shift towards local energy generation, microgrids development and electricity grid infrastructure overhaul. The incorporation of renewable energy sources, specifically solar, wind, biomass and geothermal, into the existing grid has already been inaugurated, in order to meet the increasingly high energy demand while keeping the GHG emissions rates at their present value. It is expected that energy generated from these sources will reach 12.4% of the global energy demand by 2023 [10]. Specifically, photovoltaics have followed an exponential increase in their installed capacity over the past years and are expected to lead the renewable electricity market in the near future, since solar energy is the most abundant energy resource of the planet (Figure 1). Nevertheless, the intermittency of renewable energy sources presents a vital complication for their effective integration with the existing electricity grid. The only way to ensure flexibility, reliability and non-volatility of the grid while reducing carbon emissions, is to incorporate another balancing capacity technology, that will act as the grid stabilizer and provide security of supply.

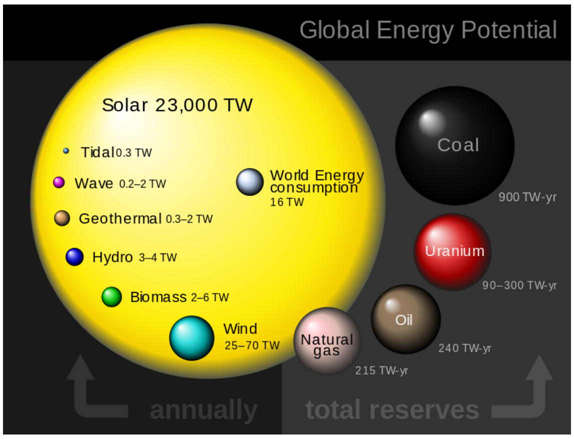

Figure 1: The finite and renewable energy reserves of the planet [11].

Energy storage already exists in many forms, such as pumped hydroelectric storage plants, which make up for more than 95% of worldwide current storage capacity [12]. However, the environmental impacts, the vast land-use, which is already confined by hydrology dependency and natural habitats deformation, as well as the high cost associated with such plants, restrict their expansion. On the other hand, research has been strongly directed towards battery storage, considering the fact that their cost declines fast and that they become economically competitive with natural gas peaking plants [13]. The technological improvements, the revocation in their economic limitations and their ability to cover for fluctuations has made electricity storage in batteries the most promising means to store energy [7, 13].

1.2 Motivation

In order for photovoltaics to be practically integrated into the grid, there is a need for high conversion efficiency, as well as large-scale energy storage to cover for their intermittent nature. Many attempts have been made to incorporate photoelectrochemical (PEC) cells to current electricity generating technologies, in order to convert electricity directly to chemicals. Most common and widely studied examples are PEC water electrolysis [14], carbon dioxide reduction [15] or other solar fuels production using artificial photosynthesis [16, 17]. However, after several years of research, these methods and devices have only been exploited in a quite limited capacity, mainly due to overpotential related losses, which results in low conversion efficiency and high cost and therefore restrains their market viability.

In the context of solar energy increased utilization and leading role in the near future, coupled with the need for an effective electricity storage system to cover the daily fluctuations, solar redox flow batteries (SRFBs) have received an increasing amount of attention over the last few years. The architectural concept of the SRFB is a combination of a redox flow battery (RFB) and a PEC or PV-assisted device, which may be fully integrated into a single cell or separated into an RFB and a solar charging component (Figure 2). The process involved is the conversion of solar energy into a chemical fuel in the form of soluble and reversible redox couples, which can be converted back to electricity during a period of scarcity. The conversion step of solar energy to the redox couples is achieved by the illumination of at least one photoelectrode, which is submerged in at least one of the redox couples. Consequently, photoexcited charge carriers are generated from the semiconductor, separated towards different contact points and subsequently reduce or oxidize the dissolved redox species of the electrolyte [18]. The charged species are then stored until there is a need for excess energy, in which case they are discharged like being in a normal RFB.

The SRFB is a simple and promising system for simultaneous solar energy conversion and storage. Such a system has multiple advantages compared to conventional water splitting devices. Firstly, it has the potential to be incorporated in any energy market, from improving grid power quality (UPS) to bulk power management [19]. This is because the SRFB shares similar features as the RFB's, one of which is the ease of scalability in energy output, just by increasing the electrolyte volume in the tanks. In addition, compared with the separate solar energy conversion and storage devices, the SRFB skips the step of electricity generation and has less capital costs due to less balance of systems (BOS) requirements [20]. Furthermore, the most prominent advantage of this system is its flexibility on redox couples [21] and photoabsorber materials [22] that can be employed in multiple combinations between them, in order to achieve the optimal result.

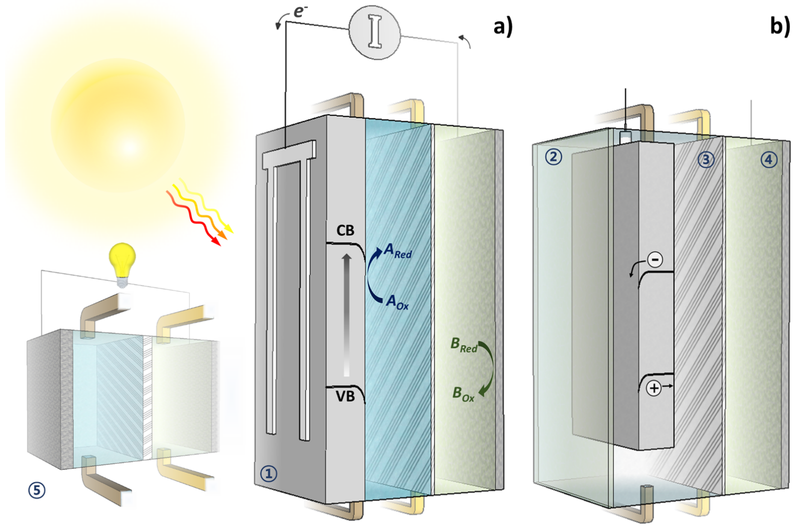

Figure 2: Schematic of solar charging compartments for SRFB system. (a) Charging cell with a back-side illuminated device and (b) cell with front-side illuminated device (i.e., illuminated through the window (2) and the electrolyte). Photocathode (1) in the catholyte (with redox couple A) and an polarizable counter electrode (4) in the anolyte (with redox couple B) are separated by an ion exchange membrane (3). In practical applications, RFB stack (5) is connected in series with storage tanks and pumps (not shown) for discharging the solar charged electrolytes. Subscripts (Ox and Red) denote the oxidized form and reduced form of the redox couples. CB and VB correspond to the conduction and valence band edges of the semiconductor, respectively. Note that the illustration is not to scale.

Despite the long research history since 1976 by Hodes et al.,[23] a lot of effort has been demonstrated relatively recently [22, 24–28], after research of PEC water splitting technologies grew. This resulted in the incorporation of PV materials in electrochemical applications. The main advantages of SRFB's compared to conventional PEC water, is that it offers flexibility with respect to redox couples employed and solubility in a wide pH range. In addition, the use of various organic chemicals has been demonstrated in recent studies, where they were combined with conventional inorganic redox chemicals, which results in an unprecedented wide selection of redox energy level matching with photovoltage for the charging reaction [18, 29, 30]. However in every case, the main drawback is the relatively low solar-to-chemical efficiency (i.e., charging efficiency, STC% hereinafter). The highest solar-to-output electricity was achieved by Li et al., where a 14.1% efficiency was recorded utilizing a single photon device combined with high cell voltage [31]. Apart from the single photon devices, there have been reports of an integrated system with photo-anode and -cathode, immersed into the PEC charging cell in dual-bed or tandem device configuration (2-photon-device). This leads to increased photovoltage that is sufficiently enough for the redox couples with high cell voltage (≥ 0.8 V) [25–27]. Most recently, Urbain et al. published a record-breaking STC% (12.3%) using a monolithic tandem a-Si/a-Si PV-assisted device which showed high photovoltage (2 V) owing to its wide bandgap (c.a. 1.95 eV) [26]. Nonetheless, the 2-photon-device approach is cost-advantageous only when both photo-absorbers have an ideal band-gap pairing [32]. Another critical challenge is the demonstration of a wide band-gap top cell with a cost below $\$100m^{-2}$ with an efficiency above 20% which is essential for having a lower LCOE (Levelized cost of electricity) than that of single-photon-device[32, 33].

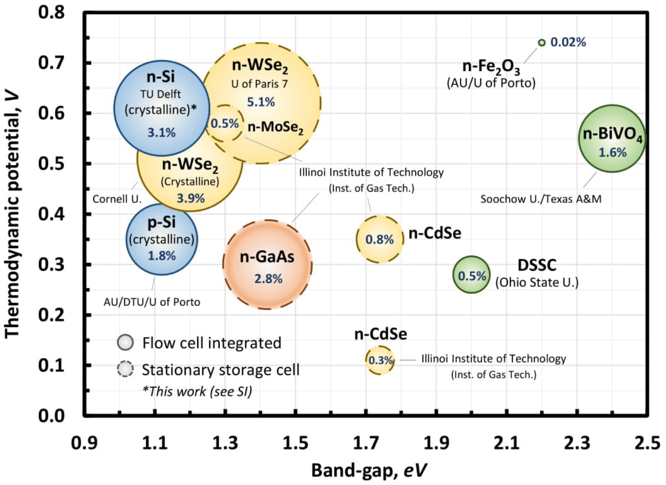

Figure 3: Experimental STC% of several solar-chargeable cells are shown at different combinations of photo-absorber band-gap and thermodynamic potential (defined as the difference between the redox potential of the respective oxidation and reduction couples) (I).

As shown in Figure 3, some studies demonstrated meaningful charging efficiency using a $n-WSe_2$ [34, 35]. However, those references used a stationary redox chemical cell with a non-standard light source (e.g., He-Ne laser; 150 mW cm^{-2}). McKone and co-workers [28] have demonstrated an SRFB in accordance to its real meaning under the standard light condition. The home-made crystalline WSe_2 was used for charging an RFB with NaI and AQDS(2,7) redox couples with a cell voltage (Vcell) of 0.46 V with an STC% of 3.9%, which is one of the highest values among the SRFBs with unbiased single PEC device [28]. Interestingly, examples with already proven PEC materials, such as c-Si, $BiVO_4$, DSSC, and etc. [22, 36–38] exhibited quite low charging efficiency ($\leq 2\%$). For the sake of consistency, all STC% data are calculated using the light-driven photocurrent measured at a 0% state of charge (SOC%). For an ideal case, which is well known as the Shockley-Queisser limit, one would expect an theoretical maximum efficiency up to around 33%. However, Figure 3 shows that charging efficiencies are far from this maximum. Even though there is a precondition of sufficient solubility of the redox couples to balance the energy storage capacity, there remains substantial room for improvement considering the gap between performances of the SRFB with a single-photon-device and state-of-the-art PV cell technology. The performance of the stationary redox cells in Figure 3 alone, also highlights the experimental potential of the SRFB. In this respect, modeling the theoretical conversion efficiency for PEC device of the SRFB is useful as it can identify practical performance limit and aspects of material properties that need to be enhanced. A number of previous studies have addressed theoretical performance limit for both single- and 2-photon PEC water splitting devices [39–42].

To recapitulate, the integrated SRFB device has attracted a lot of attention for its great potential in many applications. Several parameters still need to be optimized in order for it to be rendered viable and achieve industrialization and commercialization. Several negative effects, such as electrolyte parasitic absorption, can be hindered by using different configurations, stability issues can be improved by applying better surface passivating/-catalytic layers and the energy levels between the photoelectrode and the redox couples need to be tuned flawlessly. In addition, the vast technical breakthroughs in the field of photoelectrodes and flow batteries can be utilized and combined in a suitable way to yield the optimal results.

1.3 Research Objectives

The ultimate objective of this thesis is twofold. First, the fabrication of a Si-based photoelectrode, to understand fundamental aspects of interfaces between the photoelectrode and the electrolyte, as they pertain both to electric conductivity and energy level matching of the surface, for maximization of photocharging efficiency. Secondly, the design and fabrication of a high photovoltage SRFB device, based on GaP, to study the efficient charge carrier generation, separation and transport through a hole selective transport layer incorporated in order to maximize the photocurrent output. In both cases, the photoelectrodes are employed for the photocharge of their respective dissolved redox species, based on energy levels matching, without applying any external bias.
The main research questions for this thesis are :

- How the charge carrier transport takes place at the thin film interfaces and the development of a suitable catalytic/conducting layer.
- How to achieve high photovoltage and increase photocurrent output utilizing a hole selective thin transport layer coupled with GaP main absorber semiconductor.
- What is the influence of the deposition parameters on the thin film layers in terms of charge extraction efficiency, circumventing recombination and preventing efficiency losses.
- The suitable electrolyte selection and characterization, for each respective photoelectrode based on energy levels matching.
- The SRFB optimal configuration and electronic structure for maximizing stability, photocurrent output and charging efficiency.

1.4 Thesis Outline

The work of this thesis is partly based on the original research papers which have been published, accepted, submitted or prepared for publication and are listed in the approval page.

The layout of the report is as follows. Chapter 2 presents the theoretical background required for understanding the concept of the Solar Redox Flow Battery. The properties of semiconductor materials and electrochemical systems are introduced and the appropriate energy levels matching between them is explained. In addition, the main charge transfer mechanisms between different layers are described and the recombination processes are reported. In Chapter 3, the experimental methods followed are provided. Firstly, the photoelectrode fabrication process is described and the processing techniques are shown in detail, with additional information about the equipment employed for the photoelectrodes characterization. Secondly, the sample preparation procedures and cell configuration are described for the respective experiments employing the single or dual-chamber photoelectrochemical cell. In chapter 4, the results are shown for the two different semiconductors employed (Si and GaP), including characterization of catalytic/conducting layer, charge carrier selective transport layers, electrolyte characterization and photocharging performance. Chapter 5 discusses the experimental results and some practical considerations are reported about the devices. Furthermore, an outlook of the possible ways to further improve the photocharging efficiency is given, which provides some necessary points to guide future research. This report is concluded in chapter 6, with a summary of the most important inferences about the implemented systems and how the ultimate objectives of this thesis work are achieved.

2. Theoretical framework

This chapter aims to introduce the fundamental concepts of semiconductor physics and electrochemical systems. A theoretical outline of the semiconductor materials properties are presented and their integration with energy storage devices is discussed. In addition, the operating principle of the Solar Redox Flow Battery is described and further insights are reported in order for the photoelectrochemical system to be properly designed, including energy levels matching, charge carrier transport and recombination mechanisms.

2.1 The Solar Redox Flow Battery

The Solar Redox Flow Batteries (SRFB's) are integrated devices of a PEC and an RFB, for conversion of solar energy and simultaneous storage. It is considered a more direct, efficient and cost-effective system for solar energy utilization [31]. There exist three different operating modes which can be interchanged based on the context that the SRFB will be utilized. These include the normal RFB operation mode for discharging of the redox active species, providing energy during scarcity periods, the normal photovoltaic solar cell operation mode for direct conversion of solar radiation to electricity and finally, the SRFB operation mode for solar energy harvesting and consequently storage in the form of charged redox species. In addition, employing the right electrodes and system configuration, simultaneous charging and discharging of the redox active species is possible, making it a suitable system for energy supply and demand management.

2.1.1 Solar energy

Due to the intermittent nature of solar energy, it is necessary to employ both high efficiency solar energy conversion devices, as well as storage systems to store and release energy when required. It is the most abundant and major renewable energy source and can meet the constantly increasing global energy demand in an efficient and sustainable way. It has been reported that the potential of incident solar radiation can reach up to 23.000 TWy per annum, compared with a mere 19 TWy per annum which has been reported to be the world's yearly energy needs [43]. Due its great potential, solar energy has been established as the most promising energy source to cover future energy needs. Correspondingly to solar cells, SRFB's can either convert solar energy directly to electricity by means of the photovoltaic effect, or convert solar energy to stored charged redox species by means of the photoelectric effect. In either case, it serves as an effective and versatile system to utilize and simultaneously store solar energy. The photoelectric effect can be interpreted by describing light as well defined quanta, the photons. The photon's energy is:

$$E_{photon} = hv = \frac{hc}{\lambda} = \frac{1.2398}{\lambda / \mu m} eV \tag{1}$$

Where h is Planck's constant equal to $6.62607004 \cdot 10^{-34} m^2 kg s^{-1}$, v is the frequency of the light, c is the speed of light in vacuum equal to $299792458 ms^{-1}$ and λ is the wavelength of the wave. [44]. It is also important however to state how the solar energy spectra is distributed based on the photons' energy. The majority of the solar radiation (51.7%) lies in the near infrared region (700-3500 nm), 38.3% in the visible region (400-700 nm) and finally 8.7% lies in the ultraviolet region (200-400 nm) [45]. The corresponding electromagnetic frequency spectrum can be seen can be seen in Figure 4.

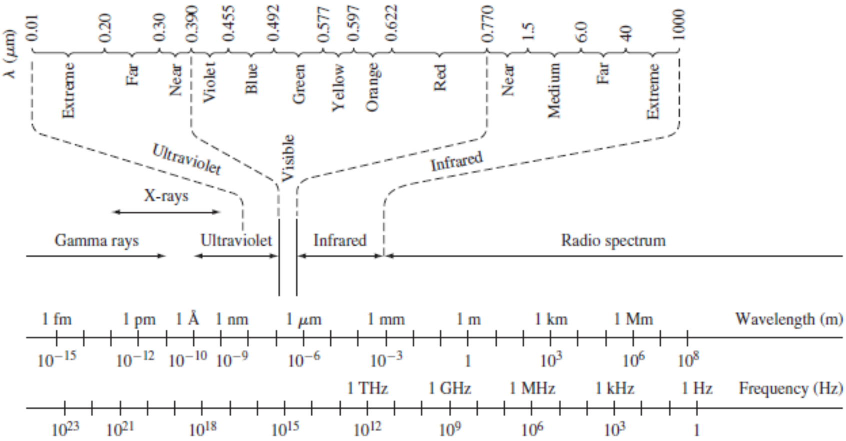

Figure 4: The electromagnetic frequency spectrum [46].

The solar radiation spectrum is described using the spectral irradiance ($I_{e\lambda}$), which is defined as:

$$I_{e\lambda} = \Phi_{ph}(\lambda) \cdot \frac{hc}{\lambda} \tag{2}$$

and the and the spectral photon flux ($\Phi_{ph}(\lambda)$) which is the photon flow per unit area ($s^{-1}m^{-2}$). The spectral irradiance determines the radiation level of sunlight, resulting in the AM1.5 spectrum at the Earth's surface which corresponds to an angle of 48.2°between Sun's position and the zenith. This spectral irradiance is depicted in Figure 5 has been established as the Standard Test Conditions (STC) which corresponds to the air mass 1.5 spectrum, a power density of 1000 W/m^2 and a standard temperature of 25°C.

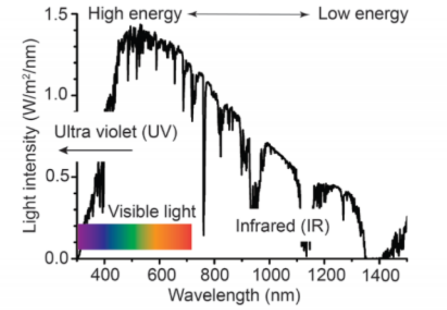

Figure 5: The AM1.5 solar spectrum [47].

2.1.2 Semiconductor materials

Semiconductors are defined as the group of materials with electrical conductivities between those of metals and insulators. They belong in group IV of the periodic table (elemental materials) or are comprised of a combination of materials from groups III-V or II-VI (compound materials). The most common elemental semiconductors are silicon (Si) and germanium (Ge) while compound semiconductors, such as GaAs, GaP or CdTe, can occur from various combinations of elements from those groups. Semiconductors are utilized for electronic devices manufacturing, such as photovoltaics, diodes, transistors and integrated circuits [46]. Based on the structure and bonding of its molecules, a solid can be distinguished into three major categories. These are amorphous, polycrystalline and single crystal solids. The amorphous materials are characterized by a random and low degree of ordered structure within the material, that means there is no consistent periodicity of atoms or molecules. On the contrary, a polycrystalline material is distinguished from multiple highly ordered and alternating phases, called single-crystal regions, characterized by different sizes and orientation of their crystal structure. Finally, single crystal solids have a specific, highly ordered structure and orientation, that extend throughout the material's spatial volume [46].

All semiconductors are characterized by a forbidden energy gap which separates their discrete electron energy levels. This energy gap is called the band gap (E_g) and under normal circumstances, energy levels can not exist in that region. The band gap of each semiconductor is located in between an occupied energy band, called the valence band (VB) and a vacant energy band, called the conduction band (CB) and is defined as the difference between the conduction band minimum (E_c) and the valence band maximum (E_v). When that conduction band minimum is located at the same wave vektor (k) as the valence band maximum, the semiconductor has a direct band gap. However, not all semiconductors have the same wave vector for their E_c (at k≠0) compared to E_v (at k=0), rendering those as indirect band gap materials [48]. In order for an electron to be excited from the occupied valence band to the conduction band at a direct band gap material, a photon with sufficient energy must be absorbed from the incident light. This is not the case however for the indirect band gap semiconductors, where the law of conservation of momentum must apply. The excitation of an electron to the conduction band minimum in this case, only occurs if a collision between a photon, an electron and a phonon takes place, in order for the phonon to provide the missing momentum to the photoexcited electron. Indirect transitions occur less frequently compared to direct transitions, affecting the absorption coefficient of the semiconductor [49]. The electron energy level at 0 K can be described by the electrochemical potential, called the Fermi level (E_f) and means that the probability of occupation of an energy state by an electron is 50% [44]. As shown in Figure 6, for an intrinsic semiconductor, the Fermi level is located in the middle of the band gap, while it shifts towards the E_c and E_v when the semiconductor is n-type or p-type doped, respectively.

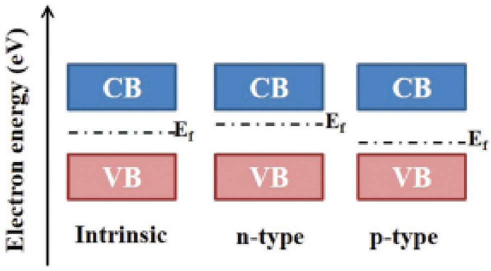

Figure 6: The energy band diagrams for intrinsic, n-type doped and p-type doped semiconductors [48].

The band structure can cause disparity in the electrical properties of each material. In case a solid has a band gap in the order of 4 eV or higher, it is described as an insulator. The main characteristics of insulators are the facts that the valence band is completely full of electrons and the conduction band completely empty, as well as the very large resistivity. On the other hand, metals are characterized by overlapping of the conduction with the valence band, resulting in very low resistivity.

When a semiconductor is illuminated, the light can be absorbed from the material and the energy of the photons is utilized to create an electron-hole pair. The electron can be consequently excited from the VB to the CB. The energy that is therefore needed for this excitation depends on the band gap energy of the semiconductor. The photon energy should be higher than the band gap in order for this to take place.

2.1.3 Electrochemical Systems

Electrochemical systems for energy storage are receiving increasing attention and among the numerous auspicious technologies, Redox Flow Batteries (RFB's) are considered a promising choice for future large-scale energy storage. The RFB is an electrochemical device in which liquid electrolytes, stored in separate tanks, are pumped around a circuit undergoing reversible electrochemical reactions. The redox couples are dissolved in a suitable supporting electrolyte. Subsequently, when there is a need for energy or excess energy to be stored, the redox electrolytes are pumped through an electrochemical flow cell, in order to be discharged or charged, respectively. The electrode size and electrolytes volume can be scaled independently, rendering it a versatile system for power and capacity management [18]. Apart from the volume, the electrolyte composition is a crucial parameter for the performance and stability of the system. The dissolved redox species should therefore satisfy several requirements in order to design the optimal configuration. An important factor is their solubility limit, since it is desired for the redox species to yield high energy and current density during cycling. The solubility limit can be controlled by selecting appropriate supporting electrolyte, pH and temperature working range and other additives. The energy density of the electrolyte is defined as:

$$E[\frac{Ah}{L}] = \frac{z \cdot C \cdot F}{3600} \tag{3}$$

Where n is the number of electrons involved in the reaction, C [mol/L] is the concentration of the redox species in the supporting electrolyte and F is the Faraday constant equal to 96.485 C/mol. Moreover, suitable redox potentials should be chosen, or controlled, to result in a high cell voltage. The fast and reversible kinetics as well as high ionic conductivity are also of great importance, in order to avoid hysteresis effects and output power related issues. Furthermore, the electrolyte should be thermally stable and have low light absorption to avoid parasitic absorption when coupled with a semiconductor. Generally, it is desirable for the optical absorption range of the electrolyte to not overlap with that of the semiconductor's. Finally, safe, earth abundant and low cost materials are always desirable [48].

Cyclic Voltammetry (CV) studies are performed to find the standard redox potential of the electrolyte redox species employed, at the specific conditions used. This is important to calculate from the Nernst equation, from which the expected maximum voltage of a redox species is needed to fully charge the cell [50].

$$E_{cell} = E^0_{cell} + \frac{RT}{zF} ln \frac{(Ox)}{(Red)} \tag{4}$$

Where E^0_{cell} is the standard cell potential, R is the gas constant, T the absolute temperature and (Ox) and (Red) correspond to the relative activities of the oxidized (Ox) and reduced (Red) species of the electrolyte. CV's scan through a voltage range in excess of the voltage of the Nernst equation and the response current which develops in the electrochemical cell is measured. By alternating the scan directions, the anodic and cathodic current peaks developed indicate the oxidation and reduction reaction of the redox species, respectively. This is illustrated in Figure 7. The midpoint of the potentials at which the current peaks occur, is the redox potential of the species [50].

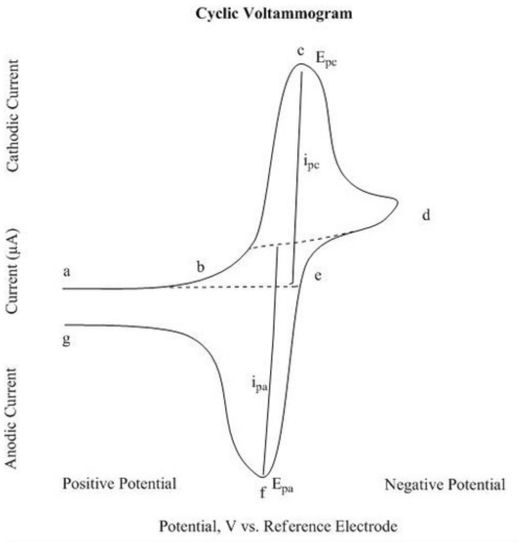

Figure 7: Sample voltammogram of a single electron oxidation-reduction reaction [51].

An important factor to consider when choosing the right redox species for the solar RFB operation, is the fact that based on the Nernst equation, the cell potential changes as a function of the concentration of the active species, as suggested by the Nernst equation. This can be described by [18]:

$$E_{cell} = E^0_{cell} + \frac{RT}{F} \cdot ln \frac{SOC^2}{(1 - SOC)^2} \tag{5}$$

As the redox species are charged, the SOC increases and this causes an increase in the Nernst potential, while the available overpotential for charging decreases. This results in a very low expected conversion efficiency at very high SOC. It is therefore desirable to take into account the Nernst potential and available overpotential, for proper selection of the redox couple based on their redox potentials, in order to be able to charge the battery until high SOC from the available photovoltage [52].

2.1.4 SRFB working principle

The working principle of the SRFB is based on the photovoltaic effect, which includes an induced potential difference through electromagnetic radiation at the junction of two materials [44]. When a semiconductor is submerged in the electrolyte and illuminated, charge carriers will be generated due to absorption of photons in the material. The energy from the photons, if higher than the band gap energy of the material, is utilized to excite an electron from the valence band to the conduction band. If the photon's energy is not sufficient to excite the electron past the forbidden energy states, it will not be absorbed and pass over the semiconductor. The electron excitation leaves a void in the valence band, which behaves as a positively charged elementary particle, called the hole. Once the charge carriers are generated, they are subsequently separated towards different contact layers. During this step, it is of outmost importance to consider the diffusion length and lifetime of the photogenerated carriers, in order to achieve efficient separation. Finally, the photogenerated charge carriers reduce or oxidize the dissolved redox species in the electrolyte. The charged species can then be stored in the same or a different cell, until there is a need for excess energy. A typical SRFB device is depicted in Figure 8. This includes at least one photoelectrode immersed in at least one electrolyte. There are many possible configurations for such a system, incorporating 2 or more electrodes and various modes of illumination. The PEC and RFB devices can be designed individually, connected with pumps for the flow of electrolyte between the charge and discharge cells, as shown in Figure 8, or it can be an integrated system with two or three electrodes. The advantage of incorporating more electrodes is that the discharging of the redox species can take place at the same time as their photocharging. Apart from the photoelectrode, the rest of the counter electrodes employed in the system should abide by several requirements. Firstly, they should have good electrochemical activity for both redox species to result in a low activation overpotential as well as be highly conducting to minimize the Ohmic losses. In addition, they should be porous enough and the electrolyte should have a high penetration depth in the counter electrodes to reduce energy consumption of the system. Finally, the materials should present good chemical stability, be cost-effective and environmentally benign [48].

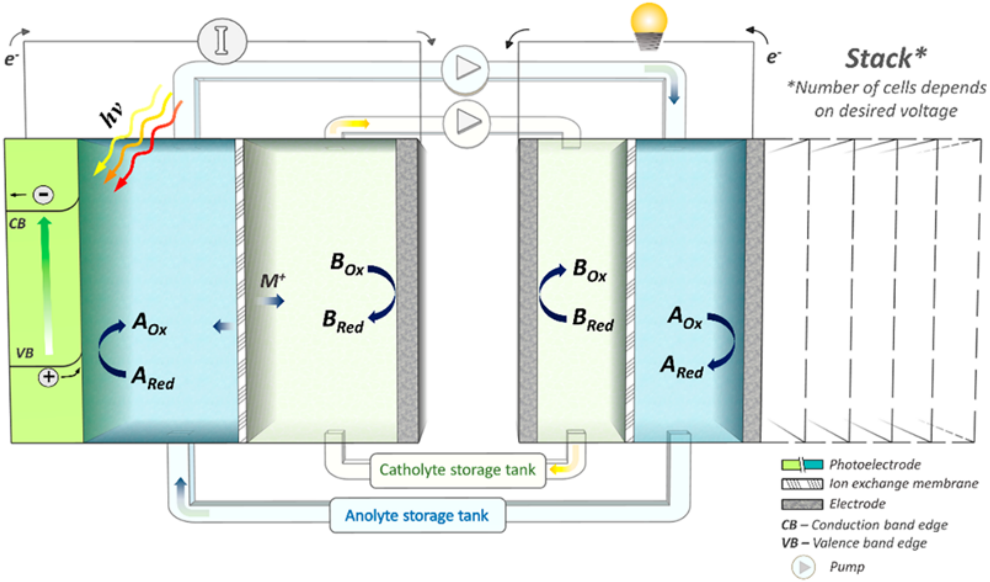

Figure 8: Schematic of a Solar RFB device [18].

Furthermore, there can exist configurations with more than one photoelectrode. If a dual band gap is incorporated for light absorption, a higher fraction of energy will be utilized. In order to efficiently make use of both photoelectrodes in such a configuration, there is a need for illumination of both semiconductors to obtain a similar current density. Nonetheless, semiconductors with complementary band gaps can be chosen, in order to absorb different photon energies and drive redox reactions with high potential difference [48]. Differences in configurations can also be noted regarding the mode of illumination. The immersed photoelectrode can either be illuminated from the front-side or back-side. These modes can be seen in Figure 9. Firstly, front-side illumination through the electrolyte, Figure

9a, most charge carriers will be generated near the semiconductor-electrolyte interface, making it easier for them to diffuse towards the electrolyte and back contact. However, there will be parasitic light absorption, which is not only dependent on the electrolyte, but also on the battery's SOC. On the other hand, back-side illumination, Figure 9b, has the advantage of no parasitic light absorption from the electrolyte, as well as avoiding light induced degradation issues. The photogenerated carriers will have to diffuse through the bulk of the material to reach the semiconductor-electrolyte interface [48].

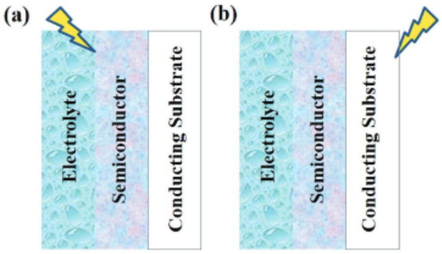

Figure 9: Schematic of a) front-side and b) back-side illumination [48].

2.1.5 Energy level matching

In order to design an effective SRFB device, the energy level matching between the different components is of utmost importance. Efficient charge carrier separation and consequently, solar charging of the dissolved redox species, relies on proper energy level alignment between the redox potential of the electrolyte with the band edges of the photoelectrode. In addition, appropriate matching of the energy levels should be considered in every layer interface of the solid surface. After the photoelectrode comes into contact with the electrolyte, in dark and equilibrium conditions, the Fermi level pinning and band bending will determine the charge carrier separation efficacy. Figure 10 depicts how the band positions of various semiconductors can be aligned with the redox potentials of some of the most crucial and widely studied redox species. There are several redox species with suitable redox potentials that can be charged by the generated photovoltage of each photoelectrode. Especially considering the addition of the organic redox species, further enhances the selection range, not only due to the diversity of available choices, but also due to the capability of controlling their redox potential by selecting the appropriate pH for the supporting electrolyte and side chain functionalization [18]. Here, the electron energy level is converted to the Standard Hydrogen Electrode (SHE) scale using [48]:

$$E_{vacuum} = -4.5eV - eE_{SHE} \tag{6}$$

The available photovoltage that will be generated and used to charge the redox species depends on the band gap of the material used. However, the full photovoltage range is not exploitable, since there are significant thermodynamic losses such as reaction overpotentials, difference in operating voltage and semiconductor band gap and several other factors such as Ohmic losses and parasitic absorption that affect the operation range [53]. Among system proof of concepts and other studies in the SRFB field related literature, it is a common phenomenon that the photocharging taking place is not sufficient to fully charge the redox species. On the contrary, in most cases the achieved SOC reaches very low values [25, 27, 30, 54–62].

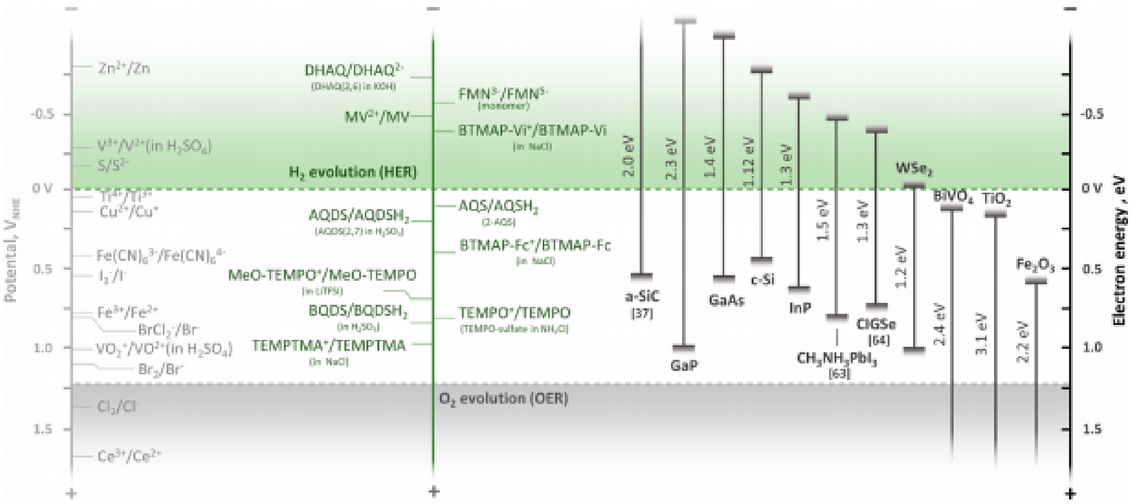

Figure 10: Band positions of various semiconductors (vs NHE, at pH=0) and redox potentials of crucial inorganic and organic redox species [18].

One of the reasons for this is that the available photovoltage for charging has not been considered with the thermodynamic losses and the redox potentials employed where not correctly designed. Furthermore, as already stated and shown in Equation 5, the cell potential increases with increasing SOC, meaning that if the electrolyte is charged until a point and then the necessary voltage is not supplied, the photocharging will decrease significantly. It is therefore pivotal, when designing an SRFB system, to consider band structure tuning, minimizing the voltage mismatch and to match the RFB cell voltage with the photoelectrode's maximum power point (MPP) [31].

2.1.6 Photoelectrode performance

When a photoelectrode is operated in solar cell mode, there are certain parameters that can be used to describe its properties under illuminated conditions. These parameters are the open circuit voltage (V_{oc}), the short circuit current density (J_{sc}), the maximum power output (P_{max}) and the fill factor (FF). In order to determine those parameters, the solar cell is illuminated with a certain intensity (P_{in}) and the corresponding J-V curve is measured. A typical solar cell J-V curve is presented in Figure 11. In addition, the external solar cell parameters are shown. The short circuit current corresponds to the current flowing at the external circuit when the solar cell electrodes are short circuited. The short circuit current depends on the incident illumination on the solar cell and therefore to the photon flux. The measurements under the Standard Test Conditions (STC) imitate the AM1.5 solar spectrum, with a measured total irradiance on the cell surface of I_{in}=1000 W/m^2 and a constant temperature of 25 °C. The open circuit voltage depends primarily on the semiconductor properties and is the voltage at which no current flows through the cell. The externally applied forward bias voltage at which the generated photocurrent becomes equal to the reverse current and consequently cancel each other out, is the open circuit voltage. The FF is defined as the ratio of the maximum obtainable power to the product of V_{oc} and J_{sc} and is an important parameter for the power conversion efficiency calculation. The FF is affected by many parameters, both internal materials' related and external parameters of the solar cell [44].

$$FF = \frac{P_{max}}{V_{oc}J_{sc}} \tag{7}$$

$$n = \frac{V_{oc} J_{sc} FF}{I_{in}} \tag{8}$$

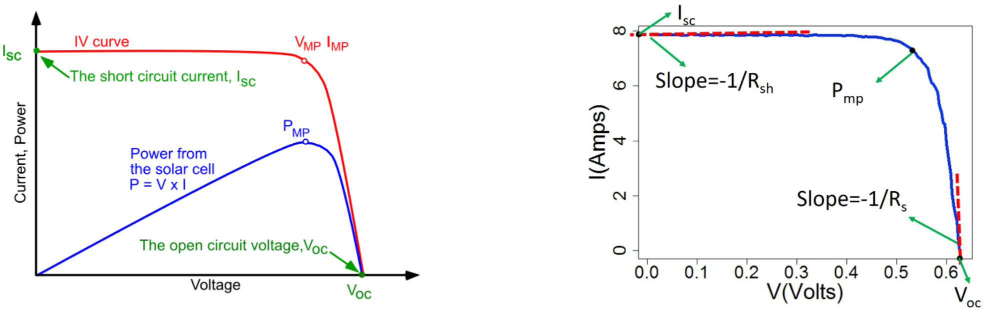

Figure 11: a) A typical solar cell J-V curve with it most important parameters [63] and b) graphical representation of the series and shunt resistance derived from a solar cell J-V curve negative inverse slope near the V_{OC} and J_{sc}, respectively [64].

Figure 11b indicates the series and shunt resistance of the solar cell, derived from the measured illuminated I-V curve. The series resistance corresponds to the negative inverse of the curve's slope near the open circuit potential, while the shunt resistance is the negative inverse of the curve's slope near the short circuit current. The series and shunt resistances can affect the operation of the solar cell to great extend. An increased series resistance results in lower current output, while a reduced shunt resistance results in lower open circuit voltage, since there exists a path of least resistance for the current to flow to bypass the actual configuration [44]. The effect of the resistances on the solar cell J-V curve are shown in Figure 12. The solar cell dark diode current can be described by the Boltzmann approximation. This depends on I_0, the reverse saturation current. The I_0 is an important parameter for any solar cell operation. When a diode is reversed biased and the space charge region width is increased and as a response, majority carriers move away from the junction. This results in no current flow produced by majority carriers. During the illumination however, charge carriers keep on generating constantly. Those that are generated near the junction will manage to flow through it, depending on their charge, so a current flow develops.This is due to the flow of minority charge carriers and is called reverse saturation current. In practice, solar cells are described by the same equation, approximating their non-ideality with an ideality factor, n, in the Boltzmann exponent factor [65].

$$I = I_0 (exp^{\frac{qV}{nkT}} - 1) \tag{9}$$

$$J_0 = q n_i^2 (\frac{D_N}{L_N N_A} + \frac{D_P}{L_P N_D}) \tag{10}$$

$$L_i = \sqrt{D_i \tau_i} \tag{11}$$

Where D_i is the diffusion coefficient for each region $[m^2 s^{-1}]$, L_i is the diffusion length of the minority charge carriers [m], N_i is the particle density $[m^{-3}]$ and τ_i is the minority charge carrier lifetime [s]. In general, the charge carrier lifetime is greatly decreased when many recombination processes are taking place and therefore the diffusion length of minority carriers is also significantly shorter. The saturation current density, also denoted as dark current density, can affect the available photovoltage and therefore the energy efficiency.

Where D is the diffusion coefficient [$m^2 s^{-1}$] and l is the diffusion length [m] . The subscript n or p corresponds to the properties of the minority carrier in each respectively doped region. N_D and N_A are the net donor impurity concentration on the n-side and acceptor concentration on the p-side of the junction [m^{-3}].

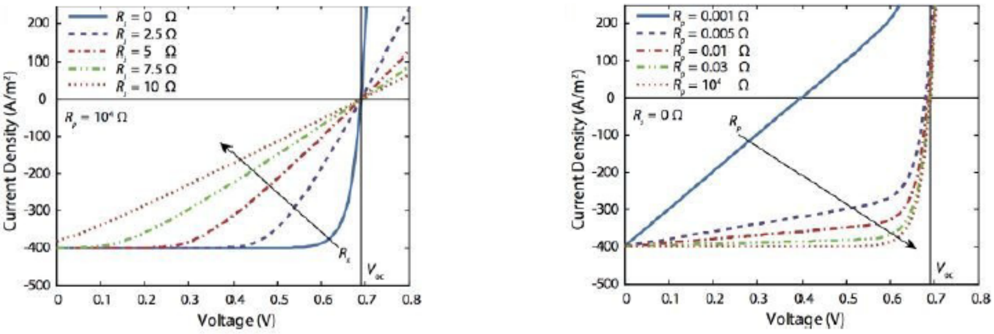

Figure 12: The effect of a) series resistance and b) shunt resistance on the solar cell J-V curve [44].

2.2 Charge transfer mechanisms

The physics underlying the layer interfaces, are a fundamental issue in the effective operation of every solar cell or photoelectrode. These include the junctions between different semiconductors (heterojunctions), the junctions between a semiconductor and a metal (MS junctions) and the interface between the photoelectrode and the electrolyte. In depth understanding of how the electronic structure of each material is affected and what the influence is on the operation of the device, will result in the optimal energy level design and efficiency of the device.

2.2.1 Semiconductor/Semiconductor interface

A heterojunction is a junction formed between two different semiconductors, either n or p-type doped, which rises to four different combinations. These are n-P, p-N, n-N and p-P, where the material with the lower band gap is referred to with a lower case letter while the material with the higher band gap is referred to with an uppercase letter. When two semiconductors come in contact under dark and equilibrium conditions, their Fermi level will be aligned and constant throughout the junction. However their conduction and valence bands will not be continuous, due to their band offsets. The electron affinity rule describes this as [44]:

$$\Delta E_c = q(\chi_{e1} - \chi_{e2}) \tag{12}$$

Where χ_{ei} is the electron affinity of semiconductor i. This can also be expressed with respect to band offsets as:

$$\Delta E_c + \Delta E_v = E_{g1} - E_{g2} = \Delta E_g \tag{13}$$

In addition, the vacuum energy, which acts as reference, is constant across the junction under equilibrium. However, a gradient of electrostatic potential is developed across the junction. This is denoted as built-in voltage and is expressed as [44]:

$$V_{bi} = \phi_{s1} - \phi_{s2} \tag{14}$$

Where ϕ_{si} is the work function of semiconductor i. The electric field is maximum at the junction and deteriorates across the depletion region, following the equation:

$$\xi_i(x) = \frac{qN_{d/ai}}{\epsilon_0\epsilon_i} \cdot (l_i - x), -l_n \leq x \leq l_p \tag{15}$$

Where $N_{d/a}$ is the donor or acceptor concentration, ϵ_0 the vacuum permittivity and ϵ_i the relative permittivity of the material. The depletion region, for the case of a n-P junction on each respective side, is expressed as [44]:

$$l_n = \sqrt{\frac{2\epsilon_0\epsilon_n\epsilon_P N_{aP} V_{bi}}{qN_{dn}(\epsilon_n N_{dn} + \epsilon_p N_{ap})}} \tag{16}$$

$$l_P = \sqrt{\frac{2\epsilon_0\epsilon_n\epsilon_P N_{dn} V_{bi}}{qN_{aP}(\epsilon_n N_{dn} + \epsilon_p N_{ap})}} \tag{17}$$

The total depletion width is:

$$W = l_n + l_P = \sqrt{\frac{2\epsilon_0\epsilon_n\epsilon_P (N_{dn} + N_{aP})^2 V_{bi}}{qN_{dn}N_{aP}(\epsilon_n N_{dn} + \epsilon_p N_{ap})}} \tag{18}$$

In general, when a pn^+ or a np^+ junction is used, the depletion width in the high doping region is practically zero, as will be shown in the Results section. The energy band diagrams of a n-P heterojunction example is shown in Figure 13.

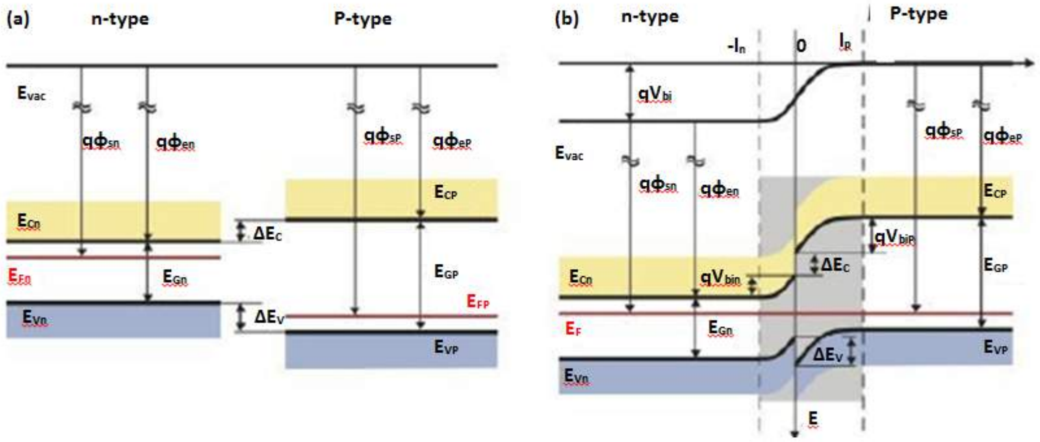

Figure 13: The band diagrams of a n-type and a P-type semiconductor a) before and b) after contact [44].

2.2.2 Semiconductor/Metal interface

Corrosion is a very important factor for the operation of any photoelectrochemical cell and poses a challenge for the long-term stability of the device. Many techniques have been developed to delay or prevent corrosion processes, the most popular of which is applying a chemically stable coating on the surface of the device. The processes leading to corrosion of a semiconductor are more complicated compared to that of a metal, due to constantly varying number of charge carriers as well as impurities or dopants incorporated in the bulk. Three different types can be distinguished, photoelectrochemical, electrochemical and chemical. Photoelectrochemical corrosion involves net charge transfer at the semiconductor-electrolyte junction of photoexcited minority charge carriers. Electrochemical corrosion is due to net charge transfer at the same junction, but caused by transfer of majority carriers. Finally, chemical corrosion does not require charge transfer, but chemical reactions can take place that will degrade or negatively affect the electrode at the interface. In order to prevent any of these cases of corrosion of the photoelectrode, a protective layer is applied, that prevents the contact between the semiconductor and the electrolyte and can also act as a co-catalyst for the oxidation or reduction of the redox species. The theoretical requirements for such a thin film would be to have the optimal electronic and optical properties, such as high transparency, low trap state density, suitable work function. The photoelectrosynthetic behaviour of this protective thin film will depend upon its composition, the way it was processed and the interface structure between the materials [66].

When a metal and a semiconductor come in contact in equilibrium, their vacuum and Fermi level will be continuous. However each metal in only characterized by one parameter, the work function (ϕ_m). Therefore, an energy barrier (ϕ_B) will form between the metal and the semiconductor, equal to the difference of the metal work function and the semiconductor electron affinity [44]:

$$\phi_B = \phi_m - \chi_e \tag{19}$$

In addition, a built-in voltage will also develop in this junction:

$$V_{bi} = \phi_B - (\phi_s - \chi_e) \tag{20}$$

This barrier can either be a Schottky barrier or an Ohmic contact. Shortly, the rectifying junctions or Schottky barriers have a large barrier ($\phi_B \leq k_B T$)and current transport mainly takes place due to transport of majority charge carriers through thermionic emission. Otherwise, the Ohmic contact results in a reduces resistance at the junction and a low voltage drop. Figure 14 depicts a representation of the energy levels allignment before and after contact of a metal with a semiconductor.

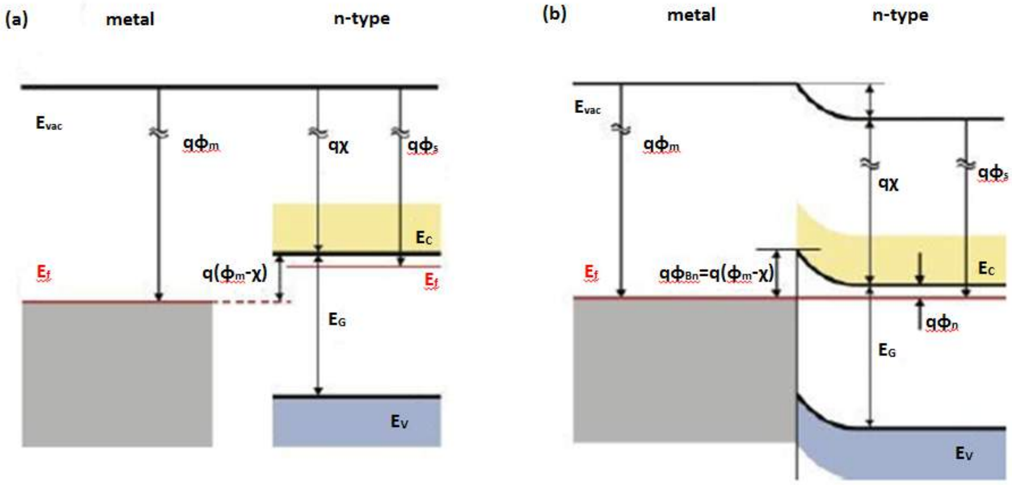

Figure 14: The band diagrams of a metal and a semiconductor a) before and b) after contact [44].

2.2.3 Solid/Liquid interface

Stability between the semiconductor and electrolyte is a crucial issue for the operation of any photoelectrochemical cell. In order to overcome the limitations occurring from an exposed semiconductor surface to the electrolyte, whether it is photocorrosion, interfering surface states, impurity effects or ion exchange caused by light, a thin, unreactive and conducting metal layer is deposited on the surface of the electrode, that requires the formation of a Schottky barrier between the metal film and the semiconductor. In that case, when the layer is deposited, the metal's ionization energy is aligned under equilibrium with the semiconductor's Fermi level. Subsequently, when the metal layer comes in contact with the electrolyte, a flat band potential is developed at the interface. This takes place due to the equalization of the charge of each side [48, 67]. The flat band gives the amount of band-bending caused by the Fermi level pinning at the Schottky interface. In order to have optimum charge carrier transfer at the interface, this band bending should be designed to be close to the redox reaction potential of the electrolyte.

As soon as a semiconductor is immersed in the electrolyte, the flat band potential is developed. Afterwards, a space charge (SC) region is developed on the photoelectrode side. This is the outcome of the accumulation of the electrons on the solid surface or migration towards the electrolyte and takes place in a considerable distance from the interface, since semiconductors have much lower carrier density compared to metals [49]. The potential at the SC region is given by the Poisson equation:

$$\frac{d^2\Delta\phi_{SC}}{dx2} = -\frac{1}{\epsilon\epsilon_0}\cdot\rho(x) \tag{21}$$

Where $\rho(x)$ is the charge density and described by:

$$\rho(x) = q[N_d - N_a - n(x) + p(x)] \tag{22}$$

And the electron (n(x)) and hole (p(x)) densities:

$$n(x) = N_c \exp -\frac{E_c(x) - E_f}{kT} \tag{23}$$

$$p(x) = N_v \exp \frac{E_v(x) - E_f}{kT} \tag{24}$$

In the case of a photoelectrode with a pn^+ or np^+ junction, the calculations for the depletion region and intrinsic semiconductor properties can be simplified (analysis on Discussion chapter).

2.3 Recombination Mechanisms

The second law of thermodynamics states that all systems are spontaneously driven towards thermodynamic equilibrium and maximizing their entropy. Based on that, a meta-stable photoexcited electron located in the semiconductor's conduction band, will end up at a lower energy state in the valence band. When this happens, the electron will recombine with the generated hole. There are various recombination effects and these are more likely to happen in direct band gap materials, since no addition of momentum is required, as previously explained. Recombination of photogenerated charge carrier, before their separation towards their respective contact layers, can greatly affect the performance of the photoelectrode. When the charge carriers recombine, the generated current is decreased, since less charge will flow through the circuit. In addition, the recombination rate affects the saturation current density. The recombination mechanisms can be distinguished between bulk (direct, SRH and Auger recombination) and surface processes.

2.3.1 Direct (Band-to-Band) recombination

Direct recombination, the opposite process of radiative generation of charge carriers, dominates in direct bad gap materials. The process involves the recombination of a "free" electron from the conduction band with a hole from the valence band. This is followed by the generation and release of a photon, with energy similar to the material's band gap energy, as shown in Figure 15a [44]. Under thermal equilibrium, the direct recombination rate is equal to the direct generation rate and both are proportional to the concentration of free electron available at the conduction band as well as the concentration of holes in the valence band. Under illuminated conditions, excess charge carriers are being generated, until the system reaches a steady state, were the direct generation is again equal to the direct recombination.

2.3.2 Auger recombination

Conversely to band-to-band recombination, Auger recombination involves a three-particle process and is more important for indirect band gap materials. The process includes the conservation of energy and momentum of the recombining electron-hole pair, by transferring energy and momentum to a third particle involved in the process. This third particle can be either an electron or a hole. The two different cases are depicted in Figure 15b.

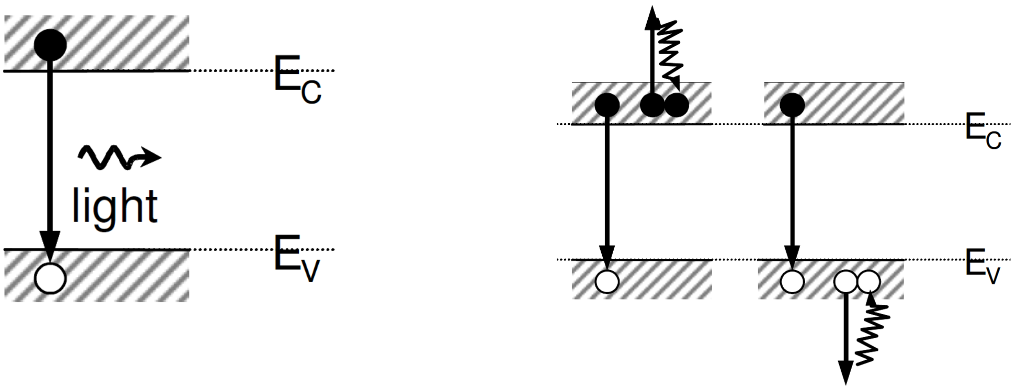

Figure 15: a) Direct recombination process and b) Auger recombination process with a) two electrons and one hole (eeh) and b) two holes and one electron (ehh) [68].

The third particle involved is excited to higher energy levels of the conduction band or deeper energy levels of the valence band, depending on if it is an electron or a hole, respectively. The excited charge carrier is consequently relaxed to its initial state, extracting heat through vibrational energy or phonon modes [44]. Whether the third particle is an electron or a hole, depends on which are the majority carriers in each specific application.

2.3.3 Shockley–Read–Hall recombination

Shockley–Read–Hall (SRH) recombination does not include band to band transitions, since it involves two steps and it only takes place in materials with defects. The recombination happens in trap states, which can be impurity atoms, interstitials, or lattice defects. These trap states introduce an allowed energy state in the band gap of the semiconductor, where a charge carrier can be trapped and attract the opposite to recombine. It is considered the dominant mechanism in most semiconductors and the excess energy from the recombination is dissipated as heat. SRH recombination is effective when the defect state energy level is not located near the conduction or valence band edge. If an electron is trapped in a defect state near a band edge, it can be re-emitted towards the conduction band. Nevertheless, SRH recombination is dependent on several parameters, the most important of which are the free carrier concentration and the trap density [44]. The process is shown in Figure 16a. The recombination rate of SRH process consists of four individual processes associated with electron or donor traps and their respective rates. These processes involve the electron capture, electron emission, hole capture and hole emission.

2.3.4 Surface recombination

Surface recombination takes place in all semiconductors. It is caused by the dangling bonds at the surface, which are practically defects, since surface atoms have electrons which do not create covalent bonds with neighboring electrons (Figure 16b). These dangling bonds form mid-gap states inside the band gap, allowing for recombination sites to be formed. Consequently, formed trap states inside the band gap is a common characteristic of semiconductors, that can also cause SRH recombination to take place, making it the dominant mechanism.

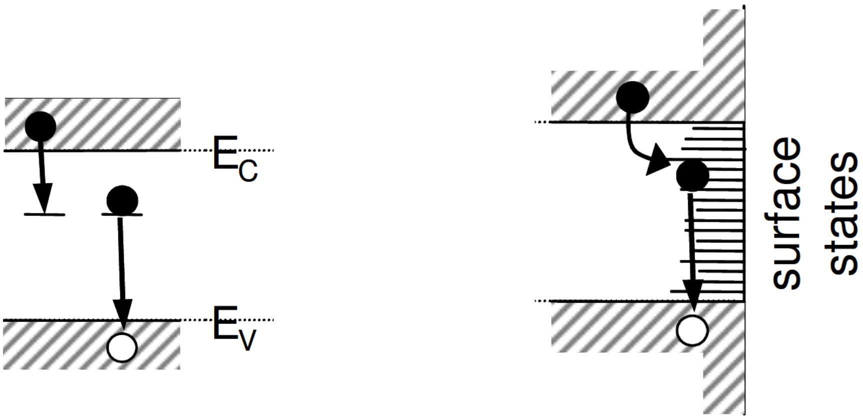

Figure 16: a) Shockley–Read–Hall recombination process and b) surface recombination mechanism through formation of dangling bonds at the surface. [68].

3. Experimental methods and materials

The objective of this chapter is to introduce the experimental methods employed for the photoelectrodes fabrication and characterization. The cell components are described and the SRFB testing procedures are reported to gain insight on the properties and the most important aspects for the efficient operation of the system.

3.1 Electrode fabrication and characterization

This section addresses the thin film solar cells fabrication procedure and the subsequent measurements for their characterization in order to be used as photoelectrodes in the integrated photoelectrochemical system.

3.1.1 Materials and chemicals

The photoelectrodes were produced by commercial semiconductor wafers at DTU by D. Bae and used without further optimization. For the photoanode, a shallow pn^+-junction was produced in p-type (100) Si wafers (Topsil, 1 to 20 Ωcm, boron-doped, acceptor density of $5 \cdot 10^{19} cm^{-3}$) by n^+ doping by a boron diffusion furnace process. Depending on whether the wafer is polished from one or both sides, etching of the unpolished side takes place in order to deposit the appropriate thin films, either for charge carrier transport or for creating an Ohmic contact for the electrical connection. Surface etching of unpolished Si samples is necessary for the operation of the device. The KOH etchant employed corrodes microstructural features on Si, necessary for flattening the semiconductor surface, removal of contaminated surfaces and removal of formed oxides at the same time. In order for the Si unpolished surface to be etched, a 40% KOH solution was created, since it has been found that solutions with less than 30% KOH do not perform satisfyingly [69]. The solution included a small amount of isopropyl alcohol, in order for the etching rate to dwindle. The 40% KOH solution is heated to 80 °C. Some drops of H_2O_2 are put on the unpolished Si surface and left for two minutes. The sample is then rinsed with deionized water and etched in contact with the solution at high temperature for 40 minutes. This results in 50 μm/hour etching rate. After the etching is finished, the sample is sonicated in deionized water, dried with N_2 gas and stored.

The reference electrode, $Hg/HgSO_4$ saturated with K_2SO_4 solution, is prepared by bringing deionized water close to boil and then making it saturated with K_2SO_4. It has a redox potential of 0.643 V_{NHE} at 25 °C.

The membrane was a Nafon-117 (Fuelcellstore). The pretreatment procedure included submerging the IEM in 3% H_2O_2 at 80 °C for 20 minutes. Afterwards, the membrane is stored in H_2O until it is used.

The electrolytes employed for the measurements, $K_3Fe(CN)_6$ (Sigma-Aldrich, $\geq$ 99%), $K_4Fe(CN)_6 \cdot 3H_2O$ (Sigma-Aldrich, $\geq$ 99.5%) NaI (Sigma-Aldrich, $\geq$ 99.5%), NH_4Br (Sigma-Aldrich, $\geq$ 99.99% trace metals basis) and $SnCl_4 \cdot 5H_2O$ (Sigma-Aldrich, $\geq$ 98%) were used as received. The synthesis of TEMPO-sulfate was based on a related report and used as received [70].

3.1.2 Thin-film deposition process

Direct Current Sputtering is a Physical Vapor Deposition (PVD) technique, which refers to non-chemical thin film fabrication procedures. While sputtering presents several limitations in the formed thin film compared to other methods, it is the process of choice for several industrial applications due to its wide application range. During the process, a coating material is chosen as the target (cathode) to be deposited in a vacuum chamber and is bombarded by Argon ionized gas molecules which are generated in a glow discharge in front of it. Molecules of the target are caused to be removed (sputtered-off) into the generated plasma and are subsequently condensed on the substrate (anode). The basic sputtering procedure presents several practical limitations, such as low ionization efficiency and deposition rates, as well as heating of the substrate. These problems have been resolved by magnetron sputtering, which unlike basic sputtering, develops a magnetic field configuration that controls the movement of the emitted secondary electrons, responsible for conserving the generated plasma, near the surrounding area of the target material. This results in increased chances a sputtered-off atom collides with an ionized electron and therefore higher ionization efficiency, ion bombardment and deposition rate [71]. A schematic of the procedure described is presented in Figure 17.

DC Sputtering is one of the most simple PVD techniques used for coatings of conducting materials, non-reflective coatings, optical components etc., and is limited to dielectrics. Its main advantages include the ease of controlling the process and the relatively low cost. Depending on the conditions employed for the deposition of the thin film, the result can vary significantly in their electronic structure, optical properties, crystalline structure and composition. The parameters that can be optimized for the desired result include the sputtering power, total pressure, temperature, gas composition (individual partial pressures) and time. In the present study, AJA International ATC 2400 sputtering system was used to optimize and vary these deposition parameters.

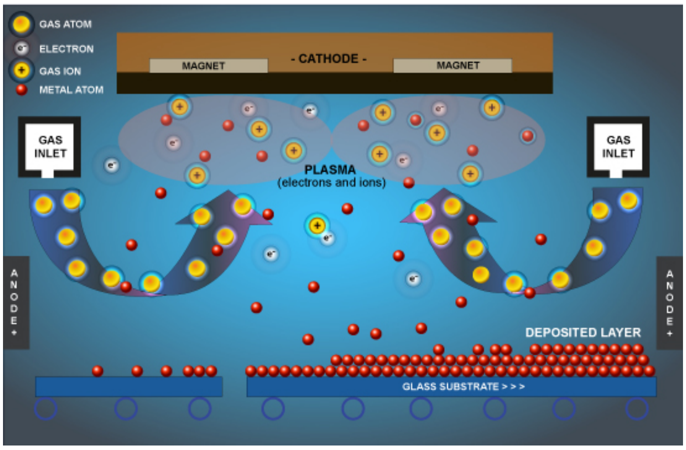

Figure 17: Schematic diagram of DC magnetron sputtering [72].

3.1.3 Post-annealing process

Annealing is a heat treatment technique in thin films fabrication, that alters the physical and chemical characteristics of the material. Depending on the conditions employed, thermal annealing can affect the material's micro-structure, like defect states concentration, intrinsic stress, grain size and surface roughness or the phases of the material, like preferred orientation and crystallinity. Temperature, time and ambient environment determine the changes that take place. In general, annealing can be used to improve the conductivity and electronic properties of the film as well as its surface morphology [73]. The post-deposition annealing process (ATS Applied test systems inc.) took place at 200 °C for all thin films.

3.1.4 Ultraviolet–visible spectroscopy

Ultraviolet and visible absorption spectroscopy (UV-Vis) is primarily used to measure the absorbance (A), transmittance (T) and reflectance (R) of a film, for a specific wavelength or an extended spectral range, described below. As explained in Equation 1, each photon with a specific wavelength has a certain quantized energy level. Visible and ultraviolet radiation (Figure 4) incident on the target material cause the excitation of electrons to higher energetic states. The excitation takes place if the energy provided by the photon is sufficient and thereby absorbed by the film. The larger the energy gap between the full orbital and its subsequent empty anti-bonding orbital, the higher photon energy will need to be provided to excite an electron [74]. A schematic of the UV-Vis procedure is shown in Figure 18.

$$A + T + R = 1 \tag{25}$$

A light source provides the radiation, which passes through a prism. Then the incoming light splits into its components and is focused on the target material. Behind the target, detectors convert the transmitted light into current, which signals the response of the target. In order to eliminate error odds, a so-called "blank" sample is first measured, whether that is a cuvette only containing the supporting electrolyte of the redox species or the substrate on which a thin film is deposited. Once the signal is detected, light absorbance can be quantified by comparing the initial light intensity (I_0) over the final detected one (I):

$$A(\%(\lambda)) = log\frac{I_0(\lambda)}{I(\lambda)} = -log(T\%(\lambda)) \tag{26}$$

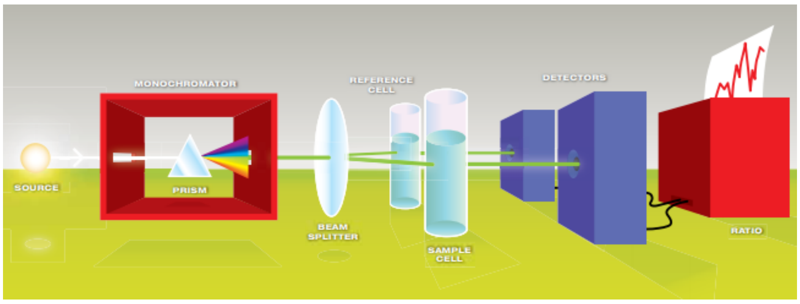

Figure 18: Schematic diagram of UV-Vis spectrometer [74].

The system used was a Perkin-Elmer Lambda 900 UV-VIS-NIR Spectrometer. Based on the wavelength of the incident light that will be absorbed by the thin film, its band gap can be determined. There are four cases that can be distinguished regarding the electronic structure of each thin film. Their band gap can include an allowed direct, allowed indirect,forbidden direct or forbidden indirect transition. As previously mentioned, the allowed direct and indirect transitions refer to the need for just photon energy or photon energy along with phonon momentum for the electron to be excited, respectively. The forbidden direct and indirect transitions refer to cases of zero momentum matrix element, which does not allow an excitation regardless of the supplied energy [75]. The optical absorption coefficient (α) and band gap energy of the material are given by:

$$\alpha = \frac{2.303A(\%)}{d} \tag{27}$$

$$\alpha = C\frac{(hv - E_g)^{1/n}}{hv} \tag{28}$$

Where C is a constant independent of wavelength, d is the sample thickness and n is determined by the transition type and is equal to 0.5, 2, 1.5 and 3 for allowed direct, allowed indirect, forbidden direct and forbidden indirect transitions, respectively. Once the Tauc coordinates ($\alpha hv - hv$) are plotted, the intersection of the linearized part of the curve with the x-axis determines the band gap energy of the material.

3.1.5 X-ray diffraction

X-ray diffraction (XRD) is one of the most widely used techniques to inquire into the structural properties and degree of crystallinity of materials and can be utilized to investigate powders or films, since the X-ray penetration depth, and therefore the investigation depth of the material's internal structure, can be controlled. The XRD analysis is illustrated in diffraction peaks, which originate from the periodical pattern of the material's atomic structure and represent its lattice parameters. The lattice parameters are unique to every crystal and relevant data is widely available on literature to precisely determine any structure [76].

Bruker AXS X-ray Diffraction Elemental Analysis was used for the XRD measurements. These XRD patterns are a result of the elastically scattered X-rays after collision with the atoms of the crystal lattice. Interpretation of these diffraction peaks is based on Bragg's law, which describes the principle of constructive interference as:

$$2d\sin\theta = m\lambda \tag{29}$$

Where d is the distance between the Bragg's planes and can be the magnitude of any of the lattice parameters, θ is Bragg's angle, m is the diffraction order, and λ is the wavelength of the incident X-rays. The XRD measurement procedure and the variables described are shown in Figure 19.

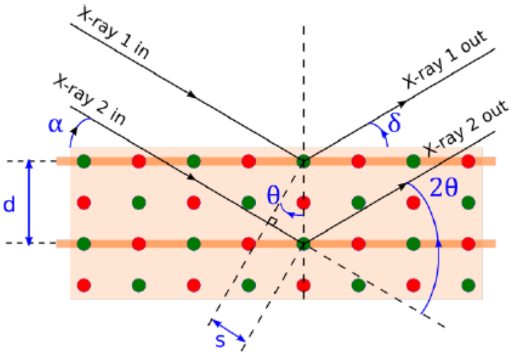

Figure 19: Schematic representation of XRD measurement procedure. Green and red circles are centers that the x-rays are diffracted. The X-ray incident and exit angle are denoted as α and δ, respectively. The Braggs planes (orange lines) are at a distance d and θ is Bragg's angle [76].

3.1.6 X-ray photoelectron spectroscopy

X-ray photoelectron spectroscopy (XPS) is a surface analysis technique based on the photoelectric effect. During XPS, a sample is irradiated with monoenergetic x-rays, which interact with surface atoms at a maximum penetration depth of 10 μm , causing their electrons to be emitted from the material and their energy is measured [77]. The emitted electrons are translated in the measurement as counts per second (CPS) as a function of binding energy (eV). Binding energy is the difference between the energies of the initial and the final states of the emitted electron. By definition, the Fermi level corresponds to zero binding energy. However, there are multiple states that an electron can be emitted to as well as a variety of probabilities, depending on the incident photon energy which affects the sample volume from which electron are emitted, as well as the variable energy that the electrons possess and is affected by their position and the photon energy [78]. While the binding energy is important to analyze the surface structure of the material investigated, the kinetic energy of the final state of the emitted electrons can provide important information about the sample. This is given by:

$$KE = hv - BE - \phi_s \tag{30}$$

Where BE is the binding energy (eV) and ϕ_s is the work function.

A Thermo Scientific K-Alpha X-ray Photoelectron Spectrometer (XPS) System was used for all measurements. XPS is a widely used analysis technique and is employed for surface elemental analysis or the determination of their concentration. Each element can be matched with a unique set of binding energies and there is extensive literature regarding material compositions. When the binding energy is measured, the resulting shift and intensity will determine the elemental and chemical state of the material [77]. In addition, the full width at half maximum (FWHM) can be measured, which provides information regarding the chemical bonds that contribute the an observed peak, changes that might occur in the material due to the incident photons or localized differences in the charged state of the surface.

Apart from the electrons emitted from surface states due to the photoelectric effect, Auger electrons can also be emitted and measured. The necessary energy for this excitation can be provided by the relaxation of photoexcited ions of the surface, after the primary electrons are emitted. After an electron transmits at a higher energy state in a vacant inner orbital of the atom, another electron can be excited or emitted of the material by capitalizing on the excess energy provided. The kinetic energy of this excited Auger electron will match the energy difference between its final state and the initial energy of the relaxed electron [78] and is given by:

$$KE_{Auger} = BE_{final} - BE_{initial} - \phi_s \tag{31}$$

3.1.7 Resistivity measurement

The electrical resistivity of the thin films studied is a crucial property to understand and improve them. Depending on the method employed, the axial or in-plane conductivity can be roughly measured. Electrical resistivity is inversely associated with other semiconductor properties, such as carrier concentration and mobility, through the equation [79]:

$$\rho = (Ne\mu)^{-1} \tag{32}$$

Where N is the total dopant concentration (atoms/cm^3), e is the electronic charge (C) and μ is the majority carrier mobility ($cm^2/(Vsec)$). Determining the thin film's resistivity can therefore provide useful information, not only about the charge carrier diffusion paths and mechanisms, but also about the intrinsic properties of the semiconductor. Charge carrier diffusion can take place both directly or with a combination of steps. One of the methods to determine the thin film resistivity is the two-point probe measurement. This method allows for the axial resistivity measurement, accordingly to the charge carriers diffusion path, while it is also suitable for highly resistive samples. The major disadvantage is the fact that the contact resistance between the probe and the metal cannot be eliminated and its resistance contributes to the measured total sample resistance. Nevertheless, a suitable configuration should be employed in order to result in an Ohmic contact between the metal and semiconductor in contact. During the measurement, the voltage drop and the current are measured across the sample, resulting in the following equation to derive the resistivity [80]:

$$\rho = \frac{VA}{IL} \tag{33}$$

Where V is the voltage drop across the sample (Volts), I is the current flowing (A), A is the cross sectional area of the sample (cm^2) and L refers to the thickness of the thin film (cm).

3.1.8 Atomic force microscopy

Atomic force microscopy is similar to a scanning probe microscope in the sense that a topographical image of the sample's surface can be illustrated. The images can be obtained with atomic resolutions of 10^{-10} m. The operating principle is based on the interactions between a tip and a sample surface. As soon as the tip, which is integrated to the end of a spring cantilever, is brought close to the sample surface, interatomic potentials are developed between the atoms of the surface and those of the tip. This results in a movement of the cantilever due to the potentials applied, with which is possible to map the sample surface based on the deflection measured [81]. The AFM imaging was performed, on the different samples presented in this work, using a Bruker Dimension Icon atomic force microscope. A Bruker SCANASYST-AIR probe with a constant force of 0.4 N/m was used in the PeakForce Tapping mode to obtain these images.

3.2 Cell components and testing procedures

This section describes the procedure followed for the fabrication of the photoelectrodes to be used in the SRFB, as well as the photoelectrochemical cell configuration. In addition, the dark and illuminated measurements are described to fully characterize the photoelectrode to be used for successful charging of the electrolytes employed.

3.2.1 Device preparation process

The photoelectrodes fabrication process is critical and needs to be strictly implemented to achieve the desired results. Following the deposition of the desired thin films on the photoelectrode, a diamond tip scriber is used to cut the semiconductor wafer into approximately 1cm × 1 cm pieces. To avoid any contamination from the package material, all sample are cleaned using an ultrasonic bath with deionized water and ethanol for 20 minutes each, then dried with N_2 gas. The structure of the photoelectrode allows for different operating modes in the SRFB. The possible configurations include operating as a photoanode or a photocathode, adjusting the redox couple employed in terms of reduction–oxidation reaction, as well as illuminating from the front side through the electrolyte, or the back side of the semiconductor. Regarding the illumination mode, an important aspect is where the p-n junction is located in the photoelectrode configuration, taking into account the lifetime and diffusion length of photogenerated charge carriers. This can lead to better charge carrier separation, avoiding recombination that can lead to lower current output and therefore lower efficiency. The thickness of the deposited thin films are strictly monitored and controlled using the quartz crystal microbalance (QCM) embedded in the DC magnetron sputtering system. Afterwards, their thickness is verified by a interferometric surface profiler (Dektak 3) in order to determine the band gap. Profiling is used to measure height variations of a sample and optical path length of a wave of light is compared between that and a reference surface. The two light beams originating from the same source, interfere and the sensor focuses on the area of greatest contrast. The thickness of the measured sample can then be determined when compared to the reference surface.

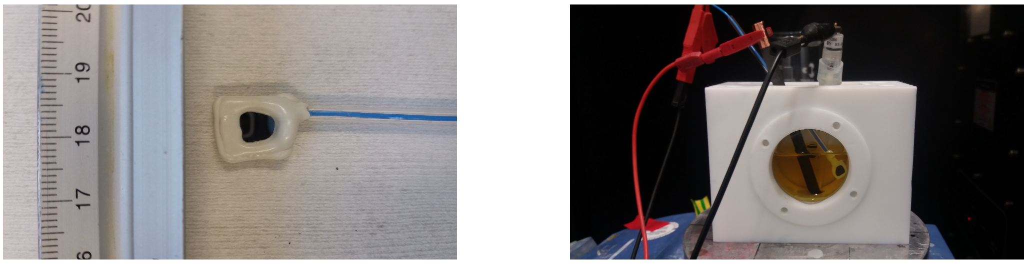

Figure 20: a) The fabricated photoelectrode after thin film deposition, connections and covered with epoxy in order to be used for the CV and MS analysis under dark conditions b) The half-cell configuration, including the epoxy covered photoelectrode (WE), a carbon rod (CE) and the $Hg/HgSO_4$ (RE) used for the dark measurements.

Once the photoelectrode is complete, the electrical connections are applied on the back surface with a tinned copper wire. In case the the wafer surface is unpolished, Gallium–Indium eutectic is applied for surface oxidation protection and to achieve better connection with the conductive liquid metal. Consequently, carbon conductive paste is applied and let until dried and afterwards covered with epoxy resin, in order to be able to fully submerge the electrode in the electrolyte for the dark measurements, without having any other surface uncovered, other than the conducting layer in contact with the electrolyte to avoid shunt resistances. The final photoelectrode to be used for the dark measurements is shown in Figure 20a.

In case the back surface of the wafer is polished, a metal ring is deposited on the semiconductor to allow for back side illumination and the tinned copper wire is attached to the metal ring with carbon conductive paste. The difference lies at the fact that it is possible to use the photoelectrode both for dark and PEC measurements, as it can be inserted in the half or dual-cell and illuminated from either side, as long as it is polished. The metal ring deposited which is usually a gold (Au) contact and can be seen in Figure 21, is formed by using a specially designed mask, which will allow the electrode to be illuminated without the back contact obstructing the light. In the case of GaP (Figure 21b), a thin piece of glass is also placed on top and connected with epoxy resin with the photoelectrode, in order to provide more stability and mechanical strength, since the GaP wafer is 300 μm thick and extremely brittle.

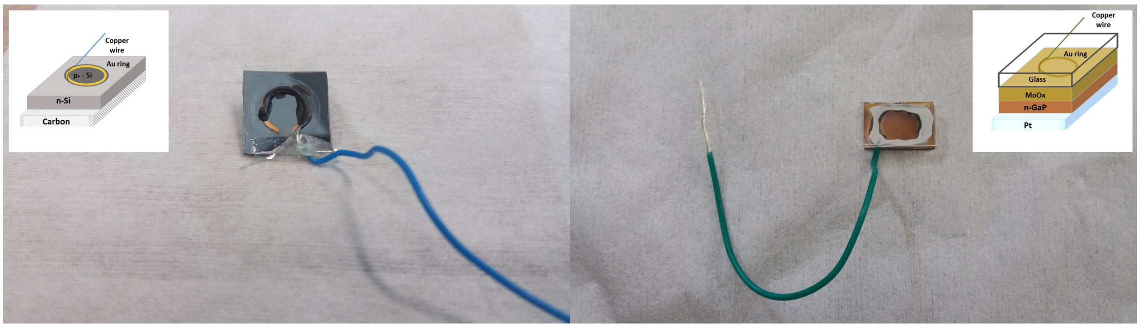

Figure 21: The fabricated photoelectrodeS after thin film deposition and connected with the external circuit through a metal contact ring in the back side, that also allows for illumination of the sample when employed in the PEC cell for a) a Si sample and b) a GaP sample, also including the glass for stability purposes.

3.2.2 Photoelectrochemical cell configurations

Once the photoelectrode is fabricated, it is used in several measurements under dark or illuminated conditions. Based on the thin film configuration and consequently the charge carriers separation and direction, it is placed inside the cell in contact with the proper electrolyte to be reduced or oxidized. This serves as the working electrode (WE). The experiments taking place include the dark cyclic voltammetry and Mott–Schottky analysis, as well as the photoelectrochemical measurements with different illumination modes where feasible. The active illuminated area of the photoelectrode is precisely measured using ImageJ software, in order for conversion of current to current density and equivalent comparison of all samples.

The half-cell configuration includes a carbon rod as counter electrode (CE), covered with silver tape at the connection point and a Hg/HgSO4 reference electrode (RE). It is important that during the measurements the counter and reference electrodes are not in contact. Finally, 30 mL of electrolyte are used for each half-cell measurement in which the three electrode system is submerged (Figure 20b).

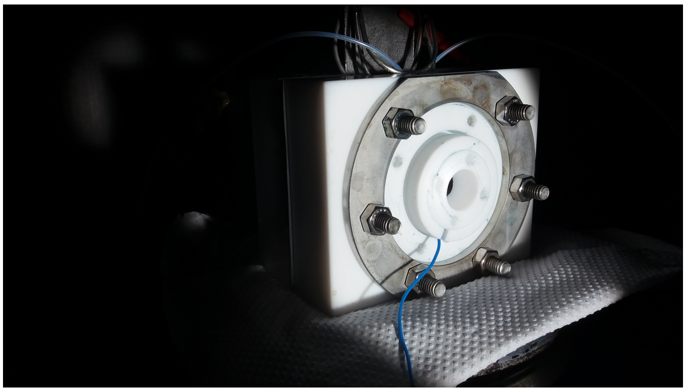

Figure 22: The dual-chamber photoelectrochemical cell during the photocharging experiment of the redox couples. The photoelectrode is illuminated from the back-side with AM1.5 illumination intensity.

In the case of the dual-chamber cell for the photoelectrochemical measurements, apart from the photoelectrode (WE), a carbon rod is used as the reference (RE) and counter (CE) electrode, since in this case the whole cell voltage is significant. Moreover, the redox couples are separated in each of the cell chambers. The separator is a pivotal component for all dual-chamber cells. The main purpose is to isolate the anolyte and catholyte chambers, while allowing the diffusion of ionic charge carriers to not result in a short circuit. In addition, the separator should not be permeable by the electrolytes' active species and have low resistance towards the ionic charge carriers. Such characteristics often come in contrast, since both are dependent on the separator thickness. It is also important however that the separator has good mechanical and electrochemical stability in the media. During the experiments conducted a Nafion 115 ion exchange membrane (IEM) was employed as a separator for the RFB and SRFB operation. The main reasons to use this IEM are its thickness (120 μm) and the low permeability of active species [82].

3.2.3 Dark cyclic voltammetry and Mott-Schottky analysis

The properties and operation of a photoelectrode under dark conditions can already produce important conclusions regarding both the interface between the electrode and the electrolyte, as well as the electronic structure of the device. For this reason, the dark cyclic voltammetry is performed, among other reasons, to derive the photoelectrode's onset potential. This is defined as the point where the thermodynamic and kinetic barriers become downhill and the reaction starts taking place. The result will be a sharp increase in current output, the slope of which can provide useful insight on the Ohmic losses of the device [49]. The objective is to acquire a conducting layer in contact with the electrolyte that will act as an electrocatalyst for a specific reaction, providing an earlier onset potential than the semiconductor would and in addition, result in high current output. Ideally, the reversible electrochemical reaction should be already able to start under dark conditions, without being assisted by the generated photovoltage during the photoelectrochemical measurements. Performing multiple cyclic voltammetry cycles can prove useful for mass transport limiting processes, hysteresis effect in the redox couple kinetics and electrochemical stability of the electrode [50].

Regarding the optimization of the electronic structure of the photoelectrode in contact with the electrolyte, under dark and equilibrium conditions, the semiconductor's Fermi level is aligned with the catalyst layer work function and consequently with the electrolyte's redox potential. The standard redox potential, which corresponds to a variety of densities of the redox states, has a Gaussian distribution and can be described as the electrolyte's Fermi level. In order for this to take place, charge carriers are locally transferred from the semiconductor to the redox species, so that equilibrium is achieved. This results in the formation of a locally charged depletion region creating a bend in the photoelectrode's energy band structure, which is shown in Figure 23a. This locally charged depletion region is compensated for by another locally charged layer in the electrolyte side, however with shorter width due to higher carrier density of the dissolved redox species compared to the semiconductor. The flat band potential is therefore defined as the potential that needs to be applied over the interface in order for the band bending to no longer exist due to the charge carrier depletion in the semiconductor and consequently, the separation of the Fermi levels [83]. The flat band potential is depicted in Figure 23b. Depending on the system configuration, a higher absolute value of the electrolyte's Fermi level, will result in upward band bending of the semiconductor space charge region, allowing for free flow of holes towards the electrolyte, as shown in Figure 23a.

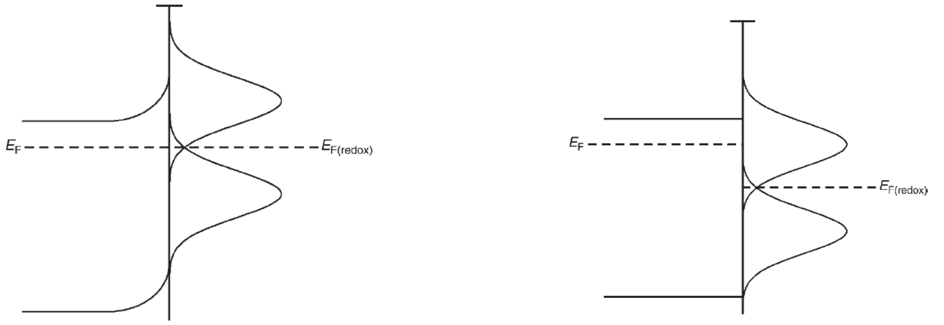

Figure 23: a) The space charge region that is created at the semiconductor-electrolyte interface when in contact and b) the electronic structure of the semiconductor-electrolyte interface is equilibrium when an external bias equal to the flatband potential is applied [83].

The objective is to acquire a conducting layer that will result in a suitable electronic configuration, rendering it possible for the selected charge carriers to be thermodynamically able to flow towards the electrolyte even at dark and equilibrium conditions, that will result in a better current output and therefore device efficiency. The flat band potential can be determined by the Mott-Schottky equation:

$$\frac{1}{C_c^2} = \frac{2}{\epsilon\epsilon_0 A^2 e N_D}(V - V_f - \frac{k_B T}{e}) \tag{34}$$

Where C is the capacitance at the interface, A the contact area, N_D is the number of donors, V is the applied voltage, V_f is the flat band potential, T the absolute temperature and k_B is the Boltzmann constant. The flat band potential can be derived from measuring the inverse square of capacitance as a function of applied voltage and extrapolating the linear part of the curve to meet the x-axis. Therefore, as shown in Figure 24, the interception point is defined as the flat band potential minus the thermal voltage and the linear part's slope corresponds to the number of donors.

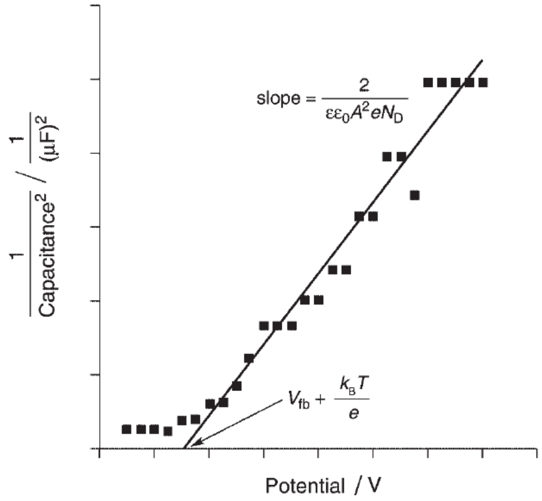

Figure 24: Mott-Schottky analysis to derive the flat band potential and the number of donors [83].

3.2.4 Photoelectrochemical analysis

Following the characterization of the electrode under dark conditions, the photoelectrochemical measurements take place to define the resulting photovoltage and photocurrent output of the device. The photoelectrochemical cell is illuminated under simulated AM1.5 solar irradiation, either from the front or back side, and the photoelectrode properties are measured. The photovoltage shift and therefore the shift in the onset potential is essential for the voltage window produced by the semiconductor and available to charge the electrolyte. As described by the Nernst equation (Equation 4), the redox potential increases with increasing SOC. The photocurrent output is also crucial for the operation of the device, since this will determine the current flow when coupled in the dual cell compartment with the second electrolyte. The J-V curve under illumination can produce useful results on the limiting process in the operation of the system. These can be attributed to ionic mass transport limitations, charge carrier resistive diffusion or recombination losses or other overpotentials due to Ohmic losses. The slope of the curve should ideally be steep, which translates to low ion exchange resistance and electron transport through the contact points, leading to low Ohmic resistance. At high current densities, the limiting process can be the result of concentration polarization where products and reactants have low transport rates. However, the ionic crossover through the membrane is also reduced, maintaining the electrolytes' capacity. The limiting process at low current densities is the activation energy required for the redox reaction to take place. All phenomena involving sorption and desorption of reactants, electron transfer as well as the physical elements of the electrode contribute to this. The polarizability of the counter electrode is also crucial to the operation of the device and therefore the photocurrent output [84].

Using the measured J-V curve under illumination of the half-cell, can be useful to derive the best performing photoelectrode configuration. By constructing the half-cell with the other electrolyte and measuring the same I-V curve with carbon rod electrodes, it is possible to approximate the operating point of the device, and therefore the photocurrent output at 0% SOC, by the overlap between the two half-cell I-V curves. This is matched at a certain operating voltage, which will decrease as the SOC increases during operation.

After the PEC analysis using the half-cell configurations is concluded, the dual-cell configuration is employed for the photocharging experiments. These include using the back-side illuminated photoelectrode in contact with its respective electrolyte, in order to photocharge it. This means that by employing the electrolyte pair, separated by an ion exchange membrane, one of the electrolytes will be oxidized and the other will be reduced. The cell is illuminated and the photocurrent output is monitored over long-term experiments. These allow not only for the photocharging of the device, which can be consequently discharged, but also for the monitoring of the stability of both electrolytes and the photoelectrode. Firstly, from the photoelectrode is expected a relatively stable current generation, which will be gradually reduced over time due to increase in the electrolytes SOC and therefore their charging voltage. Secondly, the redox pair is expected to show long-term charging stability and reversibility. Since the potentiostat only allows for current monitoring while keeping the applied bias at 0 V to achieve unbiased photocharging, the initial (before photocharging) and final (after photocharging) voltage of the cell can be determined by open circuit voltage (OCV) measurements. Once the photocharging is concluded, the SOC is determined by measuring the Absorbance of the charged electrolyte and comparing it with standard solutions.

4. Results

This chapter is divided into two main parts, which describe the results of the research carried out on each SRFB, based on two different photoelectrodes, Silicon (Si) and Gallium phosphide (GaP). The approach followed for each case and the reasoning of how to optimize each photoelectrode is described. Moreover, the experimental results are shown along with their interpretation.

4.1 Si-based SRFB

The approach followed for the Si-based SRFB was the design and realization of a suitable photoelectrode by incorporating a conducting layer in contact with the electrolyte, for the photocharging of an electrolyte couple with high efficiency and achieved SOC. In order to accomplish the desired result, the research firstly focused on studying the properties of various prospective materials that could improve charge transport at the interface. Once the optimal configuration is determined from the experiments in dark conditions, the PEC measurements follow for the deduction of the photoelectrode properties under illumination. The characterization of the different redox couples that were employed is presented and the electronic structure of the device is calculated. Finally, for each photoelectrochemical cell configuration, the photocharging of the electrolytes is shown and the overall performance is evaluated.

4.1.1 Conducting layer electrochemical characterization

For the design and realization of a suitable Si-photoelectrode and the efficient photocharging of an electrolyte couple, the approach followed included research on the charge transfer mechanisms at the interface between the electrolyte and the outer layer of the solid electrode, i.e. the conducting, or catalyst, layer. The purpose for this is ultimately the replacement of platinum (Pt), due to it being a very good catalyst for HER. This can potentially lead to bubbling in a sealed battery, which can cause stability problems and efficiency loss. In order to study the electrochemical reduction reaction of various materials incorporated as conducting layers, current-voltage (J-V) measurements were performed. All prospective materials were sputtered on highly-doped (n^+) silicon (c-Si) substrate (Figure 25 inset). The electrochemical measurements under dark conditions included the CV's and the Mott-Schottky analysis, for the determination of the exact onset and flat band potential, respectively, as well as how the pressure and thickness affect those properties. These are depicted in Figure 25. Some samples also included a sputtered TiO_2 protection layer, prior to the conducting layer. The cathodic reaction of $Fe(CN)_6^{3-/4-}$ involves a single-electron transfer, however a material-dependency can be observed for all cases, either with or without the TiO_2 protection layer.

Specifically, the platinum (Pt) and carbon films (black and blue curve in Figure 25a, respectively) showed a good performance with high onset potential for the reduction reaction of $Fe(CN)_6^{3-}$ at 0% SOC and pH=7, close to the measured $Fe(CN)_6^{3-/4-}$ redox potential. Moreover, while the sample with Pt conducting layer and TiO_2 protection layer showed a similar result to the one with bare-Pt on c-Si sample, combining the carbon conducting layer with the TiO_2 resulted in a huge negative shift of the onset potential of 0.8 V (Figure 25b). TiO_2 (Figure 25a and b, red curve) has been proven to assist the efficient charge carrier transport [22, 85] and its poor activity when combined with carbon cannot be explained by this conductivity research. Furthermore, the bare c-Si sample demonstrated very poor reactivity, which can be attributed to surface deactivation due to oxidation or silanol (Si–O–H) group formation [24, 86]. The sample with a metallic Ti thin (2nm) film presented a huge overpotential of 0.7 V, with respect to $Fe(CN)_6^{3-/4-}$ redox reaction.

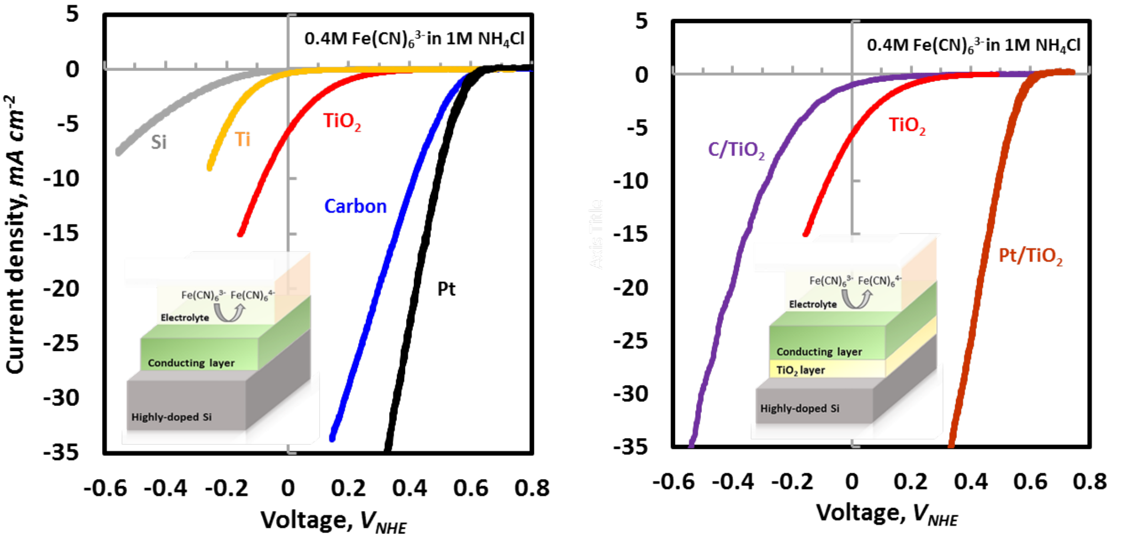

Figure 25: a) Electrochemical CV results for various conducting layers deposited directly on the highly doped Si and b) samples with TiO_2 interlayer deposited on the same substrate. Both measurements were carried out in 0.4M $Fe(CN)_6^{3-}$ with 1M NH_4Cl supporting electrolyte at pH 7 (adjusted by using NH_4OH) (II).

In order to better comprehend how the prospective conducting materials influence the device electronic structure, the Mott-Schottky plot analysis (Figure 26) is performed. When each conducting layer comes in contact with the electrolyte, the work function or Fermi level in dark conditions equilibrates with the redox potential of the reaction. This causes a shift in the Fermi level of the device in equilibrium. In addition, by extrapolating the linear part of the MS plots, the flat band potential can be derived for each case. In the case of bare c-Si, the results are not reliable due to surface deactivation. This can result in increased surface recombination rate and poor charge carrier transfer (Figure 26b). For the case of semiconductor/liquid junction, illustrated in Figure 26c, the flat band is found to be 0.32 V for the TiO_2 in contact with $Fe(CN)_6^{3-}$. This is lower compared to the $Fe(CN)_6^{3-}$ redox potential (0.5 V_{NHE}) and therefore causes an upward band bending (Schottky barrier) at the depletion region (4.2 nm), rendering the electrons unable to tunnel through. Figures 26d and e depict the device electronic band structure of the Pt conducting layer cases with and without the TiO_2 protective layer. No change in potential distribution is assumed at the Pt/$Fe(CN)_6^{3-}$ interface after the Fermi level pinning. The calculated depletion widths for the n^+-Si and TiO_2 is 1.4 and 1.6 nm, respectively. These narrow depletion widths allow for increased electron transfer through the respective layers and towards the electrolyte for the reduction reaction. This claim can also be supported by the steep current slope of the two samples in question, in Figure 25a and b, at an onset potential equal to the $Fe(CN)_6^{3-}$ redox potential (0.475 V_{NHE}).

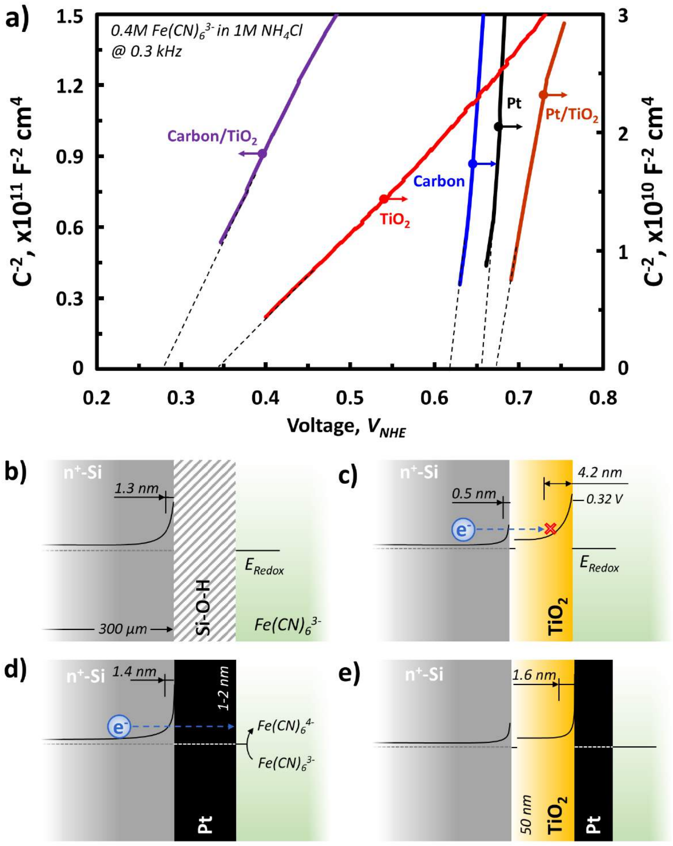

Figure 26: a) Mott-Schottky plots of prepared electrodes with various conducting layers measured at 0.3 kHz in 0.4 M $Fe(CN)_6^{3-}$ with 1 M NH_4Cl supporting electrolyte and b-e) Band alignment of the electrodes in the electrolyte based on the Mott-Schottky measurement and calculation (detail calculation and material parameters can be found in Appendix A) (II).

In spite of the fact that the carbon film showed similar kinetics (Figure 25a) to the Pt and Pt/TiO_2 films, the C/TiO_2 combination had poor kinetics, showing a negative shift of the both V_{on} and E_{FB}, close to that of the bare TiO_2 film. This can be explained by poor carbon coverage of the protecting layer during deposition. In Figure 27a the LSV curves measured for carbon deposited samples with varying deposition conditions are shown. The variables included the effect of deposition time and pressure. The thickness carbon film with deposition time of 10 minutes was found to be 1-2 nm, while the carbon film with deposition time of 60 was found to have a average thickness of 6-8 nm. Figure 27a depicts an increased enhancement of activities with increased deposition time, which can be attributed to the improved coverage of the electrode surface (27b, c and d). As a result, less substrate surface oxidation will take place as a smaller area of the substrate will be exposed to the electrolyte. Moreover, the effect of deposition pressure was studied, both in terms of carbon deposition rate and the effect on the film's porosity (or void density), which has been reported to affect the performance of the conducting layer [87]. The carbon film deposited at lower working pressure (5 bar), exhibited very good activity, with slightly better slope and V_{on} compared to the non-optimized Pt conducting layer (Figure 27a). Correspondingly, the same optimization process can be performed for the Pt layer (Inset of the Figure 27a), where an increased deposition time at lower working pressure can create better coverage of the photoelectrode and lower void density, resulting in improved kinetics compared to the baseline sample.

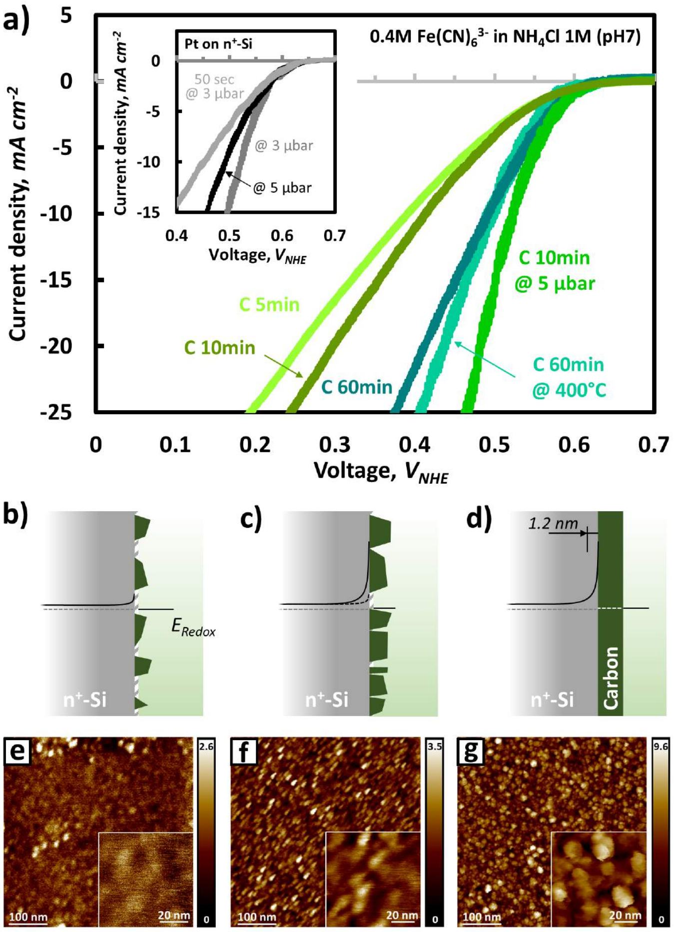

Figure 27: a) LSV curves of c-Si electrodes with carbon conducting layer deposited under various conditions (i.e., deposition duration and working pressure of the sputtering). LSVs for the samples with Pt conducting layers are also demonstrated as an inset. For notational simplicity, "min" and "sec", "μbar" correspond to the deposition time and pressure of the sputtering chamber, respectively. b-d) The cross-sectional schematic of the electrode with various carbon thickness coverage based on deposition time, are illustrated. e-g) The atomic force microscopy (AFM) analysis for sample surface morphology analysis (II).

The atomic force microscopy (AFM) analysis (Figure 27e-g) demonstrate how the surface morphology changes over the carbon deposition time, and confirmed the correlation between the carbon coverage and duration of the deposition. The maximum height difference between c-Si substrate and valleys of crests (i.e., carbon cluster with brighter colour) significantly changes from 2.6 to 9.6 nm for the sample with 60 min deposited carbon (Fig 3g). One can observe the carbon deposition resulted in rather well distributed particle or island formation, which changes its size with deposition time.

4.1.2 Photoelectrochemical analysis

Following the dark measurements for the optimization of the solid-electrolyte interface, the device behaviour is studied under illumination. The half-cell configuration is employed in order to figure out the device configuration with the best performance that will provide two crucial outputs. The first output is the induced photovoltage shift, which should ideally give a big voltage window in order to be able to sufficiently charge the electrolyte couple based on the redox potentials. The second output is photocurrent output, which means efficient charge carrier transport, low device series resistance and steep current curve in order for the saturation current density to be reached withing the voltage window for the electrolyte charging. For this purpose, apart from the various samples employed with Pt or Carbon conducting layers, some widely studied ETL and HTL thin films (TiO_2 and NiO_x respectively) are employed and tested, in order to further increase the photocurrent output. Furthermore, some different silicon doping wafers are tested, again in terms of optimal band diagram configurations. Firstly, in the cathodic photoelectrodes (Figure 28a), the highly doped $n^{++}np^{++} - Si$ (olive curve) showed the most steep curve compared with the different doping Si wafers. However, the fact that the onset potential proved to be poor can be attributed to high Schottky barrier formation at the interface between the conducting layer and the base semiconductor. The optimal result was derived form the Pt/Ti/np+-Si/Au (blue curve) which showed a proper photovoltage of about 0.5 V available to charge the electrolyte couple, as well as high photocurent output. A similar result was obtained from the same sample by replacing Pt/Ti with Carbon conducting layer (light blue curve), a result well matched with the previous dark analysis. Incorporating NiO_x (purple curve in Figure 28a and green curve in Figure 28b), a popular HTL material for Si, showed a decrease in photocurrent output. Therefore better deposition conditions optimization is required for the specific Si wafer.

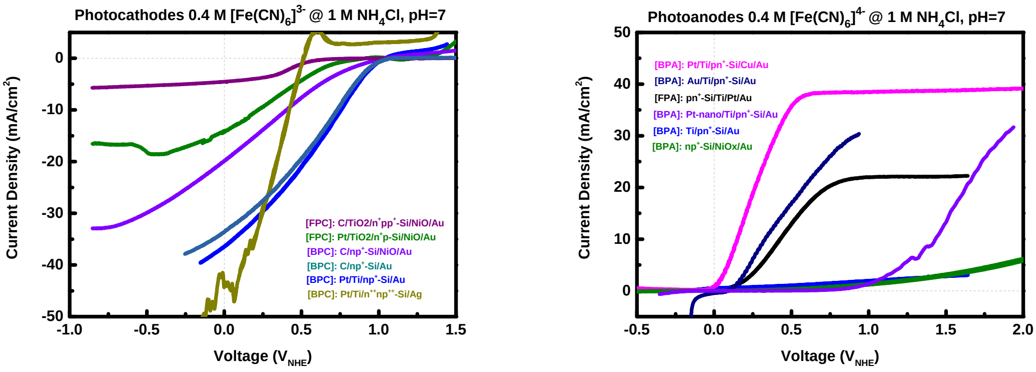

Figure 28: Photoelectrochemical CV results for various a) cathodic and b) anodic photoelectrode device configurations under illumination in contact with 0.4M $Fe(CN)_6^{3-}$ with 1M NH_4Cl supporting electrolyte at pH 7. Insets show the photoelectrode configurations employed. For each configuration, "F" denotes front-side illumination, through the electrolyte, while "B" stands for back-side illumination. "PC" stands for "photocathode" and "PA" for photoanode.

Similarly for Figure 28b, the anodic photoelectrodes are shown. The optimal result was again obtained for the same electrode as the photocathode, however with the reverse configuration of Pt/Ti/pn+-Si/Au (pink curve). The fact that the onset potential is exactly 0.5 V, providing a large enough voltage window, as well as the very steep photocurrent increase that reaches its saturation current density fast, can be attributed to lower build-in voltage and/or lower Schottky barrier formation at the interface between the conducting layer and the electrolyte. In addition, this could be enhanced by the fact that the semiconductor surfaces were both polished and no etching was needed to pre-treat an unpolished side for a thin film deposition, which is the case for the photocathode Si wafer. The other configurations shown correspond to lower photovoltage and current output, were the effect of back and front side illumination mode can be examined. In every case, front side illumination corresponds to lower parameter outputs compared to back side illumination, due to both parasitic absorption from the electrolyte and the fact of where the p-n junction is located relative to the base semiconductor thickness. The device electronic configurations of the best performing samples, for both cathode and anode, are presented and discussed in Chapter 5.1. The fact that both cathodic and anodic photoelectrodes are studied and tested, is the availability of suitable electrolyte couples in terms of toxicity and price, that will enable the efficient operation of the SRFB.

One consideration is the illumination mode and how the highest current density can be achieved. This applies in every case and concerns the losses associated with the device operation during the charge carrier generation. Specifically, as shown in Figure 29a and b, for the Si and GaP based photoelectrodes respectively, illuminating from the back side is more efficient than the front side in terms of current output and lowering over potential losses.

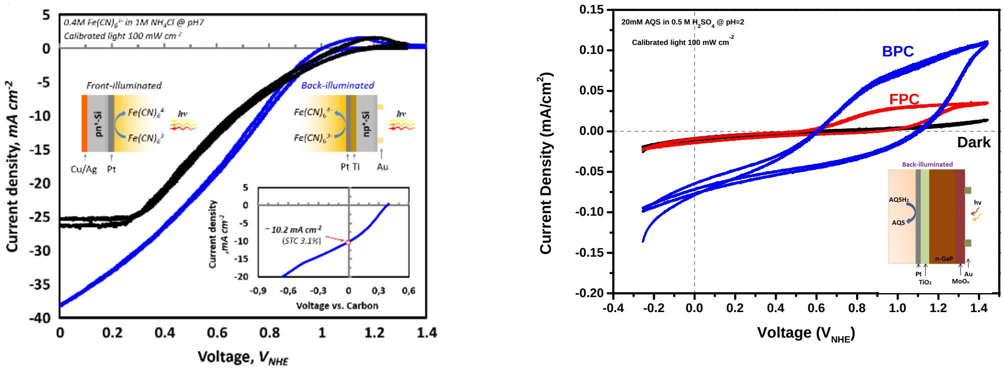

Figure 29: aa) The experimental Si-based LSV curve, in the case of a 0.4 M ferricyanide electrolyte, a front-side illuminated configuration results in a significantly lower saturation photocurrent. The inset shows the LSV for a dual-electrolyte cell (i.e., 2-electrode configuration), resulting in a current density of 10.2 $mAcm^{-2}$, corresponding to an estimated STC of 3.1% at a cell voltage of 300 mV (I) and b) CV curves of the same GaP-based configuration illuminated form front and back side and the importance of back-side (blue curve) to front-side (red curve) illumination in terms of current output. Optical losses from parasitic absorption and the junction location in the device need to be considered (III).

As seen in Figure 29a, the saturation current of the front-side illuminated Si-device is significantly lower than that of the back-illuminated case, despite an otherwise almost identical setup. Figure 29b also illustrates the lower current output during the CV of the front (red curve) compared to the back (blue curve) side illumination. The reason for this is twofold. The first is the fact that there will be no parasitic absorption from the other components of the device, such as electrolyte, conducting layer and possibly other thin films incorporated on the device for efficient charge carrier separation. Secondly, the base semiconductor is usually the thickest layer and it is important to illuminate from the side at which the junction is closest, to enable the more efficient generation and separation of charge carrier and prevent recombination over high diffusion lengths. These can lead to higher kinetic over potentials and therefore efficiency loss.Once the optimal configurations for each case (cathode and anode) are found, these electrodes are employed in the dual cell configuration that is required to charge the SRFB.

4.1.3 Si-based SRFB photocharging

Photo-charging tests were performed with both 3-electrode configuration for half-cell reactions (Figure 31b and d), and two-electrode setup with different electrolytes separated by Nafion membrane (Figure 31c and e). For the following series of experiments the optimal photoelectrode configuration are employed based on their optimization described in the previous sections. Those consist of of the photoanode structure of $Pt/Ti/pn^{+} - Si/Au$ as well as the photocathode structure of $C/np^{+} - Si/Au$. The electrolytes employed each time were chosen based on the most crucial parameters, which are their redox potential, price, stability, toxicity and availability. Out of multiple inorganic and organic electrolytes with greatly varying properties, the results described in this section refer to two specific SRFB configurations which showed the highest charging efficiency. For the complete list of of SRFB configurations employed, testing procedures and further supporting information, the reader is referred to Appendix D.

Both Si photoelectrodes developed can ultimately provide a maximum of 0.5 V photovoltage. It is therefore crucial to select the optimal redox couple that will enable a high photocharging efficiency and SOC. For this purpose, the CV's electrolytes employed are shown in Figure 31a. Potassium hexacyanoferrate (II/III) was used for both cases, since the conducting layer optimization started with this electrolyte, and consequently TEMPO-sulfate and copper(II) sulfate was employed in combination with potassium hexacyanoferrate for the photoanode and photocathode, respectively. The SRFB of the photoanode couple exhibited a cell voltage of 0.4 V while the SRFB of the photocathode showed 0.35 V.

The redox reactions for the photocathode Si-SRFB are:

$$Fe(CN)_6^{3-} + e^- \rightleftharpoons Fe(CN)_6^{4-}, E_{redox} = 0.475V_{NHE} \tag{35}$$

$$Tempo - sulfate^0 \rightleftharpoons Tempo - sulfate^+ + e^-, E_{redox} = 0.82V_{NHE} \tag{36}$$

So the overall cell reaction is:

$$Fe(CN)_6^{3-} + Tempo - sulfate^0 \rightleftharpoons Fe(CN)_6^{4-} + Tempo - sulfate^+ \tag{37}$$

Likewise, the redox reactions for the photoanode Si-SRFB are:

$$Fe(CN)_6^{4-} \rightleftharpoons Fe(CN)_6^{3-} + e^-, E_{redox} = 0.475V_{NHE} \tag{38}$$

While for the cathodic side, the reactions can vary based on the conditions under which the SRFB is operated.

$$Cu^{2+} + e^- \rightleftharpoons Cu^{1+} \tag{39}$$

$$Cu^{1+} + e^- \rightleftharpoons Cu_s \tag{40}$$

$$Cu^{2+} + 2e^- \rightleftharpoons Cu_s, E_{redox} = 0.08V_{NHE} \tag{41}$$

So the overall cell reaction is:

$$2Fe(CN)_6^{4-} + Cu^{2+} \rightleftharpoons 2Fe(CN)_6^{3-} + Cu_s \tag{42}$$

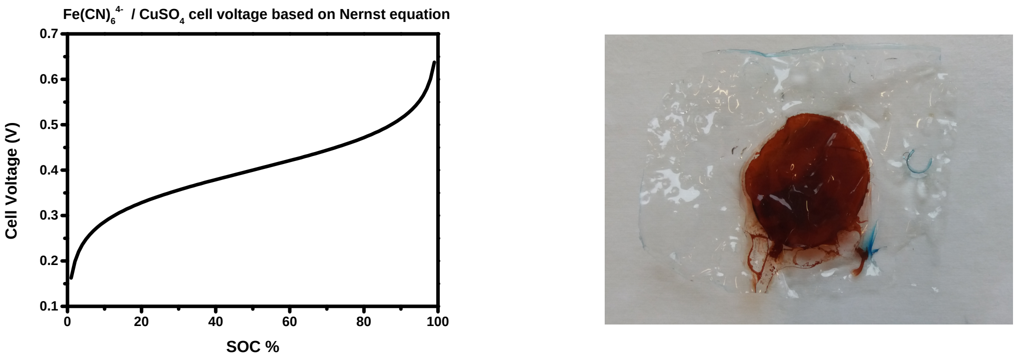

Figure 30: a) The projected cell voltage of the $CuSO_4/\ Fe(CN)_6^{4-}$ cell based on the theoretical calculation of the Nernst equation and b) the IEM after the chronoamperometry measurement where copper ions precipitation can be noticed on the membrane which affects the permselectivity and therefore the device efficiency.

Furthermore, the pH conditions at which the cell is operating is of outmost importance. This can affect the redox potential, the electrode stability as well as the selectivity towards certain products. Incorporating copper sulfate since it has a suitable redox potential resulted in solid copper ($Cu_{(s)}$) formation, which rendered the consecutive cell discharge impossible. Introducing NH_4OH to control the pH towards more neutral values, resulted in other precipitation form of copper(II) hydroxide ($Cu(OH)_2$). The solid copper formation can be seen in the IEM after the chronoamperometry (Figure 30b). This is another cause of efficiency losses, which deteriorates over time. The pH of the Cu^{2+} electrolyte was adjusted to 2 in order to prevent the precipitation of solid copper. Under the conditions used and due to lack of RFB optimization, the main reaction expected to take place is the formattion of solid copper with two-electron transfer. Information on the proper copper RFB conditions can be found on Appendix D. Figure 31b illustrates the LSV curve obtained for the photocathode either with $Pt/Ti/pn^+ - Si$ (black curve) or $C/pn^+ - Si$ (green curve), which showed almost identical results, overlapped with the respective LSV curve of TEMPO-sulfate employing the anodic half cell with a three electrode measurement (two carbon rods and one reference). From the overlap of the two curves, the current output can be estimated, by omitting the IEM induced overpotential. Figure 31c illustrates the photocharge profiles for the first 20 h using a C/np+-Si||Carbon-rod configuration with ferricyanide/TEMPO-sulfate. The charging photocurrent for the photocathode starts at 11.6 $mAcm^{-2}$ and decreases to 8.7 $mAcm^{-2}$; the corresponding initial and final values for the ferricyanide/Br2/Br- cell are 2.0 and 0.4 mA cm-2 (Figure 31b black curve). The unequal photocurrent density between the two setups is due to a redox potential shift leading to the cell voltage increase (from 0.34 to 0.92 V) that makes the operating current density (intersection between the polarization curves in Figure 31b) lowered. Theoretically 0.51 V from the photocathode is insufficient to charge the ferricyanide/Br2/Br- battery without a bias potential. The low photocharging current from the ferricyanide/Br2/Br- cell is only observable at low SOC%, where the required potential is quite low according to the Nernst equation. Similarly, Figure 31d depicts the two half-cell configurations for which the LSV's are measured and overlapped in order to approximate the photocurrent output. Here it can be noticed that the current is much higher compared to the photocathode and this is attributed to the low series resistance and therefore steep current increase of the anodic photoelectrode. This can be explained by better band alignment of the device, due to different n type donor density and p^+ type acceptor density.

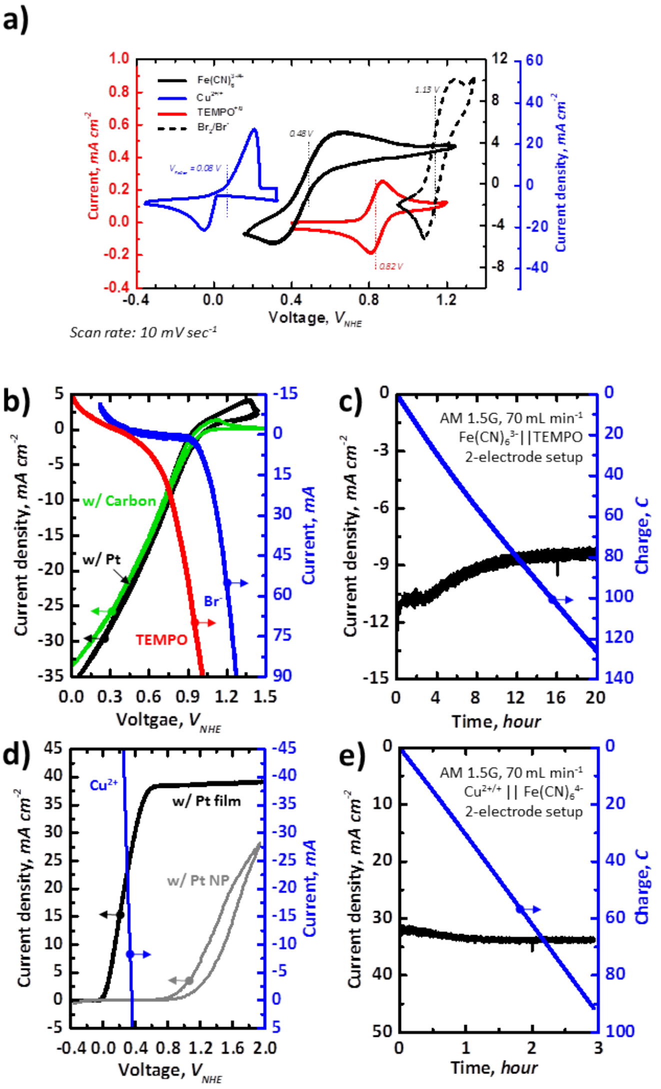

Figure 31: a) CV's of 2 mM solutions of TEMPO-sulfate (red), $CuSO_4$ (blue solid), $K_3Fe(CN)^6$ (black) and NH_4Br (blue dased), using a scan rate of 10 $mVsec^{-1}$. For the TEMPO-sulfate, $K_3Fe(CN)^6$ and NH_4Br, NH_4Cl was used as a supporting electrolyte, and the pH was adjusted to 7. Note that pH of the Cu^{2+} electrolyte was adjusted to 2 in order to prevent the precipitation of solid copper. b) Overlaid current-voltage curves measured in a three-electrode experiment for the individual photocathodes and anode (carbon felt). $C/pn^{+}-Si$ and $Pt/pn^{+}-Si$ in a 0.4M $Fe(CN)_6^{3-}$ and 1M NH_4Cl supporting electrolyte; while carbon felt anode in a 0.4M $TEMPO^{-}$ and 0.2M Br^{-} with an 1M NH_4Cl solution. c) Chronoamperometry and accumulated charge of the photocathode with Carbon conducting layer, under the same electrolyte conditions, but with two-electrode configuration. d) Overlaid current-voltage curves (three-electrode configuration) for the individual photoanodes and carbon felt cathode. The pn^{+}-Si photocathodes with a Pt thin film (1-2 nm) and Pt nanoparticles (200 $ngcm^{-2}$) and carbon felt cathode for 0.4M Cu^{2+} in the same electrolyte condition used for the figure (31b). e) Chronoamperometry and accumulated charge of the photoanode with Pt with carbon felt cathode with two-electrode configuration (II).

In spite of the facile kinetics in the photoanode case, Figure 31d reveals an interesting feature. A photoanode employed with Pt nanoparticles (loading of 200 $ng \cdot cm^{-2}$ as a conducting layer was produced. The LSV curve of the sample with Pt nanoparticles (grey) is described accurately at low V_{OC} with slow kinetics and low current density. It can be therefore concluded that deactivated substrate without conducting particles can hinder the facile carrier transport, especially in the case of not sufficient surface coverage, as shown for carbon in Figure 27. Note that both Pt film and nanoparticles were formed after the surface cleaning step (etching) to prevent the deactivation of the interface between the Si substrate and the conducting material. Finally, Figure 31e shows the chronoamperometry of the copper-ferrous cell, where a stable and quite high current output of 35 mA/cm^2, is observed over a period of 3 hours, resulting in an efficient photocharging process, however with solid copper formation. This high photocurrent probably is attributed to the direct light absorption without any parasitic optical loss by the electrolyte and other layers including protection, Pt conducting layers, and acrylic window, which are unavoidable in front-side illumination conditions, as well as on the improved photoelectrode electronic structure. For each chronoamperometry curve, the SOC% can be approximated either from electrolyte absorbance measurement and comparison with standard solution, or from the total charge inserted. At the measured SOC%, the cell voltage can be measured either with an OCP measurement (and compared with the initial OCP, Appendix D) or it can be approximated by the Nernst equation. Using the measured SOC%, the cross-referenced cell voltage and the photocurrent output at that moment, the estimated charging efficiency can be approximated for each SRFB system. This can be described as:

$$n_C = \frac{U_{cell@SOC} \cdot J_{measured@SOC}}{W_{in}} \tag{43}$$

Where W_{in} is the input power of 100 mW/cm^2. The results for each chronoamperometry curve of Figure 55 are presented in Tables 1 and 2 below, for the photocathode and photoanode, respectively.

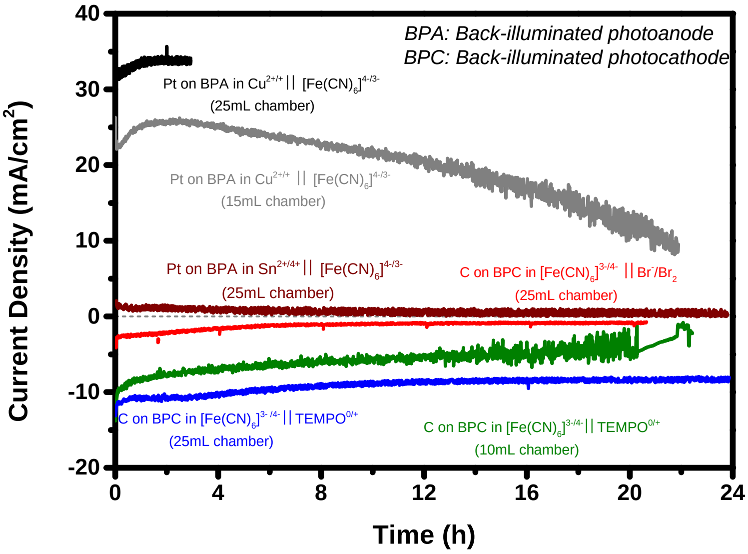

Figure 32: All the chronoamperometry measurements employing various SRFB configurations

By examining the performance of the different photoelectrode structures and correlating it with the optimal SRFB device performance, some useful inferences can be derived. Figure 55 depicts the chronoamperometry measurements performed for all SRFB structures used, by incorporating the best performing electrodes and different electrolytes. The electrolyte redox reactions can be found in Appendix D. Here it can be seen how the redox couples employed, practically affect the photocurrent output. Firstly, it is evident that suitable electrolyte selection can lead to very high charging efficiencies of 9.4% ($CuSO_4/\ Fe(CN)_6^{4-}$ cell, purple curve). The redox potential of the electrolyte couples close to 0.4 V appear to have the best performance, as also seen in Figure 44. This photoelectrochemical charging efficiency for the Cu-sulfate | | Ferrocyanide cell is the highest among all the SRFBs with a single photon-device so far reported. On the contrary, employing electrolytes with very high cell potential practically prevented the photoelectrode from being able to charge the cell unbiased and only allowed for a minimal photocurrent output from the photoelectrode at low SOC% ($NH_4Br/\ Fe(CN)_6^{3-}$ cell, green curve). Naturally, the Ferricyanide | | Br2/Br- combination case only showed 0.32% at 1% SOC due to discrepancy between the photovoltage and cell voltage to drive the chemical reaction. Also, it is clear that in most cases there is a gradual current decrease. This can be explained by the rise of cell voltage due to Nernst equation, as well as due to precipitation from increased membrane and solution resistance and evaporation of a portion of the electrolyte during long operation time (which promptly correlates with the current output due to available charge carrier diffusion paths in Figure 55). The $SnCl_4/\ Fe(CN)_6^{4-}$ cell (black curve) employed also showed a poor performance similar to NH_4Br, for the same reasons (information on $SnCl_4$ can be found in Appendix D).

C/np$^+$ $- Si/Au$ **photocathode**	**TEMPO / Fe(CN)$_6^{3-}$ Ecell=0.35**	**TEMPO / Fe(CN)$_6^{3-}$ Ecell=0.35**	**NH$_4$**$Br/Fe(CN)_6^{3-}$ **Ecell=0.6**
Concentration [M]	0.4	0.4	0.4
Volume [mL]	25	10	25
Charge [C]	155/965	88/385	20/965
SOC [%]	15	22	1
Charging efficiency [%] **(@ indicated SOC)**	2.1 (@ 15% SOC)	1.7 (@ 20% SOC)	0.32 (@ 1% SOC)

Table 1: Chronoamperometry data for Si-based photocathode SRFB's with their corresponding electrolytes

Pt/Ti/pn$^+$ $- Si/Au$ **photoanode**	**SnCl$_4$**$/Fe(CN)_6^{4-}$ **Ecell=0.98**	**CuSO$_4$**$/Fe(CN)_6^{4-}$ **Ecell=0.4**	**CuSO$_4$**$/Fe(CN)_6^{4-}$ **Ecell=0.4**
Concentration [M]	0.4	0.4	0.4
Volume [mL]	25	15	25
Charge [C]	10/965	398/598	93/965
SOC [%]	-	63	9
Charging efficiency [%] **(@ indicated SOC)**	-	7.7 (@ 50% SOC)	9.4 (@ 10% SOC)

Table 2: Chronoamperometry data for Si-based photoanode SRFB's with their corresponding electrolytes

4.2 GaP-based SRFB

The GaP-based photo device was developed following a different approach compared to the Si-based SRFB. In the present case, research was conducted on MoO_x as a promising material to enable and improve hole extraction and to prevent recombination. A full characterization of the thin layer and optimization of the conditions used during formation is presented. These include studies on the electronic structure of the thin film and its alignment with GaP, XPS and XRD results, conductivity measurements and photovoltaic devices fabrication for the complementary solar cell measurements. The results under dark and illuminated conditions are shown, along with the characterization of the redox couples employed. Finally, the SRFB photocharging is performed and the charging efficiency is assessed.

4.2.1 MoOx as HTL

Efficient carrier transfer at the interface is a key to energy conversion devices, such as photovoltaic (PV) and photoelectrochemical (PEC) applications. This is enabled through dopant atoms, which are introduced in each surface region of the semiconductor, by creating uneven conductivity for each respective charge carrier, such as homogenous pn-junction devices. An alternate option to separate the photogenerated charge carriers is to apply thin film materials other than absorber semiconductor (i.e., heterogeneous). This contact type, with thin and almost transparent metal oxides can bring less parasitic optical loss and the relatively lower process temperature for forming these metal oxide can minimize the possible thermal damage of the device. Among the multitudinous transition metal oxides, molybdenum oxide (hereinafter MoOX) integrated to the n-type silicon has proven beneficial in hole-selective transfer layer (HTL), proven in the work of Battaglia et. al. MoOX is a wide band-gap (3.0 eV) semiconductor with high electron affinity and ionization energy and exhibits low parasitic absorption, an important consideration in maximizing the photocurrent output. Under light irradiance, the generated charge carriers will flow towards the path of least resistance, opting for a decrease in their free energy. The energy level alignment is, therefore, the first and foremost parameter, contributing to efficient charge separation and reduced interface recombination. The MoO_x has sub-stoichiometric phases which inherently form a mid-gap state close to the conduction band (CB). In many cases, MoO_x has been studied as a HTL based on its induced mid-gap state. Researches above-described have focused on the effect of process parameters, such as thickness, composition and temperature to find the optimal conditions to acquire high conversion efficiency. Here the influence of deposition parameters of MoO_x on the band alignment with wide band-gap GaP and electrical behaviour is demonstrated.

4.2.1.1 UV-Vis

The optical properties of the MoOX thin films were tested by UV-Vis spectroscopy using a Perkin-Elmer Lambda 900 and their thickness was determined by a interferometric surface profiler (Dektak 3) to determine their band gap. MoO_x thin films with a nominal thickness of 150 nm were prepared on FTO glass substrate at various O_2/Ar ratio (6/14, 7/13 and 8/12 sccm) to determine the effect of composition ratio on the transmittance of the obtained thin films and therefore their optical band gap. As shown in Figure 33, all samples showed quite high transmittance ($>$ 80% in visible range) and the band gap was estimated to be 2.75-2.83 eV according to the Tauc plot (inset) with indirect allowed transition (i.e., n = $\frac{1}{2}$), which is proportional to the oxygen flow ratio. This is a result of the higher proportion of stoichiometric molybdenum trioxide phases with wide absorption edge.

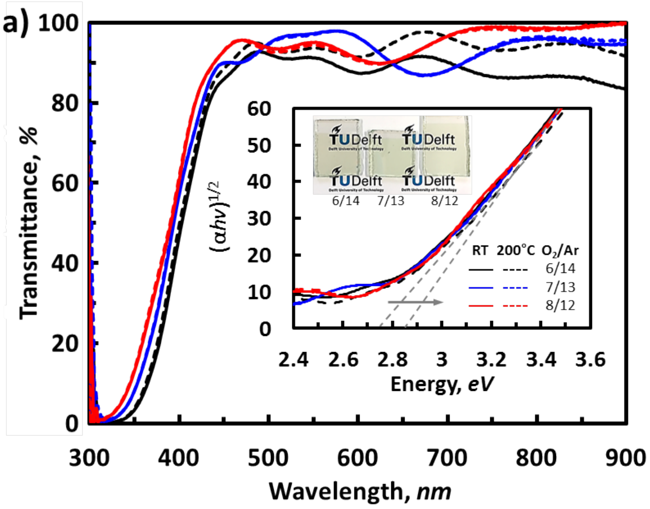

Figure 33: UV-Vis transmittance spectra of MoO_x deposited with various O_2/Ar gas flow ratio on a FTO-coated glass substrate. The signal from the quartz substrate was subtracted as a background spectrum. Tauc plot converted from the transmittance to estimate its band gap also shown as an inset along with optical photo of the samples (III).

In addition, an increase in transmittance was observed after the post-deposition annealing process in case of the MoO_x with O2/Ar ratio of 6/14 sccm, along with a slight increase in band gap has been identified. This can be due to the Burstein–Moss shift, caused by the Fermi-level shift to higher energy in a heavily doped semiconductor, due to the populated states near the conduction band [88]. Generally, non-stoichiometric oxides with excess metal cations due to insufficient oxygen during the deposition, results in highly doped oxide layer, and the sample with low oxygen ratio (i.e., 6/14 sccm) is in this case as more oxygen vacancies are formed.

4.2.1.2 XRD/XPS studies

The structural properties of the films were examined using X-ray diffraction (XRD; Bruker D8 Advance) and X-ray photoelectron spectroscopy (XPS; Thermo Scientific, K-alpha). The structural properties of MoO_x thin films were characterized in order to analyse the composition and the orientation of the films. The X-ray diffraction is therefore examined, for both the as-deposited and the post-deposition annealed samples. Figure 34 depicts the diffraction peaks of the MoO_x deposited on FTO glass substrate. As shown with the dashed line, the film seems to keep its amorphous nature for both as-deposited and annealed sample at annealing temperature of 200°C. The characteristic peaks related to MoO_x form a rather weak and broad signal situated around 30-32°in which the (204) plane assigned to hexagonal MoO_3 phase. The distinct reflections at 2θ of 26.3°may indicate the formation of h-MoO_3 with (210) plane. However, the strong overlap with the characteristic peaks from the FTO coated substrate makes it hard to distinguish in the XRD data. Through this peak overlap, with Reference Intensity Ratio between the 26.3°and 37.8°implies existence of the (210) plane for all formed MoO_x samples. It is worth to note that the peak at 26.3°may be derived from the MoO_2 (111) plane, and thus the XPS analysis was conducted to investigate the composition of the films.

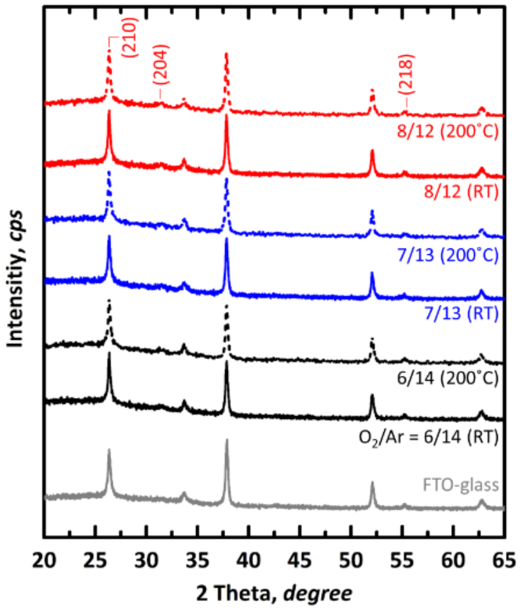

Figure 34: XRD patterns of MoO_x grown at room temperature and post-annealed at 200°C (with N_2 flow) and with various O_2/Ar gas flow ratios, plotted with spectra from the FTO coated glass (III).

The MoO_x thin films were examined using X-ray Photoelectron Spectroscopy (XPS) to obtain quantitative data regarding their chemical states and surface morphology as well as to determine their electronic structure. As shown in Figure 35a, the valence band (VB) of the films can be reduced slightly by thermal post-annealing in ambient N_2 as demonstrated in the stacked spectra. This VB shift towards the Fermi level is observed for all samples, regardless of the oxygen ratio. The valence band spectra is known to be dominated by the mostly O 2p derived bands, and no appreciable shift upon possible creation of oxygen vacancies during the heat-treatment has been observed, indicating that oxygen vacancies are not acting as shallow donors in MoO_x, as shown in previous study [89].

The sputtered MoO_x films were then exposed to ion-beam to remove the adventitious carbon at the surface. Battaglia et al. demonstrated a negative shift of the VB position after a UV-ozone exposure on their evaporated MoO_x films to remove the carbonaceous contamination [89]. Naturally, the samples exposed to ambient conditions may have different oxidation state from the as-deposited one. It is evident from survey scans that the untreated samples have distinct peaks that correspond to carbon peaks (C 1s scan) while cleaned sample show a significantly decreased carbon trace. Though the MoO_x film was formed using a sputtering technique and cleaned the surface with an ion-beam, it appears that the trend in VB remained the same. Exploring the cleaned surface is particularly important from a device fabrication viewpoint where the hole transfer layer is deposited in the vacuum forming the MoO_x/GaP interface. The small defect band visible at a binding energy of around 1.5 eV is also of particular interest. This mid-gap defect state has been observed in other XPS studies on MoO_x films. Although its origin has remained a source of controversy, identifying its position is important for understanding the hole transfer pathway in band alignment of the full device. Its spectral weight suppressed with post-annealing treatment (Figure 35a and b, dotted line), and this decrease may be due to the carbon contamination from the probably not thoroughly cleaned quartz tube.

However, surface cleaning by ion-beam shallow etching reveals that the center of defect state drifts apart from the Fermi level.

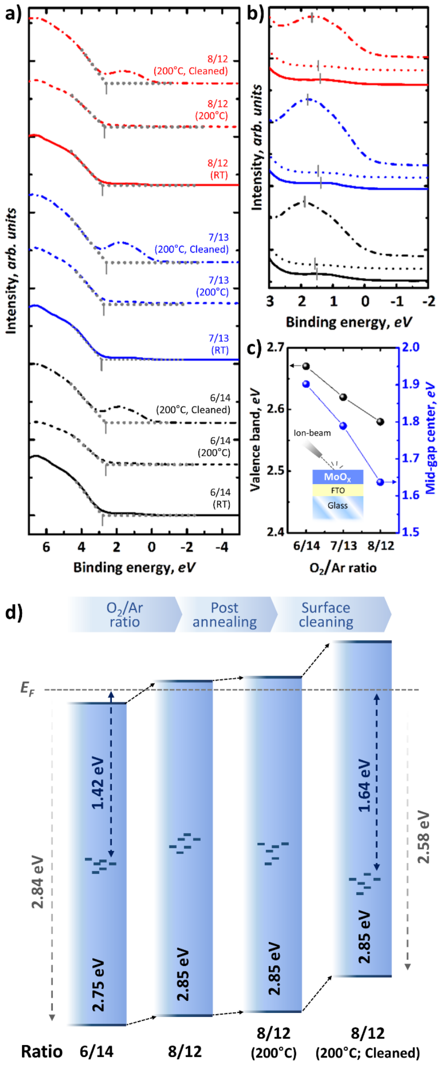

Figure 35: a) X-ray photoelectron valence band (VB) spectra of the MoO_x film prepared by sputter deposition under various $O_2/$Ar mixture ratio. Spectra from the post-annealed sample and the one with surface cleaning treatment are plotted with dotted and dot-dash line, respectively. b) Zoomed-in plots of the relevant region for the mid-gap states in the VB. c) Extracted VB and mid-gap center values from the annealed and cleaned samples and d) illustration of band edge diagrams in undefined scale based on the extracted values of mid-gap states and VB edge (III).

The broad peak within 0.5-2.5 eV can be related to the presence of Mo^{4+} that contributes to the mid-gap states near 2 eV as also observed in Figure 36. In this context, the shift of the defect state towards the Fermi level can be understood by the fact that relatively lower number of oxygen vacancy in the MoO_x films formed at high $O_2/$Ar flow ratio, may suppress the Mo^{4+} from the MoO_2 phase (Figure 35c).

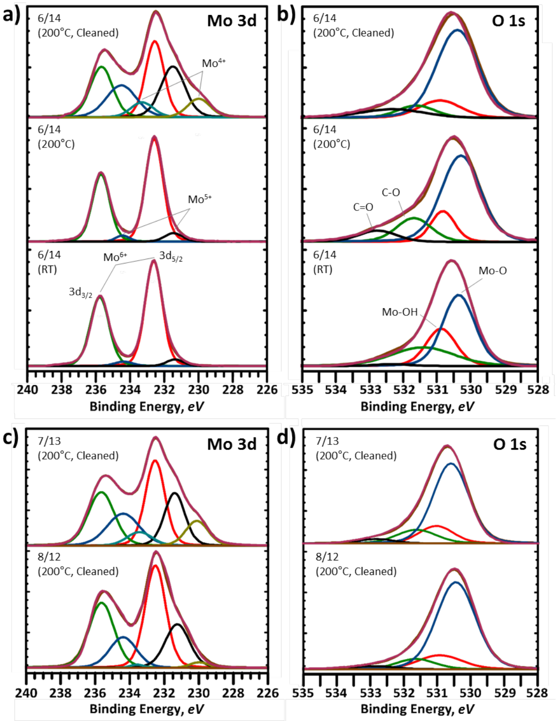

Figure 36: XPS spectra of the a) Mo 3d and b) O 1s from the samples with various deposition and post-treatment conditions (O_2/Ar ratio of 6/14, c) 7/13 and d) 8/12) are shown with the deconvoluted peak assignments (III).

4.2.1.3 Resistivity measurements and solar cell characterization

The current-voltage measurement was conducted using a potentiostat PARSTAT MC (Princeton Applied Research, AMETEK). The photovoltaic properties have been measured under simulated AM1.5 solar irradiation (100 $\frac{mW}{cm^2}$) using a Newport Sol3A Class AAA solar simulator with 450W xenon short arc lamp.

J-V measurements were performed in order to study the electrical conductivity at room temperature of the as-deposited and post-treated MoO_x films under various O_2/Ar ratio on FTO-coated glass followed deposition of Cu (50 nm) and Au (50 nm) films. The results from the devices investigated under direct bias between the FTO (positive) and Au (negative) poles are shown in Figure 37a, which displays the J-V curves of the devices fabricated at various O_2/Ar mixture ratios. The overall conductivity of the MoO_x is estimated to be about $2-4\cdot 10^{-6} Scm^{-1}$ from the J-V measurement. The conductivity was extracted under low bias potential (up to 1 V) in order to compare the conductivity of the whole set of samples. However, negigible changes were observed. As explained by Oh et al., stoichiometric MoO_3 is a transparent and insulating material, whereas MoO_2 is a metal-like conductor [90]. The electrical conductivities of MoO_3 and MoO_2 have been reported to be in range of $10^{-10}-10^{-11} Scm^{-1}$ and $10^5-10^4 Scm^{-1}$, respectively. Here, the results from both XPS and electrical studies point out that mixed phase of stoichiometric MoO_3 and substoichiometric MoO_x results in moderate conductivities of magnitude of $10^{-6} Scm^{-1}$.

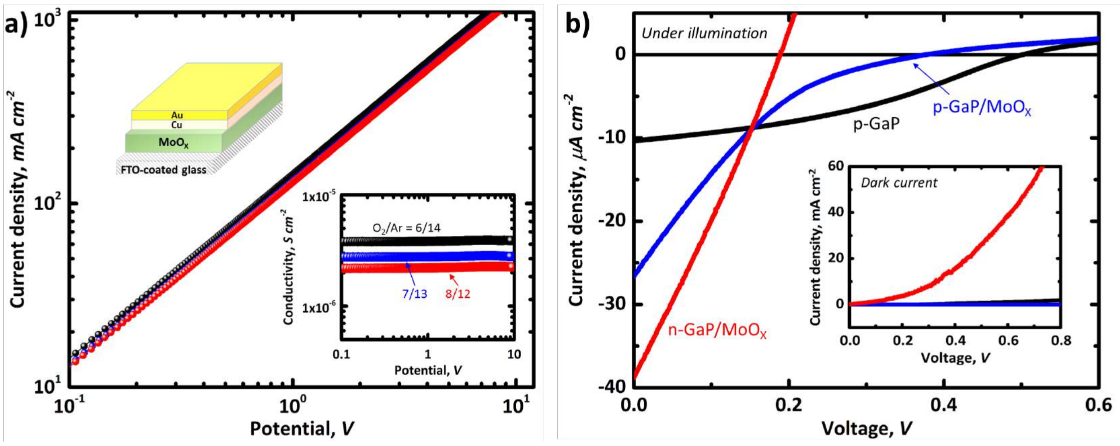

Figure 37: a) J-V curves (in dark) of the MoO_x devices as a function of the O_2/Ar ratio (6/14 black; 7/13 blue; 8/12 red). The inset shows the extracted conductivities from the J-V curve using a Ohm's law. The device schematic used to measure the dark J-V is also illustrated (upper left). b) Results from n and p- type GaP fabricated solar cell devices with or without MoO_x under the light (III).

Figure 37b illustrates the J-V curves of the GaP based photo-device prepared with and without the MoO_x thin layer, under illumination. It is worth noting that indium tin oxide film and Cu-wire were used to make electrical contacts at both ends. The bare p-GaP device showed an open circuit voltage (V_{OC}) of 0.5 V, while for the MoO_x added sample it is reduced to 0.4 V. Moreover, the short circuit current (J_{SC}) is 10 cm^{-2} for the bare GaP while for the GaP/MoO_x sample it reaches 27 cm^{-2}. The increased J_{SC} can be explained by an improved charge separation introduced in the device after the deposition of the MoO_x. Considering the estimated CB edge of the MoO_x and VB of the GaP, this behaviour implies alternative charge transfer via mid-gap states as illustrated in Figure 37c, giving rise to increased minority carrier flow from the bulk towards the space charge region. However the increased series resistance in the samples containing the MoO_x cannot be explained by this. The presence of high series resistance can be attribute to the relatively low conductivity of the MoO_x layer as shown in Figure 37a. An interesting feature is that n-GaP/MoO_x device showed an improved fill factor (FF), but with decreased V_{OC} compared to those from the p-GaP/MoO_x. Based on band alignment with a negatively shifted Fermi level of the GaP, the n-GaP/MoO_x structure could potentially increase the V_{OC}. This unforeseen J-V response may be attributed to the high recombination at the interface between the GaP and the MoO_x, due to relatively high doping concentration of the n-GaP ($2 \cdot 10^{18} cm^{-3}$). The increased dark current (inset in Figure 37b) in the case of the n-type GaP also supports this.

Furthermore, as seen in Figure 37b (blue curve) the essential feature of the MoO_x addition on p-GaP is the concave response of the J-V curve of the solar cell. This is called an "inflection point" or "S-shaped anomaly" and the reasons for its appearance can be numerous. Battaglia et al. [89] researched MoO_x as a hole selective contact and encountered the same S-shaped behaviour, which was attributed to a band alignment issue between the layer interfaces. This could possibly be the result of either low work function of the MoO_x layer or the presence of a native oxide on the GaP surface. It has been reported that the latter can adversely affect the solar cell's FF. This misalignment results in holes extraction hindering, that deteriorates further with the increase of the MoO_x layer thickness. Kumar et al. [91] support that the appearance of the S-shape can be attributed mainly to interfacial states of the thin layers. As already described, oxygen vacancies are formed in the bulk during the MoO_x deposition, which serve as hole extraction paths. Such induced defects and trap states create energy barriers which lead to loss of V_{OC} and FF. Furthermore, it has been reported that post deposition annealing at high temperatures can remove the S-shape effect and drastically increase the efficiency of the device, since defects states are reduced and the interface is no longer characterized by poor charge carrier permeability [92]. Finally, a slight decrease of current density near the maximum power point can be attributed to shading effects. The non-illuminated part of the photoelectrode at the point where the contact is connected with the external circuit, creates a shading effect. Since the parallel conductivity of the amorphous formed MoO_x film is poor, the diffusion of charge carriers from the illuminated area towards the contact area is limited by the resistivity and consequently, limiting the current output [93]. In order to avoid the S-shaped J-V curve, it is therefore necessary for the MoO_x to be free of native oxides on its surface and have lower thickness in order to avoid band misalignment and to further decrease the series resistance. The Fermi level should however be higher, in order to improve band alignment, improve the holes extraction paths and the FF, although there should still be a barrier for electrons extraction. A lower thickness can also result in lower reverse saturation current due to thinner space charge region, while maintaining a higher transmittance [89].

The illustration shown in Figure 37c is not to scale. The band allignment between the different thin films is based on a simulated study performed by W. Yoon et. al. [94], where p-Si was used in contact with MoO_x as hole extraction layer. It was found that the band bending at the interface is greatly affected by the MoO_x electron affinity. The structure presented in Figure 37c for the n-GaP is indicative of the bend bending spikes. Regarding the p-GaP, depending on the exact value of the MoO_x electron affinity, the referred CB spike could have the opposite direction. In that case, it would still be favorable even for electrons to flow towards the HTL or further increase interface recombination [94].

4.2.2 GaP-based SRFB photocharging

Once the optimal device configuration is determined, based on the inferences from the MoO_x deposition conditions, the photoelectrochemical behaviour of the half-cell is analyzed. Multiple photoelectrode samples were prepared, employing different thin films and tested in contact with AQS as cathode (Appendix E). The variations aimed in increasing the device photocurrent output and available photovoltage for charging the electrolytes, compared with the same device without the MoO_x as HTL. These included testing n and p-type GaP, incorporating TiO_2 as prospective ETL material, with intentional formation of native and other oxides to circumvent recombination and integrating Pt as a conducting layer. Afterwards, the best performing configuration is used in the dual-chamber cell coupled with the electrolytes and separated by a Nafion membrane, for the chronoamperometry measurements. The redox reactions of the electrolytes employed are:

$$AQS + 2H^{+} + 2e^{-} \rightleftharpoons AQSH_2, E_{redox} = 0.11V_{NHE} \tag{44}$$

$$3HI \rightleftharpoons HI_3 + 2H^{+} + 2e^{-}, E_{redox} = 0.67V_{NHE} \tag{45}$$

So the overall cell reaction is:

$$AQS + 3HI \rightleftharpoons AQSH_2 + HI_3, E_{cell} = 0.56V_{NHE} \tag{46}$$

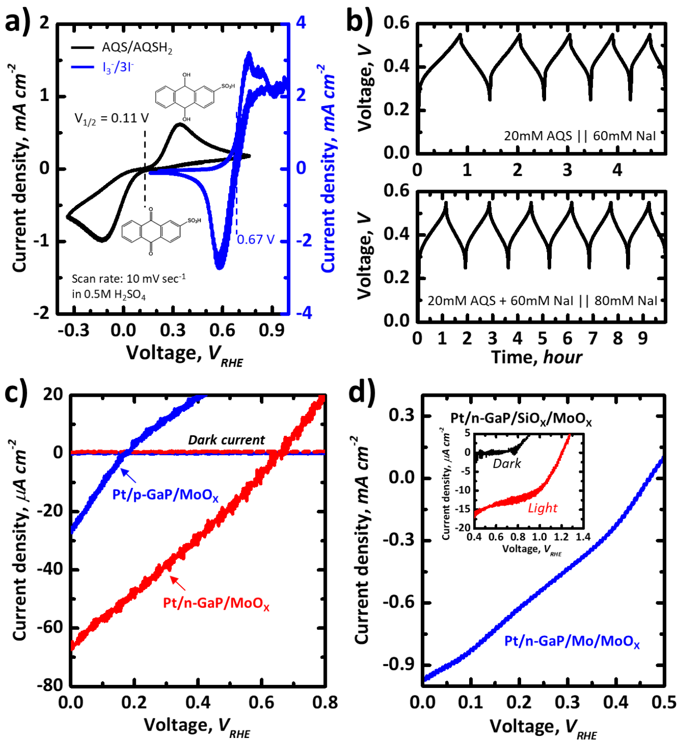

Figure 38: a) CV's of 20 mM solutions of AQS (black) and NaI (blue). For both 0.5M H_2SO_4 was used as a supporting electrolyte. b) RFB cycling with different electrolyte compositions in 0.5M H_2SO_4 supporting electrolyte. Incorporating 60mM NaI along with he 20mM AQS in the catholyte, results in lower battery capacity loss per cycle. c) Dark and illuminated LSV curves of n and p-type GaP, including Pt as a conducting layer and MoO_x as a HTL. d) Illuminated LSV curve of Pt/n-GaP/Mo/MoO_x electrode with the optimal performance. Inset shows the dark and illuminated LSV curves for the photoelectrode incorporating SiO_x (III).

The AQS (cathode) and NaI (anode) CV's can be seen in Figure 38a. These result is a cell voltage of 0.56 V. The RFB cycling behaviour is shown in Figure 38b, where 20mM AQS along with 60mM NaI was used a catholyte and 80mM NaI as anolyte. This was based on previous published data that resulted in a lower RFB capacity loss over the course of several cycles (Appendix E). In order to improve the photoelectrode properties, a Pt conducting layer was deposited at the interface with the electrolyte, since Pt has already been proven to be suitable as a conducting layer. The purpose of incorporating MoO_x as a HTL is to improve the charge carrier extraction and transport and therefore bubbling due to hydrogen production in a sealed SRFB is not of concern in the present chapter. After testing the photovoltaic cell J-V curve shown in Figure 37b, the results were corroborated by the LSV curves of the half-cell when the photoelectrode (with the same structure but also including Pt as conducting layer) is brought in contact with the cathode. Figure 38c depicts the LSV curves of Pt/GaP/MoO_x configuration for both n and p-type GaP. It can be seen that the photocurrent output is higher for the n-GaP, which can be interpreted based on better device electronic structure alignment (Figure 37c). Nevertheless, this device configuration did not yield the necessary current to achieve a meaningful result in the device charging process, but was examined as a guideline during the device optimization process. The best performing device corresponds to the LSV curve of Figure 38d, which is Pt/n-GaP/Mo/MoO_x, which showed high current output and suitable onset potential. The added thin metallic Mo layer contributed to the device as a protecting layer that also provided enough lateral conductivity in order to improve the charge transfer. As mentioned in Figure 37a, only the in plane conductivity was measured due to columnar growth of the MoO_x film. The metallic Mo layer therefore contributed to increasing the charge carrier lateral diffusion in the device, allowing for better properties. The inset of the plot presents the dark and illuminated measurements of the photoelectrode, incorporating a thin layer (2 nm) of high band gap SiO_x.

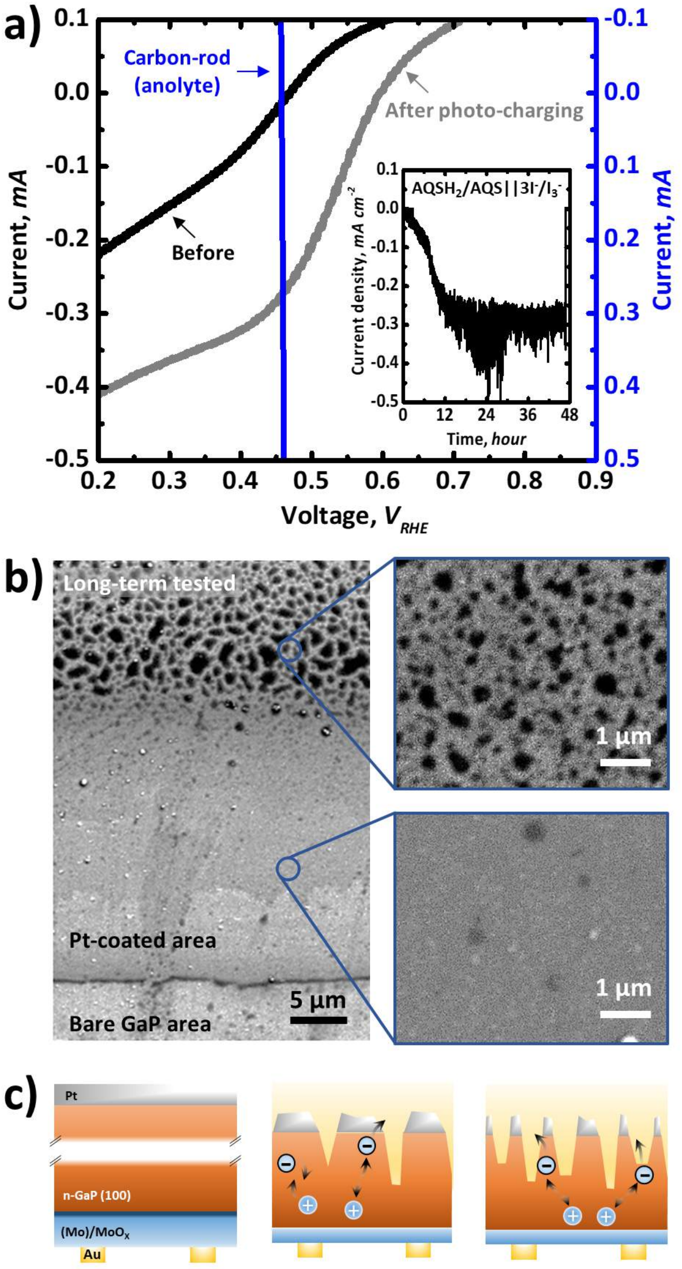

Figure 39: Overlaid current-voltage curves measured in a three-electrode experiment for the individual photocathode and anode (carbon felt). Pt/n-GaP/Mo/MoO_x in a 20mM AQS + 60mM NaI and 0.5 M H_2SO_4 supporting electrolyte; while carbon felt anode in a 80mM NaI with a 0.5 M H_2SO_4 supporting electrolyte. Inset depicts the chronoamperometry measurement in a dual-chamber cell for 48 consecutive hours and b) SEM images after the long-term CA measurement indicating the porous micro structures developed at the Pt protective layer. c) Cross sectional illustration of Pt protective layer and GaP absorber semiconductor electrochemical etching due to acidic electrolyte diffusion and increased available charge carrier pathwaysr (III).

Following the optimization of the MoO_x layer and the device band alignment, the best performing photoelectrode was employed in the dual-cell for the chronoamperometry measurement. Figure 39a shows the estimated current output of the device (black line) by overlapping the LSV curve of Figure 38d with the corresponding curve of the anolyte (NaI, blue line), using a carbon rod electrode. It can be clearly noted that not sufficient current is initially produced based on this overlap. The inset shows the chronoamperometry measurement for consecutive 48 h. The photocurrent output is initially equal to 20 $\mu A \cdot cm^{-2}$, which increases to 0.3 $mA \cdot cm^{-2}$ over 12 h. After that point, the average current output is around 0.3-0.5 $mA \cdot cm^{-2}$ and stays relatively constant. The reason a decrease in current is not observed after many charging hours, is that the photocurrent output is not sufficient to charge the cell to high SOC and the cell potential of the redox couple employed, based on the Nernst equation, has not exceeded the available photovoltage provided by the high GaP bandgap. The CA measurement showed very good photoelectrode performance, with an relatively high increase in current output, compared to reported results. It can be also noted in Appendix E how the formation of a MoO_x HTL combined with GaP specifically can result in a better performing electrode compared to that without MoO_x. In addition, incorporating TiO_2 as a widely studied ETL, to further improve the device performance, did not yield the expected results. The LSV curve of the photoelectrode, after the chronoamperometry measurement is concluded, is also shown in Figure 39a (grey curve). The new overlap with the anolyte half-cell now estimates a current output of about 0.3 mA, which is higher than both the initial LSV (before the photocharging commensed) and the case of the chronoamperometry measurement. Nevertheless, this overlap should only be used as an estimation of the actual current output, since it does not take into account resistance from the second electrolyte, the membrane and electrolyte kinetic overpotential losses and other losses due to more contact points and electrolyte evaporation during operation.

Regarding the Pt function on the device, its role is to provide better conductivity for the charge carriers diffusion, as well as acting as a protection layer, preserving the GaP wafer from corrosion. During the deposition process, a Pt protective layer (Figure 39b) was formed on the GaP, which enabled a higher active area for the redox reaction to take place. Due to diffusion, however, of highly acidic electrolyte (H_2SO_4) through the Pt islands, the GaP surface was subjected to electrochemical surface etching, forming porous micro structures as reported elsewhere [95]. This is also seen in Figure 39b through the SEM images of the Pt protective layer after the long-term CA measurement and previous SEM studies of the surface modification can be found in Appendix E. This surface roughening, caused by the electrochemical process in aqueous H_2SO_4 solution, is believed to have lead to the development of nano-sized pores on the GaP surface, which facilitate the charge carrier diffusion, as illustrated in Figure 39c. The same conclusion can be made with or without Pt conducting layer degradation during long residence time operation. This way the photocurrent output keeps increasing while the thin films get degraded at the same time. In addition, the same phenomenon could result into reduced charge carrier travel pathway distance and therefore better carrier separation, if the diffusion length is smaller than the formed islands distance. Regardless of the increase in current output, which is caused by the protective layer degradation and absorber semiconductor etching through diffusion of the electrolyte through pores, this issue is mainly attributed to stability problems of the conducting layer in acidic environment.

5. Discussion

The present chapter recapitulates the main findings of the research conducted and some important points are discussed in relation to the research objective. The photoelectrochemical performance of both Si and GaP developed SRFB's are evaluated and the research questions come into view. In addition, the results obtained from this project are thoroughly explained and compared with results from literature.

5.1 Charge carrier transport optimization at solid-electrolyte interface

In order to derive the device energy levels under equilibrium, the C/n^+p-Si back-side illuminated photocathode and the $Pt/Ti/pn^+-Si$ back-side illuminated photoanode are taken into account. The first was developed by replacing the Pt conducting layer with carbon with similar properties The equations described below are adjusted for the photocathode. The photoelectrode band diagrams are therefore examined. The band gap of p-type Si is 1.124 V. Starting from the $p-n^+$ junction, there will be an internal band bending regardless of electrolyte and other layer interactions. This is called built-in potential and can be calculated as [22, 96]:

$$V_{bi} = \frac{kT}{e} ln(\frac{N_{D,n^+}N_{A,p}}{n_i^2}) \tag{47}$$

Where $N_{D,n^+} = 5 \cdot 10^{19} cm^{-3}$ is the donor density of n^+-Si, $N_{A,p} = 3 \cdot 10^{15} cm^{-3}$ is the acceptor density of $p-Si$ and $n_i = 1.5 \cdot 10^{10} cm^{-3}$ is the intrinsic carrier density of Si. Respectively for the photocathode, the $N_{A,p^+} = 1 \cdot 10^{20} cm^{-3}$ is the acceptor density of p^+-Si, $N_{D,n} = 1.75 \cdot 10^{16} cm^{-3}$ is the donor density of $n-Si$. This results in a built-in voltage of 0.88 V. This developed voltage creates a band bending in each differently doped side of the junction. The total depletion width, which corresponds to the length at which the electric field distribution exists is calculated as:

$$W = \sqrt{\frac{2\epsilon_0\epsilon_{Si}(N_{D,n^+} + N_{A,p-Si})V_{bi}}{eN_{D,n-Si}N_{A,p-Si}}} \tag{48}$$

Where $\epsilon_0 = 8.85 \cdot 10^{12} Fm^{-1}$ is the permittivity in vacuum and $\epsilon_{Si} = 11.7$ is the relative permittivity of Silicon. The total space charge region can then be calculated to be 615 nm. This is distributed among the two differently doped regions of the p-n junction as:

$$x_{p-Si} = W\frac{N_{D,n^+}}{N_{A,p-Si} + N_{D,n^+}} \tag{49}$$

$$x_{n^+} = W\frac{N_{A,p-Si}}{N_{A,p-Si} + N_{D,n^+}} \tag{50}$$

The depletion region is therefore distributed almost entirely in the p-type Si. Furthermore, the metal layers are in contact with the p-type Si. This contact can either be an Ohmic contact or a Schottky barrier. If it is assumed that a Schottky barrier exists, which is likely the case, there will appear an upwards band bending with a barrier height described by:

$$\Phi_{Bi,Si} = \Phi_C - \Phi_{Si} + \frac{kT}{e} ln(\frac{N_{C,Si}}{N_{D,n^+}}) \tag{51}$$

Where Φ_C is the work function of carbon, which is also in contact with the electrolyte, under equilibrium. It is assumed that the metal conducting layer work function equilibrates with the redox potential of potassium ferricyanide, which is 0.475 V_{NHE} = 4.975 V_{vacuum}. $\Phi_{Si} = 4.15V$ is the electron affinity of Si.$N_{C,Si} = 2.8 \cdot 10^{15} cm^{-3}$ is the effective density of states. Respectively for the cathode $N_{V,Si} = 1.04 \cdot 10^{19} cm^{-3}$. The barrier height is therefore 0.58 V and distributed over a width of:

$$W = \sqrt{\frac{2\epsilon_0 \epsilon_{Si} \Phi_{Bi,Si}}{eN_{D,n^+}}} \tag{52}$$

Which is calculated to be 0.5 nm. The other electrode configurations of Figure 26 can then be calculated in the same way.

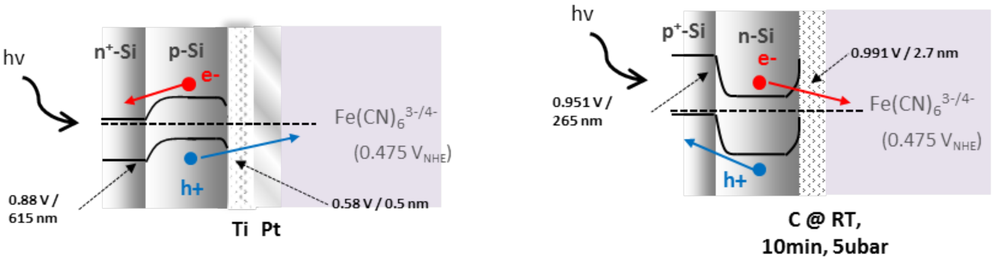

Figure 40: Band alignment of solid / electrolyte interface based on calculations for the a) back side illuminated photoanode $Pt/Ti/pn^+ - Si/Au$ and b) back side illuminated photocathode $C/np^+ - Si/Au$

As shown in Figure 40, the photoanode presents a lower built-in voltage, distributed over a bigger depletion width and the Schottky barrier formed in contact with the conducting layer is smaller and shorter. This allows higher probability of electron tunneling towards the electrolyte and can be the reason why the photoanode in question (Figures 31d, 40a) presents a lower resistance with a more steep current increase that reaches its saturation current density, while the photocathode has more sluggish kinetics (Figures 31b, 40b). In conclusion, the semiconductor-metal interface can be designed to boost the performance of redox flow batteries. Assuming a cheap and stable catalyst layer, such as carbon, unable to cause HER in a sealed battery, there are certain steps to be followed for its optimization in terms of charge transport. In case of an Ohmic contact, there will be no potential distribution across the device. However in most cases a Schottky barrier is developed on the semiconductor side which needs to be minimized, to also reduce the space charge region and enable electron tunnelling through the barrier. For this there is a need to develop a conducting layer with suitable thickness, transparent, with catalytic "islands" and high surface area. Specifically for carbon, porosity is also important and the formation of a more compact layer achieved higher current output. Another important consideration would be to achieve a catalyst layer that will provide an onset potential in dark conditions and equilibrium, similar to the redox reaction in question. This will enable all the available photovoltage upon illumination to be capitalized for the charging of the redox species.

5.2 Charge carrier transport optimization at semiconductor-semiconductor interface

In order to optimize the charge carrier transport at the interface of two materials, the energy diagram is very important to understand the energy level alignment and electronic structure of the layers. As mentioned before, MoO_x is an inherently n-type semiconductor, with oxygen vacancies formed during sputtering near its conduction band, that enables the extraction and collection of holes. The charge carriers are generated in the base semiconductor. In the case of GaP, both n and p-type were studied. This creates a n-n and a p-n heterojunction, respectively. Based on the calculated distance of the mid-gap states of MoO_x from the Fermi level, which is aligned under equilibrium, the optimal configuration can be described as shown in Figure 41a. The illustration shown in Figure 41a is not to scale. The band allignment between the different thin films is based on a simulated study performed by W. Yoon et. al. [94], where p-Si was used in contact with MoO_x as hole extraction layer. It was found that the band bending at the interface is greatly affected by the MoO_x electron affinity. The structure presented in Figure 41a for the n-GaP is indicative of the bend bending spikes. Regarding the p-GaP, depending on the exact value of the MoO_x electron affinity, the referred CB spike could have the opposite direction. In that case, it would still be favorable even for electrons to flow towards the HTL or further increase interface recombination [94].

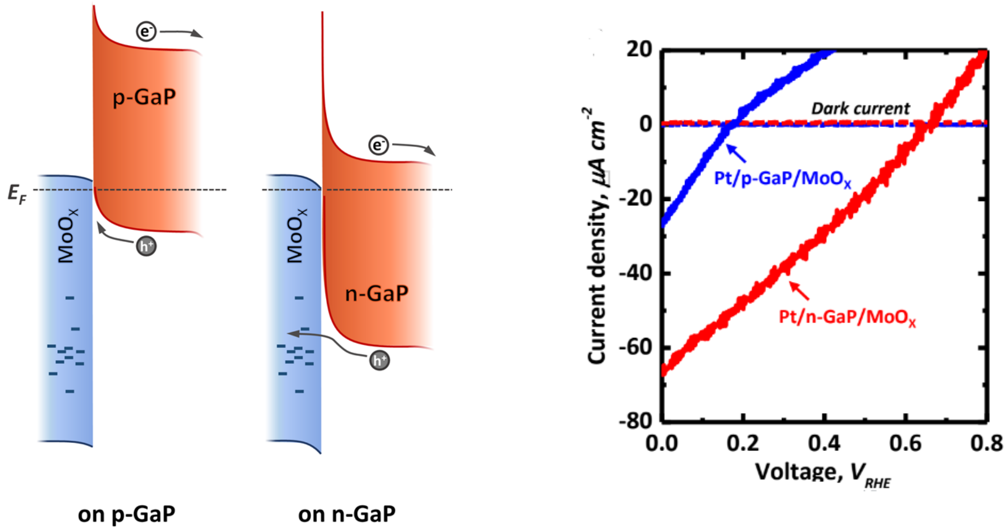

Figure 41: a) Schematic band alignment at an interface between the MoO_x and p- and n-GaP substrates and b) the resulting LSV in terms of onset potential and current output which can be significantly improved by device electronic structure examination (III).

This can be further supported by the LSV curves shown in Figure 41b, where it is clear that the charge separation is more efficient on the n-type GaP compared to the p-type. This is partially due to ion-beam cleaning of the sample to remove the carbon that contaminates the sample, as seen in Figure 35, which shifts the MoO_x mid-gap states closer to the VB. As mentioned before, the illustration of Figure 41a (p-GaP) is not based on actual data. It was found that low electron affinity values of MoO_x film, resulted in limitations regarding interface recombination [94]. The electron affinity needs to be increased, in order for a large CB spike to be formed to block the movement of electrons [94]. In general, a low interface state density and low junction recombination, along with a high enough electron affinity will result in improved charge carrier extraction. Regarding the Pt/n-GaP/Mo/MoO_x photoelectrode which resulted in the optimal performance, including a high increase in photocurrent output during the long-term CA measurement (as seen in Figure 39 inset), it is believed that this was the case due to improved lateral conductivity by incorporating a thin (2nm) Mo layer, as well as due to surface degradation of the Pt conducting layer. Regarding the thin Mo layer (2 nm), it is expected to be oxidized since the deposition of MoO_x follows directly after that. Nevertheless, a Mo rich phase is employed since it improves the lateral conductivity as a metal compound and prevents the formation of a native oxide (GaO_x) on the GaP surface. This is important since the GaO_x formation was proven to promote charge carrier recombination and therefore lower device efficiency (Appendix E). In conclusion many useful inferences can be derived from the analysis of the MoO_x electronic structure based on its formation parameters. These include the alignment of MoO_x with n-type GaP, formed under low oxygen concentration to improve both its conductivity (Figure 37) as well as its band alignment, surface cleaned before use and thinner film to avoid the concave shape of the J-V characteristics and therefore efficiency loss due to increased recombination. In addition, the use of a native oxide, such as GaO_x or SiO_2 did not improve the performance and current output of the device as expected, but aided the recombination processes at the trap states. The chronoamperometry showed high photocurrent output, better than previous reported results, however the dual-cell volume of 25mL does not allow for a high SOC to be achieved withing a reasonable time frame. The high photocurrent output during the CA measurement was achieved due to better spacial separation of the photogenerated charge carriers and the improved lateral conductivity attributed to the rich Mo phase, which also prevented the native oxide formation. The consequtive current increase is attributed to microstructural corrosion of the Pt conducting layer and the GaP semiconductor, which provided higher active area and improved charge carrier pathways, however presented stability issues in long-term operation.

5.3 Electrolyte selection parameters for optimal SRFB performance

As far as the electrolyte selection is concerned, there are multiple parameters to be considered for an efficiently designed SRFB. These include not only the redox potential of the electrolyte employed, but also the supporting electrolyte, pH conditions, operating volume, toxicity and price. The black and grey curves of Figure 55 depict the chronoamperometry measurements, employing the anodic photoelectrode ($Pt/Ti/pn^+ - Si/Au$), with a different electrolyte volume, 25 mL and 15 mL respectively. As can be seen, the current output of the device is greatly affected by the electrolyte level, which also affects the IEM coverage. The dual-cell used for the measurements is operated at 25 mL, a very big volume to achieve complete SOC. Nevertheless, in these cases the charging efficiency is 9.4% and 7.7%, respectively. These were cross examined also by comparing a potassium ferricyanide sample absorbance after the photocharging takes place and comparing it with standard solutions prepared beforehand, to approximate the achieved SOC (Appendix B). The current increase of the lower volume cell (grey curve of Figure 55) during the first operational hours can be attributed to a temperature increase that causes the internal resistance to decrease. The subsequent current decrease is attributed to rise in cell voltage as explained by the Nernst equation (Figure 30a for the specific cell case) . For these two cases of 25 mL and 15 mL employed, the corresponding achieved SOC is 9% and 63%, respectively. Another way to identify this is from the input charge as measured by the potentiostat.

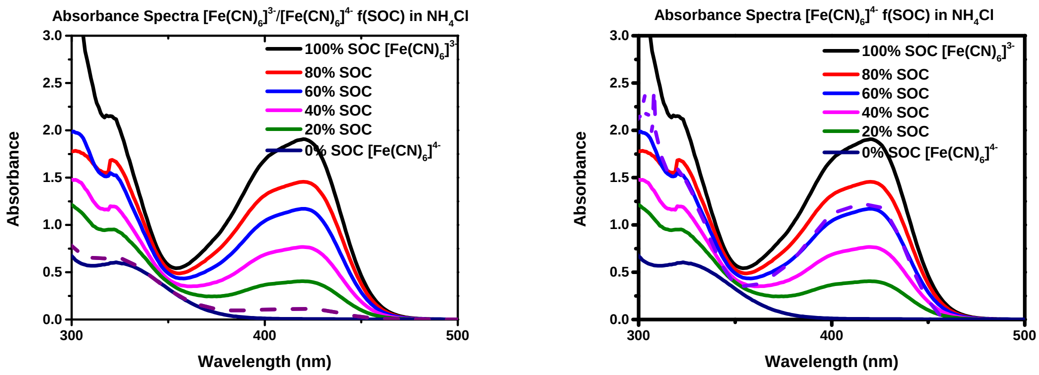

Figure 42: a) UV-Vis measurement of $Fe(CN)_6^{4-}$ after the photocharging of 25mL compartment to cross examine the achieved SOC with standard solutions and b) UV-Vis measurement of $Fe(CN)_6^{4-}$ after the photocharging of 15mL compartment to cross examine the achieved SOC with standard solutions.

The available pathways for ion exchange are therefore also a crucial parameter and incorporating a cell with lower IEM coverage can affect the resistance and therefore the current output. Figures 43a and b depict the SRFB configuration employed for the CA measurements of Figures 42a and 42b, respectively. The difference between the configurations is the volume employed, which also practically affects the photocurrent output, as shown above. The main points to consider when assembling the SRFB device, is the partly uncovered photoelectrode (W.E.) which does not enable the transport of charge carriers through all the available conducting islands formed on the surface, the partly submerged carbon rod (C.E. - R.E.), which provides lower surface area and the IEM which also complicates the ion diffusion process.

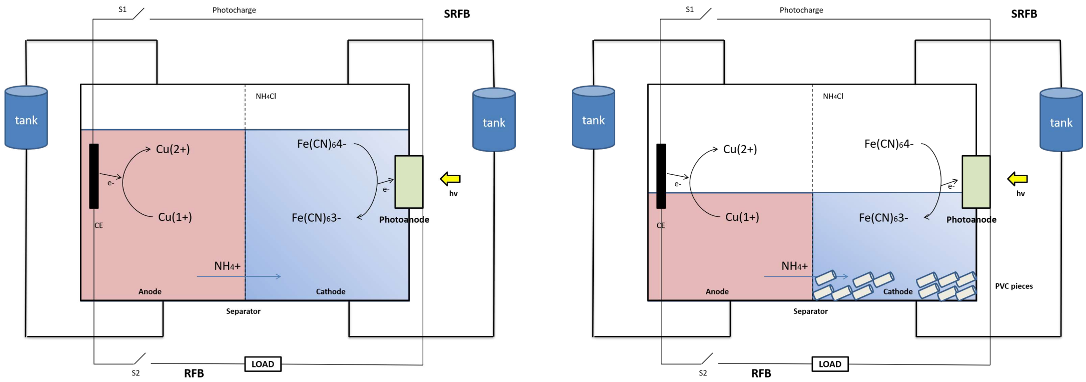

Figure 43: The SRFB device illustration with BPA and $CuSO_4/\ Fe(CN)_6^{4-}$ redox couple based on the CA measurement of Figures 42a and 42b with a) high volume and b) low volume, respectively.

In order to achieve a high round trip efficiency SRFB, the RFB optimization is a crucial step. Both in terms of operating pH (Appendix B), as well as in terms of redox potential. This is the first and foremost property regarding the electrolyte selection for proper energy levels matching when in contact with the photoelectrode.

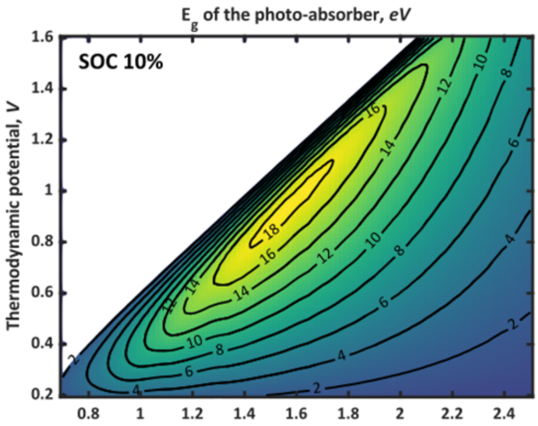

Figure 44: The theoretical estimation of achieved charging efficiency (at 10% SOC) based on the absorber semiconductor band gap and the redox couple employed (I).

Figure 44 illustrates the maximum achievable charging efficiency of the device, based on the semiconductor band gap and the electrolyte couple employed. The plot corresponds to low SOC, this efficiency however changes as the photocharging progresses. This is seen theoretically in Figure 30 and cross examined with Figure 55. The achieved SOC for the low volume cell is 63%, which based on the Nernst equation the cell voltage has almost reached the maximum of 0.5 V photovoltage supplied by the electrode under illumination and can explain the current decrease. By examining Figure 44, it is clear that the cell potential for the $CuSO_4/\ Fe(CN)_6^{4-}$ cell (E_{cell} = 0.4 V) can already yield a higher charging efficiency compared to the $TEMPO - sulfate/\ Fe(CN)_6^{3-}$ cell (E_{cell} = 0.34 V). Apart from the more favorable electronic structure of the $Pt/Ti/pn^+ - Si/Au$ photoanode compared to the $C/np^+ - Si/Au$ photocathode (Chapter 5.1), the cell potential also plays a crucial role in the higher output charging efficiency of the $CuSO_4/\ Fe(CN)_6^{4-}$ cell.

5.4 SRFB structure considerations for efficient operation

As shown in Figure 45, the solar conversion efficiencies at 10% SOC are 2.10% and 9.44% for the unbiased ferricyanide | | TEMPO-sulfate and Cu-sulfate | | ferrocyanide photocharging cases, respectively. This photoelectrochemical charging efficiency for the Cu-sulfate | | ferrocyanide cell is the highest among all the SRFBs with a single photon-device, so far reported. Naturally, the ferricyanide | | Br2/Br- combination case only showed 0.32% at 1% SOC due to discrepancy between the photovoltage and cell voltage to drive the chemical reaction. Comparison of the experimentally measured results and theoretical estimation provided here, reveals that the experimental results follow the predicted trend, and the overlap may serve as a guideline to the actual kinetic overpotential of each device. The discrepancy between the theoretical maximum at given cell potential indicates that there remains substantial room for improvement in terms of better redox couples matching, RFB conditions optimization, minimizing the overall device resistance and improved charge carrier transport. The dual-chamber cell employed for the experimental measurements is characterized by the large volume (25 mL) that must be employed in each compartment, which is expected to lead to higher cell resistance compared to a more compact cell. In the overall device design-wise approach, an important limitation to circumvent is the series resistance of the device. As illustrated in Figure 45b, similarly to the kinetic overpotential effect, obtainable maximum STC% increases with decreasing series resistance, simultaneously shifting optimum cell potential to higher values. As predicted by the theoretical model in Figure 45c, the c-Si sample without optical loss (i.e., 0% reflection) shows a STC%

higher than 11%, while the sample with bare Si surface exhibits around 8.7% with practical PV parameters (reflection of 30%, $R_s = 5\Omega cm$). Optimization of surface incorporating anti-reflective coating can be performed, however the discrepancy between these two extreme conditions is insignificant compared to the effect of device resistance. Considering the device configuration, reducing the overpotential is the key for increasing the operating current density and efficiency. Unlike the photoanode sample with facile carrier transport across the Pt/p-Si junction (Figure 40a), the photocathode with n-type Si surface requires more than 200mV with respect to onset potential. Replacing the Ti interlayer with another metal with lower work function, e.g., Mn (4.1 V) or forming a heavily doped sheet conducting layer (n+ in this case) can reduce the Schottky barrier. While, in the case of the photoanode, a different approach is required since the $Pt/pn^+ - Si$ photoanode sample showed fast kinetics (less than 100 mV is required). An additional charge transport layer, such as highly doped n-type TCO, including the indium tin oxide (ITO), can be considered as an interlayer between the n^+-doped Si surface and metallic grid (Cu/Au in this case) that enhances the lateral conductivity.

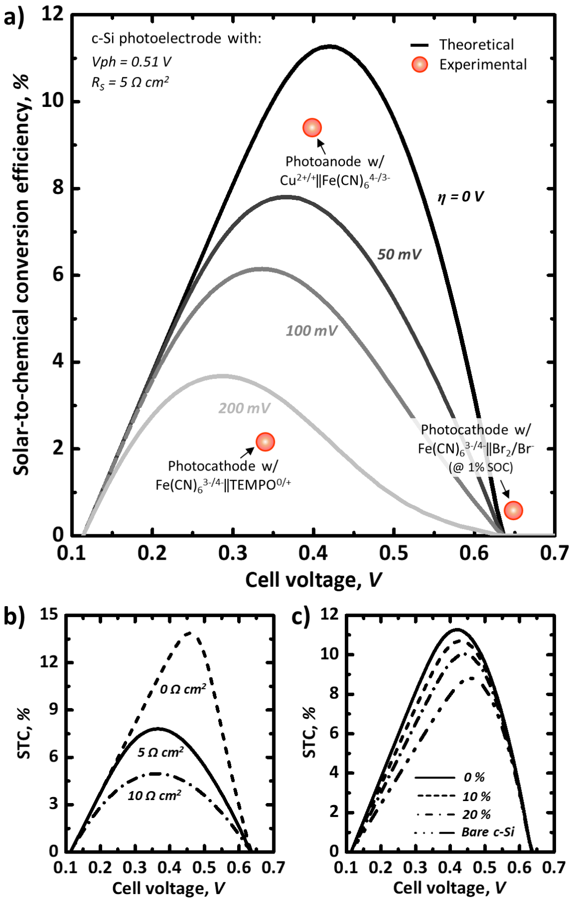

Figure 45: [The photo-charging efficiency at 10% SOC is plotted as a function of the thermodynamic potential for different kinetic overpotentials (= 0 V, 0.15 V, 0.3 V and 0.45 V). The system is modeled as a c-Si photoelectrode with a photovoltage (V_{ph}) of 0.51 V, a series resistance of 5 Ωcm^2 and surface reflection from the bare Si surface. Note that the model does not take into account the effect of solution resistance. The red circles indicate the experimentally measured value with various redox couples from the Figure 31. b) and c) correspond to the model curves for different series resistance and reflection from the surface, respectively (II).

6. Conclusions

The present thesis project set out to provide some detailed guidelines on the charge carrier transport mechanisms entailed at the photoelectrode interlayer interfaces. These include research on suitable materials based on energy levels matching and control of thin films physical and electronic structure by varying the formation conditions. The deposition parameters of the thin films are optimized to yield the best device performance and their contribution, in terms of charge carrier exchange, is examined. Once the appropriate device is developed, it is subjected to a series of characterization experiments and consequently incorporated in the Solar Redox Flow Battery (SRFB) system, for the photo-charging of the selected redox species.

For the progress and evaluation of the conducting layer at the semiconductor/electrolyte interface, the following points were addressed:

- A carbon conducting thin film was developed, with similar kinetics to platinum, that significantly improved the charge carrier transport through the growth of well distributed islands, that provided a higher active area. The optimization of the formation conditions and energy levels matching with the electrolyte, led to minimizing the kinetic overpotential and Schottky barrier at the interface.

- An extensive research into redox species properties and characterization was performed to result in a functional couple with suitable cell potential, based on the available photovoltage provided by the designed photoelectrodes.

- A Si-based SRFB, with copper-iron redox species was developed, that yielded a solar to chemical efficiency of 9.4%, the highest charging efficiency among all the SRFBs with a single photon-device so far reported.

The importance of the Si-based SRFB progress can be emphasized in two aspects. First, the necessity of band alignment design in order to form a facile carrier pathway from both n- and p-type photoelectrodes to the electrolyte with the respective redox reaction in the SRFB system is emphasized along with supporting experimental evidence. The high solar-to-chemical conversion performance of 9.4% can be achieved using a Si-based photoanode from the system with a cell voltage of 0.4 V. Although it should be stressed that this addresses only "half" of the SRFB problem (i.e., photo-charging performance), this is the highest reported efficiency for the SRFB with a single photo-device system. The device performance was also investigated and it was found that it is highly influenced by the morphology of the conducting layer, which determines the coverage of substrate. Minimizing the deactivated surface is another key feature for the facile carrier transfer. The comparison between the measured value and modeled curves identifies that there is still room to improve the conversion efficiency, and in overall device-wise approach, various efforts, including the optical loss management and RFB optimization should be carried out for further development. Important limitations to circumvent are the strong reflection from the Si surface, which was inevitable for all samples tested, as well as the electrolyte degradation towards solid precipitates. In the aspect of redox system level, increase of solution conductivity is an obvious solution for better kinetics. Either using a highly concentrated electrolyte or conductive additives can be some simple approaches.

For the comprehension and development of the hole transport layer (HTL) based on the device electronic structure, the subsequent inferences are presented:

- The formation conditions of a MoO_x thin film as hole transport layer were studied and the control of its electronic structure and inherent properties was comprehended, in order to energetically align with GaP.
- Incorporating the hole transport layer resulted in better spatial separation of the photogenerated charge carriers, circumventing recombination, which contributed to the net current of the device.
- The incorporation of the designed photoelectrode in an SRFB with a suitable redox couple was successful and led to improved performance. MoO_x can be therefore successfully integrated with n-GaP to promote the extraction of the photo-generated holes.

Incorporating carefully designed thin films, to promote the better spatial separation of photogenerated charge carriers, is a simple and functional way to increase the overall device performance. Regarding the n-GaP based SRFB, MoO_x can be successfully incorporated on the thin film structure as a hole extraction layer. The device showed improved performance, it was however unstable due to electrolyte diffusion though the conducting layer islands' and the GaP surface was subjected to electrochemical surface etching, forming porous micro structures. This issue needs to be addressed in terms of better protective/conductive layer coverage to increase the available active area and electrolyte conditions optimization.

Bibliography

[1] Y. Nakato, K. Ueda, H. Yano, H. Tsubomura, "Effect of Microscopic Discontinuity of Metal Overlayers on the Photovoltages in Metal-Coated Semiconductor-Liquid Junction Photoelectrochemical Cells for Efficient Solar Energy Conversion," *J. Phys. Chem.*, vol. 92, pp. 316–2324, 1988.

[2] M. D. Adams, J. H. Kyle, "Precipitation of Cyanide as Cu2Fe(CN)6 Compounds from Cyanidation and Detoxification Circuits," *Conference: Minprex 2000, Melbourne, Australia*, pp. 201–206, 2000.

[3] H. Konishi, T. Bitoh, H. Ono, T. Oishi, K. Koyama, M. Tanaka, "Behavior of Copper Dissolution in an Ammonia Solution Containing Ammonium Chloride or Sulfate," *Journal of JSEM*, vol. 14, pp. s205–s209, 2014.

[4] G. Seyfang, A. Smith, "Grassroots Innovations for Sustainable Development: Towards a New Research and Policy Agenda," *Environmental Politics*, vol. 16, no. 4, p. 584–603, 2007.

[5] "Paris Agreement." [Online]. Available: https://unfccc.int/sites/default/files/english_paris_agreement.pdf

[6] "United nations, department of economic and social affairs, world population projections." [Online]. Available: https://www.un.org/development/desa/en/news/population/world-population-prospects-2017.html

[7] "International energy agency (iea), world energy outlook, 2018." [Online]. Available: https://webstore.iea.org/download/summary/190?fileName=English-WEO-2018-ES.pdf

[8] "U.s. energy information administration, international energy outlook, 2017." [Online]. Available: https://www.eia.gov/outlooks/ieo/pdf/0484(2017).pdf

[9] "International energy agency (iea), co_2 emissions from fuel combustion, 2017." [Online]. Available: https://www.iea.org/publications/freepublications/publication/CO2EmissionsfromFuelCombustionHighlights2017.pdf

[10] "International energy agency (iea), renewables market analysis and forecast from 2018 to 2023, 2018." [Online]. Available: https://www.iea.org/renewables2018/

[11] "Renewable Sources of Energy." [Online]. Available: https://renewablesourcesofenergy1.weebly.com/

[12] I. Kougias, S. Szabo, "Pumped hydroelectric storage utilization assessment: Forerunner of renewable energy integration or Trojan horse?" *Energy*, vol. 140, pp. 318–329, 2017.

[13] J. Rugolo, M. J. Aziz, "Electricity storage for intermittent renewable sources," *Energy Environmental Science*, vol. 5, p. 7151–7160, 2012.

[14] M. G. Walter, E. L. Warren, J. R. McKone, S. W. Boettcher, Q. Mi, E. A. Santori, N. S. Lewis, "Solar Water Splitting Cells," *Chem. Rev.*, vol. 110, p. 6446–6473, 2010.

[15] P. Wang, S. Wang, H. Wang, Z. Wu, L. Wang, "Recent Progress on Photo-Electrocatalytic Reduction of Carbon Dioxide," *Part. Part. Syst. Charact.*, vol. 35, no. 1700371, 2018.

[16] D. Gust, T. A. Moore, A. L. Moore, "Solar Fuels via Artificial Photosynthesis," *Accounts of Chemical Research*, vol. 42, no. 12, pp. 1890–1898, 2009.

[17] R. J. Cogdell, T. H. P. Brotosudarmo, A. T. Gardiner, P. M. Sanchez, L. Cronin, "Artificial photosynthesis - Solar fuels: Current status and future prospects," *Biofuels*, vol. 1, no. 6, p. 861–876, 2010.

[18] K. Wedege, D. Bae, W. A. Smith, A. Mendes, A. Bentien, "Solar Redox Flow Batteries with Organic Redox Couples in Aqueous Electrolytes: A Minireview," *J. Phys. Chem. C*, vol. 122, p. 25729–25740, 2018.

[19] K. A. Kavadias, D. Apostolou, J. K. Kaldellis, "Modelling and optimisation of a hydrogen-based energy storage system in an autonomous electrical network," *Applied Energy*, vol. 227, pp. 574–586, 2018.

[20] N. S. Lewis, "Research opportunities to advance solar energy utilization," *Science*, vol. 351, no. 6271, p. 25729–25740, 2016.

[21] Y. Zhao, Y. Ding, Y. Li, L. Peng, H. R. Byon, J. B. Goodenough, G. Yu, "A chemistry and material perspective on lithium redox flow batteries towards high-density electrical energy storage," *Chem. Soc. Rev.*, vol. 44, no. 22, p. 7921–8378, 2015.

[22] K. Wedege, D. Bae, E. Drazevic, A. Mendes, P. C. K. Vesborg, A. Bentien, "Unbiased, complete solar charging of a neutral flow battery by a single Si photocathode," *RSC Adv.*, vol. 8, p. 6331–6340, 2018.

[23] G. Hodes, J. Manassen, D. Cahen, "Photoelectrochemical energy conversion and storage using polycrystalline chalcogenide electrodes," *Nature*, vol. 261, p. 403–404, 1976.

[24] W. Li, H.-C. Fu, L. Li, M. Cabán-Acevedo, J.-H. He, S. Jin, "Integrated Photoelectrochemical Solar Energy Conversion and Organic Redox Flow Battery Devices," *Angew. Chemie Int. Ed.*, vol. 55, p. 13104–13108, 2016.

[25] Q. Cheng, W. Fan, Y. He, P. Ma, S. Vanka, S. Fan, Z. Mi, D. Wang, "Photorechargeable High Voltage Redox Battery Enabled by Ta3N5 and GaN/Si Dual-Photoelectrode," *Adv.Mater.*, vol. 29, p. 1700312, 2017.

[26] F. Urbain, S. Murcia-López, N. Nembhard, J. Vázquez-Galván, C. Flox, V. Smirnov, K. Welter, T. Andreu, F. Finger, J. R. J. R. Morante, "Solar vanadium redox-flow battery powered by thin-film silicon photovoltaics for efficient photoelectrochemical energy storage," *J. Phys. D. Appl. Phys.*, vol. 52, no. 044001, 2019.

[27] S. Liao, X. Zong, B. Seger, T. Pedersen, T. Yao, C. Ding, J. Shi, J. Chen, C. Li, "Integrating a dual-silicon photoelectrochemical cell into a redox flow battery for unassisted photocharging," *Nature Communications*, vol. 7, p. 11474, 2016.

[28] J. R. McKone, F. J. DiSalvo, H. D. Abruña, "Solar energy conversion, storage, and release using an integrated solar-driven redox flow battery," *J. Mater. Chem. A*, vol. 5, p. 5362–5372, 2017.

[29] M. Park, J. Ryu, W. Wang, J. Cho, "Material design and engineering of next-generation flow-battery technologies," *Nat. Rev. Mater.*, vol. 2, p. 1–18, 2016.

[30] K. Wedege, J. Azevedo, A. Khataee, A. Bentien, A. Mendes, "Direct Solar Charging of an Organic–Inorganic, Stable, and Aqueous Alkaline Redox Flow Battery with a Hematite Photoanode," *Angew.Chem.Int.Ed*, vol. 5, p. 7142–7147, 2016.

[31] W. Li, H.-C. Fu, Y. Zhao, Jr-H. He, S. Jin, "14.1% Efficient Monolithically Integrated Solar Flow Battery," *Chem*, vol. 4, p. 1–14, 2018.

[32] I. M. Peters, S. Sofia, J. Mailoa, T. Buonassisi, "Techno-economic analysis of tandem photovoltaic systems," *RSC Adv.*, vol. 6, p. 66911–66923, 2016.

[33] Z. J. Yu, J. V. Carpenter, Z. C. Holman, "Techno-economic viability of silicon-based tandem photovoltaic modules in the United States," *Nat. Energy*, vol. 3, p. 747–753, 2018.

[34] B. Keita, L. Nadjo, "Layer-type semiconductor-based storage cell with I/I3 and 9,10-anthraquinone-2,6-disulfonate/9,10-anthrahydroquinone-2,6-disulfonate redox couples," *J. Electroanal. Chem.*, vol. 151, p. 283–288, 1983.

[35] ——, "Electrochemistry and photoelectrochemistry of sodium 9,10-anthraquinone-2,6-disulfonate in aqueous media. Application to rechargeable solar cells and to the synthesis of hydrogen peroxide," *J. Electroanal. Chem.*, vol. 163, p. 171–188, 1984.

[36] Y. Zhou, S. Zhang, Y. Ding, L. Zhang, C. Zhang, X. Zhang, Y. Zhao, G. Yu, "Efficient Solar Energy Harvesting and Storage through a Robust Photocatalyst Driving Reversible Redox Reactions," *Adv. Mater.*, vol. 30, p. 1–7, 2018.

[37] W. D. McCulloch, M. Yu, Y. Wu, "pH-Tuning a Solar Redox Flow Battery for Integrated Energy Conversion and Storage," *ACS Energy Lett.*, vol. 1, p. 578–582, 2016.

[38] P. G. P. Ang, A. F. Sammells, "Photoelectrochemical systems with energy storage," *Faraday Discuss. Chem. Soc.*, vol. 70, p. 207–222, 1980.

[39] M. F. Weber, M. J. Dignam, "Efficiency of Splitting Water with Semiconducting Photoelectrodes," *J. Electrochem. Soc.*, vol. 131, pp. 1258–1265, 1984.

[40] B. Seger, O. Hansen, P. C. K. Vesborg, "A Flexible Web-Based Approach to Modeling Tandem Photocatalytic Devices," *Sol. RRL*, vol. 1, no. e2016000135, 2017.

[41] J. D. Benck, L. C. Seitz, B. A. Pinaud, T. F. Jaramillo, A. J. Forman, Z. Chen, "Modeling practical performance limits of photoelectrochemical water splitting based on the current state of materials research," *ChemSusChem*, vol. 7, p. 1372–1385, 2014.

[42] H. Döscher, J. F. Geisz, T. G. Deutsch, J. A. Turner, "Sunlight absorption in water – efficiency and design implications for photoelectrochemical devices," *Energy Environ. Sci.*, vol. 7, p. 2951–2956, 2014.

[43] "International energy agency (iea), a fundamental look at supply side energy reserves for the planet, 2015." [Online]. Available: https://www.iea-shc.org/data/sites/1/publications/2015-11-A-Fundamental-Look-at-Supply-Side-Energy-Reserves-for-the-Planet.pdf

[44] A. S. R. S. M. Z. O. Isabella, K. Jager, *Solar Energy: The Physics and Engineering of Photovoltaic Conversion, Technologies and Systems*. UIT Cambidge, England, 2016.

[45] S. C. Bhatia, “Advanced renewable energy systems, Part 1,” *Woodhead Publishing India Pvt. Ltd.*, 2014.

[46] D. A. Neamen, *Semiconductor Physics and Devices - Basic Principles (4th ed.)*. McGraw-Hill, 2012.

[47] H. D. G. P. H. B. H. R. Purchase, H. De Vriend, *Artificial photosynthesis for the conversion of sunlight to fuel*, 2015.

[48] L. Cao, M. Skyllas-Kazacos, D.-W. Wang, “Solar Redox Flow Batteries: Mechanism, Design, and Measurement,” *Adv. Sustainable Syst.*, vol. 2, no. 1800031, 2018.

[49] R. Memming, *Semiconductor Electrochemistry*. Wiley-VCH Verlag GmbH Co. KGaA, 2015.

[50] N. Elgrishi , K. J. Rountree, B. D. McCarthy, E. S. Rountree, T. T. Eisenhart, J. L. Dempsey, “A Practical Beginner’s Guide to Cyclic Voltammetry,” *J. Chem. Educ*, vol. 95, no. 2, pp. 197–206, 2018.

[51] “Cyclic Voltammetry.” [Online]. Available: https://chem.libretexts.org/Bookshelves/Analytical_Chemistry/Supplemental_Modules_(Analytical_Chemistry)/Instrumental_Analysis/Cyclic_Voltammetry

[52] Weber, A.Z., Mench, M.M., Meyers, J.P. et al., “Redox flow batteries: a review,” *J Appl Electrochem*, vol. 41, p. 1137, 2011.

[53] B. Seger, I. E. Castelli, P. C. K. Vesborg, K. W. Jacobsen, O. Hansenc, I. Chorkendorf, “2-Photon tandem device for water splitting: comparing photocathode first versus photoanode first designs,” *Energy Environ. Sc*, vol. 7, pp. 2397–2413, 2014.

[54] Y. Saito, S. Uchida, T. Kubo, H. Segawa, “Energy-Storable Dye-Sensitized Solar Cells with Tungsten Oxide Charge-Storage Electrode,” *ECS Trans.*, vol. 16, pp. 27–34, 2009.

[55] N. F. Yan, G. R. Li, G. L. Pan, X. P. Gao, “TiN Nanotube Arrays as Electrocatalytic Electrode for Solar Storable Rechargeable Battery,” *J. Electrochem. Soc.*, vol. 159, pp. 1770–1774, 2012.

[56] P. Liu, Y. L. Cao, G. R. Li, X. P. Gao, X. P. Ai, H. X. Yang, “A Solar Rechargeable Flow Battery Based on Photoregeneration of Two Soluble Redox Couples,” *ChemSusChem*, vol. 6, p. 802 – 806, 2013.

[57] N. F. Yan, G. R. Lia, X. P. Gao, “Solar rechargeable redox flow battery based on Li2WO4/LiI couples in dual-phase electrolytes,” *J. Mater. Chem. A*, vol. 1, pp. 7012–7015, 2013.

[58] N. F. Yan, G. R. Li, X. P. Gao, “Electroactive Organic Compounds as Anode-Active Materials for Solar Rechargeable Redox Flow Battery in Dual-Phase Electrolytes,” *J. Electrochem. Soc.*, vol. 161, pp. 736–741, 2014.

[59] M. Yu, X. Ren, L. Ma, Y. Wu, “Integrating a redox-coupled dye-sensitized photoelectrode into a lithium-oxygen battery for photoassisted charging,” *Nat Commun*, vol. 5, pp. 5111–5117, 2014.

[60] D. Liu, Z. Wei, C. J. Hsu, Y. Shen, F. Liu, "Efficient Solar Energy Storage Using A TiO 2/WO 3 Tandem Photoelectrode in An All-vanadium Photoelectrochemical Cell," *Electrochimica Acta*, vol. 136, pp. 435–441, 2014.

[61] C. Hsu, Y. Shen, Z. Wei, D. Liu, F. Liu, "Anatase TiO 2 nanobelts with plasmonic Au decoration exhibiting efficient charge separation and enhanced activity," *Journal of Alloys and Compounds*, vol. 613, pp. 117–121, 2014.

[62] N. Li, Y. Wang, D. Tang, H. Zhou, "Integrating a Photocatalyst into a Hybrid Lithium-Sulfur Battery for Direct Storage of Solar Energy," *Angew.Chem.Int.Ed.*, vol. 54, p. 9271–9274, 2015.

[63] "IV Curve." [Online]. Available: https://www.pveducation.org/pvcdrom/solar-cell-operation/iv-curve

[64] "Introduction to IV Curves." [Online]. Available: https://cran.r-project.org/web/packages/ddiv/vignettes/IVcurve.html

[65] "Diode Equation." [Online]. Available: https://www.pveducation.org/ru/%D1%84%D0%BE%D1%82%D0%BE%D1%8D%D0%BB%D0%B5%D0%BA%D1%82%D1%80%D0%B8%D1%87%D0%B5%D1%81%D0%BA%D0%B8%D0%B5/diode-equation

[66] S. Hu, N. S. Lewis, J. W. Ager, J. Yang, J. R. McKone, N. C. Strandwitz, "Thin-Film Materials for the Protection of Semiconducting Photoelectrodes in Solar-Fuel Generators," *J. Phys. Chem. C*, vol. 119, p. 2420124228, 2015.

[67] L. R. F. A. J. Bard, *Electrochemical Methods: Fundamentals and Applications*. John Wiley Sons, New York, 2000.

[68] L. Tous, "Nickel/Copper Plated Contacts as an Alternative to Silver Screen Printing for the Front Side Metallization of Industrial high Effciency Silicon Solar Cells," *(PhD thesis)*.

[69] "Etch rates for silicon, silicon nitride, and silicon dioxide in varying concentrations and temperatures of KOH." [Online]. Available: https://cleanroom.byu.edu/KOH

[70] J. Winsberg, C. Stolze, S. Muench, F. Liedl, M. D. Hager, U. S. Schubert, "TEMPO/Phenazine Combi-Molecule: A Redox Active Material for Symmetric Aqueous Redox Flow Batteries," *American Chemical Societ*, vol. 8, p. 6331–6340, 2016.

[71] P. J. Kelly, R. D. Arnell, "Magnetron sputtering: a review of recent developments and applications," *Vacuum*, vol. 56, pp. 159–172, 2000.

[72] "High performance selective solar control glass, Tectonica-online." [Online]. Available: http://www.tectonica-online.com/productos/2707/snx_solar_selectivo_vidrio_extra_sunguard_selective/

[73] G. M. Alonzo-Medina, A. G. González, J. L. Sacedón, A. I. Oliva, "Understanding the thermal annealing process on metallic thin films," *Materials Science and Engineering*, vol. 45, p. 012013, 2013.

[74] "Ultraviolet - Visible Spectroscopy (UV) , Royal Society of Chemistry." [Online]. Available: http://www.rsc.org/learn-chemistry/content/filerepository/CMP/00/001/304/UV-Vis_Student%20resource%20pack_ENGLISH.pdf

[75] "Study of semiconductors by UV-Vis spectroscopy, Belarusian State University, Department of Energy Physics." [Online]. Available: http://www.physics.bsu.by/sites/default/files/files/departments/Energy/TEMPUS/CMM_lab/Characterization%20of%20modern%20materials%20-%20Study%20of%20semiconductors%20by%20UV-Vis%20spectroscopy%20-%20TEMPUS%20%28english%20version%29.pdf

[76] N. E. Widjonarko, "Introduction to Advanced X-ray Diffraction Techniques for Polymeric Thin Films," *Coatings*, vol. 6, p. 54, 2016.

[77] J. F. Moulder, *Handbook of X-ray Photoelectron Spectroscopy: A Reference Book of Standard Spectra for Identification and Interpretation of XPS Data*. Perkin-Elmer Corporation, 1992.

[78] "A Beginners Guide to XPS, Teignmouth Science and Technology Centre, 2017." [Online]. Available: http://www.casaxps.com/help_manual/manual_updates/Basics_Quantification_of_XPS_Spectra.pdf

[79] "R. Brennan, D. Dickey, Determination of Diffusion Characteristics Using Two- and Four-Point Probe Measurements, Solecon Laboratories, Inc., San Jose, California." [Online]. Available: http://www.solecon.com/pdf/determination_of_diffusion_characteristics_using_2_and_4pp.pdf

[80] Y. Singh, "Electrical Resistivity Measurements: a Review," *International Journal of Modern Physics: Conference Series*, vol. 22, p. 745–756, 2013.

[81] R. N. Jagtap, A. H. Ambre, "Atomic force microscopy (AFM): Basics and its important applications for polymer characterization: An overview," *Indian Journal of Engineering Materials Sciences*, vol. 13, pp. 368–384, 2006.

[82] "Nafion 115 Specifications." [Online]. Available: https://www.fuelcellstore.com/nafion-115

[83] K. Gelderman, L. Lee, S. W. Donne, "Flat-Band Potential of a Semiconductor: Using the Mott–Schottky Equation," *J. Chem. Educ*, vol. 84, no. 4, p. 685, 2007.

[84] G. Hodes, "Photoelectrochemical Cell Measurements: Getting the Basics Right," *J. Chem. Chem. Lett.*, vol. 3, no. 9, pp. 1208–1213, 2012.

[85] D. Bae, B. Seger, O. Hansen, P. C. K. Vesborg, I. Chorkendorff, "Durability Testing of Photoelectrochemical Hydrogen Production under Day/Night Light Cycled Conditions," *Chem. Electro. Chem*, vol. 6, pp. 106–109, 2019.

[86] D. Bae, B. Seger, P. C. K. Vesborg, O. Hansenb, I. Chorkendorff, "Strategies for stable water splitting via protected photoelectrodes," *Chem Soc Rev*, vol. 46, pp. 1933–1954, 2017.

[87] J. H. Thomas, "Effect of pressure on dc planar magnetron sputtering of platinum," *Journal of Vacuum Science Technology*, vol. 21, p. 572, 2003.

[88] "Moss–Burstein effect." [Online]. Available: https://en.wikipedia.org/wiki/Moss%E2%80%93Burstein_effect

[89] C. Battaglia, X. Yin, M. Zheng, I. D. Sharp, T. Chen, S. McDonnell, A. Azcatl, C. Carraro, B. Ma, R. Maboudian, R. M. Wallace, A. Javey, "Hole Selective MoOx Contact for Silicon Solar Cells," *Nano Lett.*, vol. 14, no. 2, pp. 967–971, 2014.

[90] M. Sook Oh, B. Seob Yang, J. Ho Lee, S. Ha Oh, U. Soo Lee, Y. Jang Kim, H. Joon Kim and M. Soo Huh, "Improvement of electrical and optical properties of molybdenum oxide thin films by ultralow pressure sputtering method," *Journal of Vacuum Science Technology A*, vol. 30, p. 031501, 2012.

[91] A. Kumar, S. Sista, Y. Yang, "Dipole induced anomalous S-shape I-V curves in polymer solar cells," *Journal of Applied Physics*, vol. 094512, 2009.

[92] F. A. de Castro, J. Heier, F. Nuesch, R. Hany, "Origin of the Kink in Current-Density Versus Voltage Curves and Efficiency Enhancement of Polymer-C60 Heterojunction Solar Cells," *IEEE JOURNAL OF SELECTED TOPICS IN QUANTUM ELECTRONICS*, vol. 16, no. 6, pp. 1690–1699, 2010.

[93] "Guide to interpreting i-v curve measurements of pv arrays, application note, 2011." [Online]. Available: http://resources.solmetric.com/get/Guide%20to%20Interpreting%20I-V%20Curves.pdf

[94] W. Yoon, J. E. Moore, E. Cho, D. Scheiman, N. A. Kotulak, E. Cleveland, Y. W. Ok, P. P. Jenkins, A. Rohatgi, R. J. Walters, "Hole-selective Molybdenum Oxide as a Full-area Rear Contact to Crystalline p-type Si Solar Cells," *Japanese Journal of Applied Physics*, vol. 56, p. 08MB18, 2017.

[95] M. Treideris, I. Simkiene, A. Selskis, Z. Balevicius, G.J. Babonas, "Electrochemical Formation and Microstructure of Porous Gallium Phosphide," *Acta Physica Polonica A*, vol. 119, pp. 131–134, 2011.

[96] D. Bae, B. Mei, R. Frydendal, T. Pedersen, B. Seger, O. Hansen, P. C. K. Vesborg, I. Chorkendorff, "Back-Illuminated Si-Based Photoanode with Nickel Cobalt Oxide Catalytic Protection Layer," *ChemElectroChem*, vol. 3, p. 546–1552, 2016.

Appendix A: Supporting information on conducting layers

Figure 46 depicts the electrochemical characterization under dark conditions of the carbon conducting layers formed at different deposition conditions. It can be noticed that the lower the thickness the lower the current output of the device. In addition, post-deposition annealing at 400 °C does not improve enough the charge transfer at the interface. Furthermore, it was found that using a lower pressure of 5μbar, instead of 10μbar, leads to a more compact and less porous film, that results in properties similar to those of Pt (or paired Pt/TiO_2). The measurements in Figures 25 and 46 correspond to 0% SOC of the potassium ferricyanide employed electrolyte.

Thermal voltage is equal to kT=0.026 eV, at temperature T=300K.

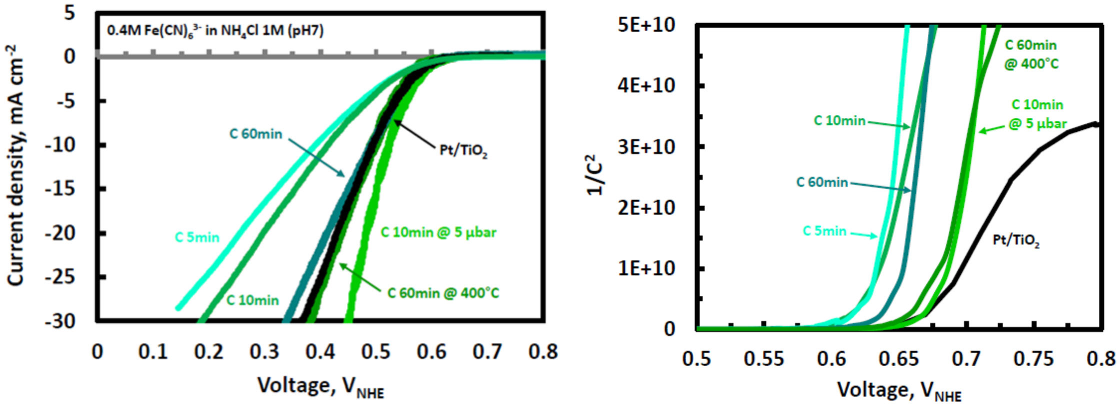

Figure 46: All dark a) CV and b) MS measurements for different Carbon, as conducting layer, deposition conditions.

Table 3 shows the experimentally obtained flat band potential values of different materials used as protective layers.

Material	$\mathbf{E}_{fb} + (\mathbf{k}_B T/q)$	E_{fb}
Bare Si	-0.24	-0.266
TiO2/Si	-0.12	-0.146
C(5min)/Si	0.612	0.586
C(10min)/Si	0.627	0.601
C(10min-5ubar)/Si	0.68	0.654
C(30min)/Si	0.657	0.631
C(60min)/Si	0.668	0.642
C(60min-400C)/Si	0.67	0.644
Pt(70sec)/Si	0.67	0.644
Pt(70sec)/TiO2/Si	0.67	0.644
C(10min)/TiO2/Si	-0.21	-0.236
C(10min-400C)/TiO2/Si	0.075	0.049
C(H2-400C)/Si	0.418	0.392
C(H2-400C)/TiO2/Si	0.23	0.204

Table 3: The calculated flatband potentials for various prospective materials deposited on highly-doped c-Si

Figure 47 depicts all the experiments performed in dark conditions for all the above mentioned protective layers. The best performing carbon layer is compared to that of Pt and their onset potential under different electrolytes SOC conditions are shown in Figure 48. The LSV experiments for 0%, 50%, and 100% SOC were carried out using the samples with Pt and carbon layer deposited on degenerately doped n^+-Si substrate. For making the 0% and 100% SOC electrolytes, 0.4M $K_3[Fe(CN)_6]$ and $K_4[Fe(CN)_6] \cdot 3H_2O$ were mixed with 1M NH_4Cl supporting electrolyte. The 50% SOC electrolyte is a mixed electrolyte with 0.2M $K_3[Fe(CN)_6]$ and 0.2M $K_4[Fe(CN)_6] \cdot 3H_2O$.

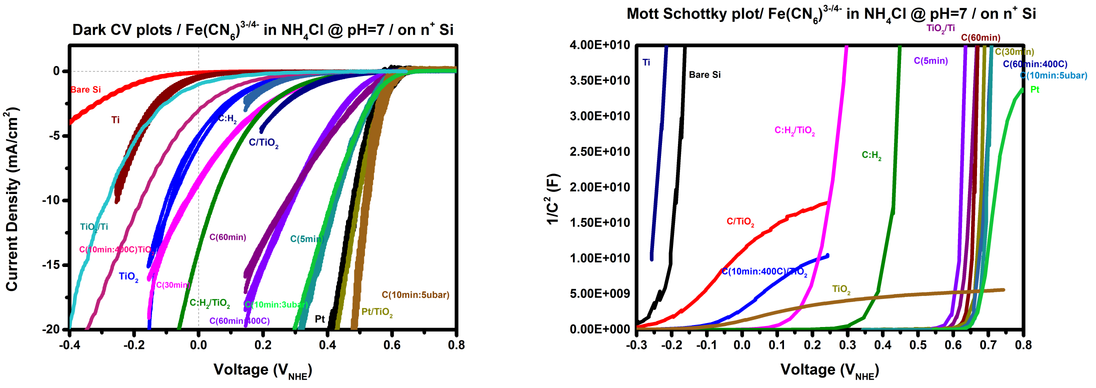

Figure 47: All dark a) CV and b) MS measurements for different electrode configurations and conducting layers employed.

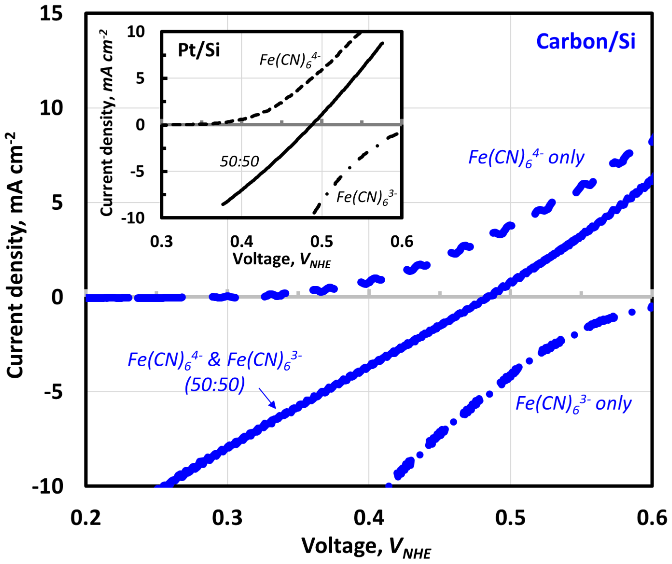

Figure 48: Dark measurements of Pt and C conducting layer at 0%, 50% and 100% electrolyte SOC.

Figure 49a depicts a semiconductor material, coated with metal islands and in contact with an electrolyte. As soon as the electrode is submerged in the electrolyte, following the electric double layer formation and as a response to that, there is a band bending of the energy levels of the semiconductor parts that are not coated with metal islands. A space charge region is therefore formed with different properties than that of the space charge region of the coated semiconductor surface. Since the semiconductor is considered a dielectric (can be polarized when an electric field is applied) while both the metal islands and the electrolyte are conductors with a theoretically constant electrical potential, the electric field distribution runs through the semiconductor. The charge of the metal is therefore counter acted by an opposite charge developed in the space charge region. This is shown in Figure 49b in terms of energy band diagram.

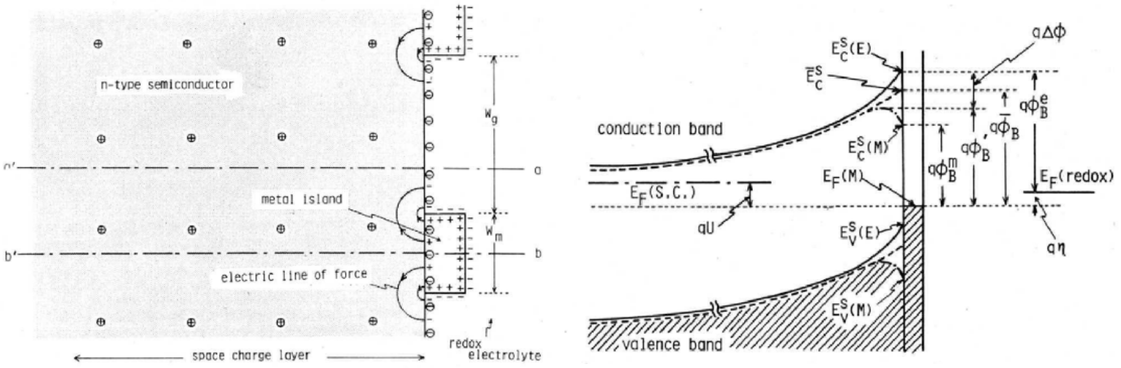

Figure 49: a) Schematic of electric field distribution of the semiconductor, coated with metal islands, in contact with electrolyte solution [1] and b) Schematic of the corresponding energy band diagram of the same semiconductor, coated with metal islands, in contact with electrolyte solution [1].

Appendix B: Supporting information on electrolytes

The SRFB structure incorporating the photoanode ($Pt/Ti/pn^{+} - Si$) and copper sulfate - potassium ferrocyanide proved to be the most efficient device, yielding a charging efficiency higher than 9%. The formattion of solid copper however restricts the practical use of such an SRFB. For this reason, it is important to to optimize the RFB operation, which is outside the scope of this project. For this, Konishi et. al. [3] and Adams [2] have published reports regarding the copper sulfate cells and how these can be adjusted based on the Cu Pourbaix diagram in order to form the desired product. Applying related research to the RFB operating conditions can ultimately result in a high solar-to-output-electricity SRFB.

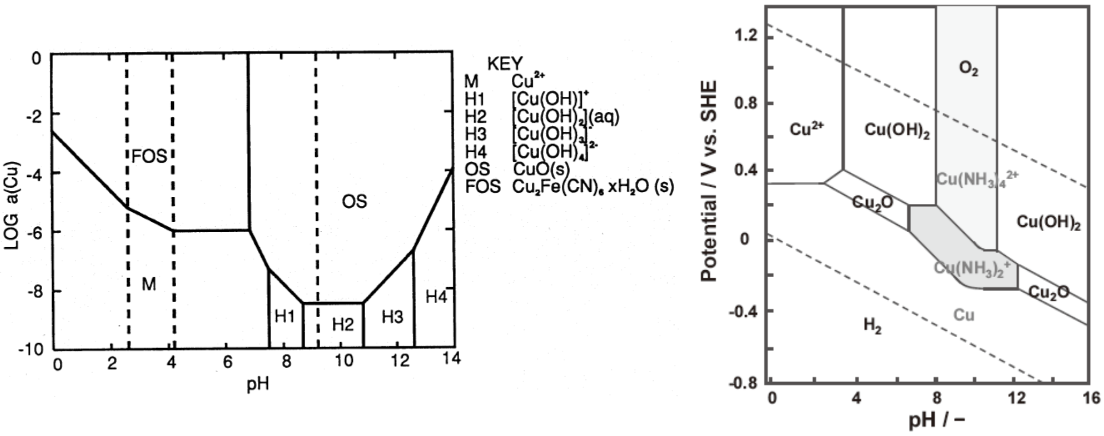

Figure 50: a) The stability of the copper (stable in pH region of 4-6.5. Above it it is unstable with respect to copper oxide (OS), and below it dissolves into its constituent ions. [2] and b) potential-pH diagram of copper-ammonia solution at 298K and 0.5 copper activity [3]

The CV's of all employed electrolyte couples in the developed SRFB's are shown bellow:

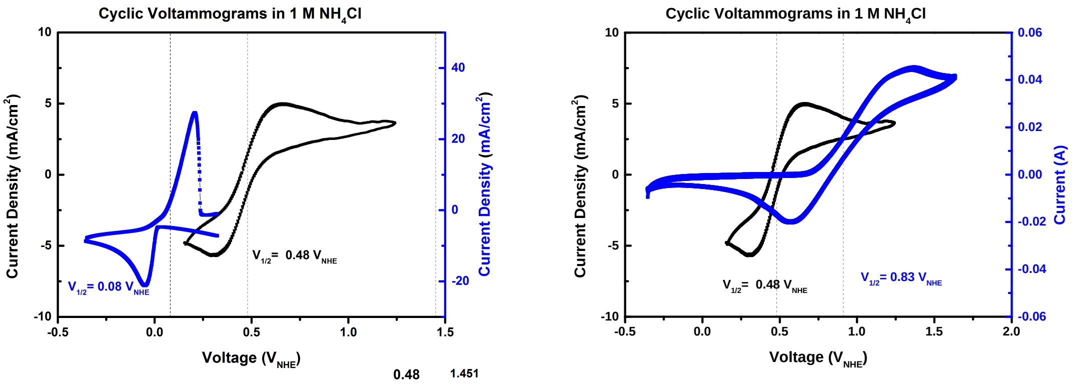

Figure 51: CV's of a) $CuSO_4$ and b) TEMPO-sulfate with respect to Potassium ferri/ferrocyanide.

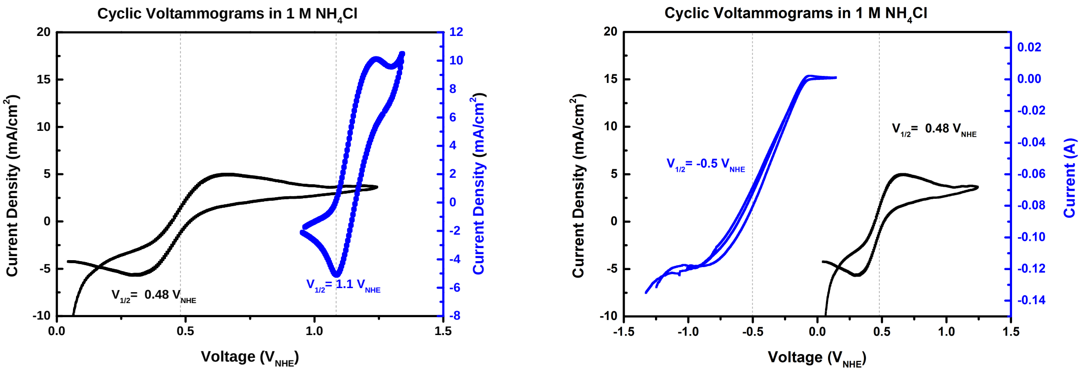

Figure 52: CV's of a) NH_4Br and b) $SnCl_4$ with respect to Potassium ferri/ferrocyanide.

Regarding the SOC measurement after each SRFB chronoamperometry test, due to practical considerations it was not possible to measure the cell voltage change while measuring the current. The reason for this was that no bias should be applied during illumination (to achieve complete unbiased photocharging) and therefore only the photocurrent output was measured. Consequently, the SOC achieved was measured by comparing the absorbance of potassium ferricyanide after the testing to that of standard solutions. In order to create the standard solutions it is important to acquire both reduced and oxidized forms of the electrolyte in questions. Such was the case for ferri/ferrocyanide which was produced by mixing 15 μL of standard solution with 2985 μL of NH_4Cl in a 3 mL cuvette. The standard solution were produced by mixing of proper quantities of each ferrous form in 50 mL NH_4Cl:

SOC	$K_3Fe(CN)_6$	$K_4Fe(CN)_6 \cdot 3H_2O$
0%	0.4M / 6.5848g	0M / 0g
20%	0.32M / 5.2678g	0.08M / 1.6896g
40%	0.24M / 3.9509g	0.16M / 3.3791g
60%	0.16M / 2.6339g	0.24M / 5.0687g
80%	0.08M / 1.3169g	0.32M / 6.7582g
100%	0M / 0g	0.4M / 8.4478g

Table 4: The quantities of oxidized and reduced form of potassium ferricyanide employed to produce the standard solutions for the UV-Vis measurements.

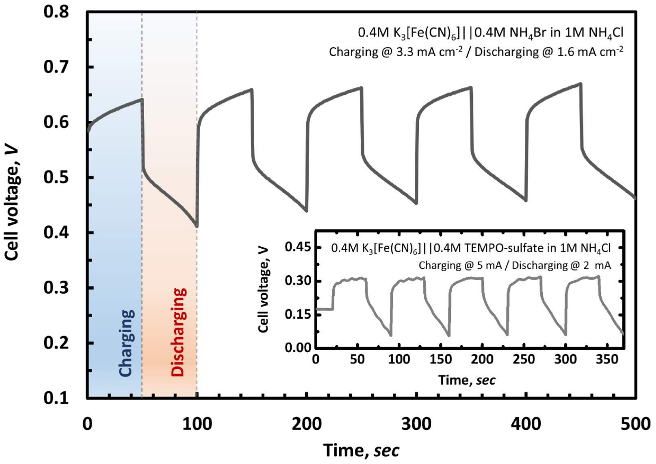

Figure 53: Charge/discharge curves in a 25 cm2 RFB cell with a constant current density of 3.3 mA/cm^2 and electrolyte concentration 0.4M ferrocyanide and 1M NH4Br in 1M NH4Cl. The inset shows a charge/discharge curves of the same catholyte using a pair of carbon-rods, but with a different anolyte (TEMPO-sulfate) at charging/discharging rate of 5 mA and 2 mA, respectively.

Appendix C: Supporting information on MoO_x HTL electronic structures

Figure 54 shows the procedure with which the band structures of various films are estimated. The different formation conditions are compared and their impact on the semiconductor VB and mid-gap states related to the Fermi level are comprehended. Figure 54a shows the temperature and oxygen partial pressure effect. For the same oxygen partial pressure, formation under high temperature results in a shift of the VB towards negative values and the same occurs with the mid-gap states shift. Increasing the oxygen partial pressure leads, again, to a shift of the VB towards negative values, the mid-gap states however shift towards the opposite direction. Figure 54b shows the effect of surface etching, which results in a shift of the VB towards positive values and the mid-gap states shift closer to the VB.

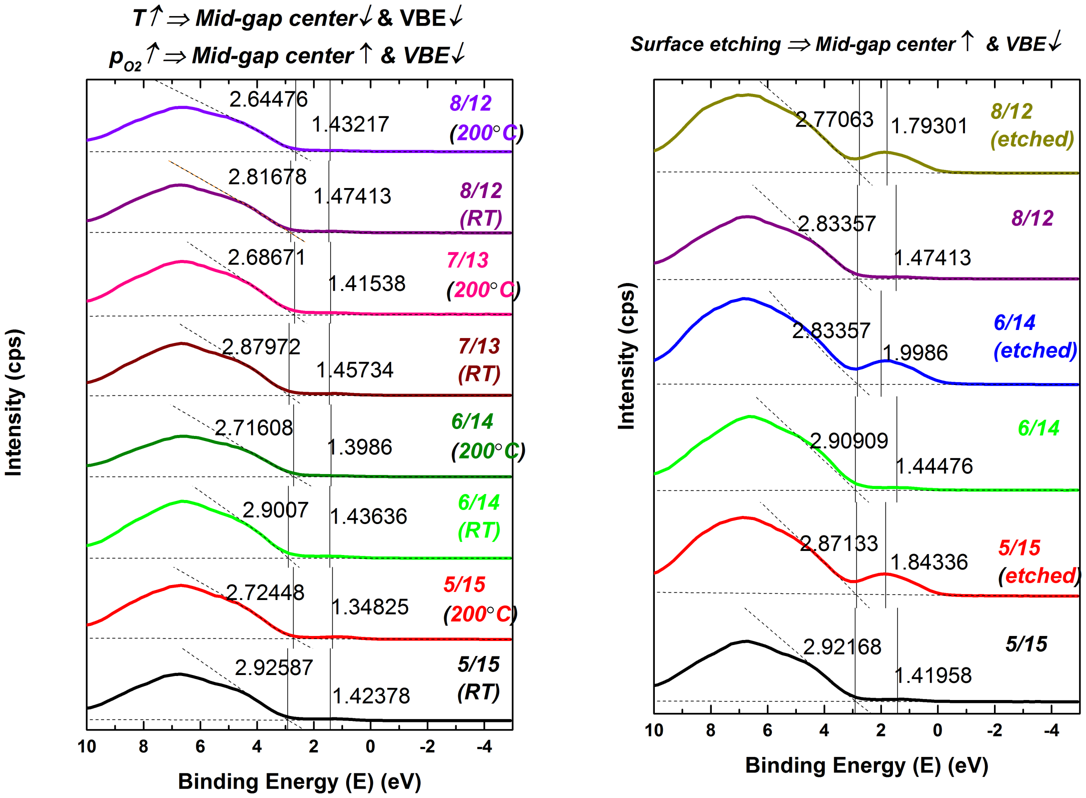

Figure 54: Influence of deposition conditions a) p_{O2} and T and b) surface cleaning of MoO_x on the valence band edge shift and the distance of the oxygen-vacancies induced mid-gap states from the Fermi level.

Appendix D: Supporting information on all Si-based SRFB's developed

The redox reactions of the NH_4Br and $SnCl_4$ SRFBs employed are:

$$Fe(CN)_6^{3-} + e^- \rightleftharpoons Fe(CN)_6^{4-} \tag{53}$$

$$Br^- + e^- \rightleftharpoons Br \tag{54}$$

So the overall cell reaction is:

$$Fe(CN)_6^{3-} + Br^- \rightleftharpoons Fe(CN)_6^{4-} + Br \tag{55}$$

$$Fe(CN)_6^{4-} \rightleftharpoons Fe(CN)_6^{3-} + e^- \tag{56}$$

$$Sn^{4+} + 2e^- \rightleftharpoons Sn^{2+} \tag{57}$$

So the overall cell reaction is:

$$2Fe(CN)_6^{4-} + Sn^{4+} \rightleftharpoons Fe(CN)_6^{3-} + Sn^{2+} \tag{58}$$

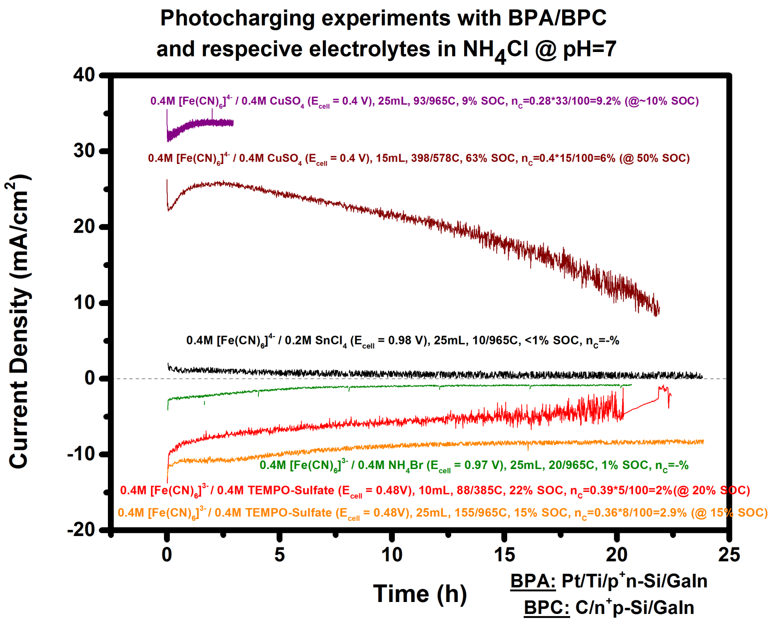

Figure 55: All chronoamperometry measurments employing various Si-based SRFB configurations.

Copper (II) sulfate ($CuSO_4$) / Potassium ferrocyanide ($K_4[Fe(CN)_6] \cdot 3H_2O$) SRFB w/ photoanode $Pt/Ti/pn^+ - Si/Au$, long (20h) photocharging measurement:

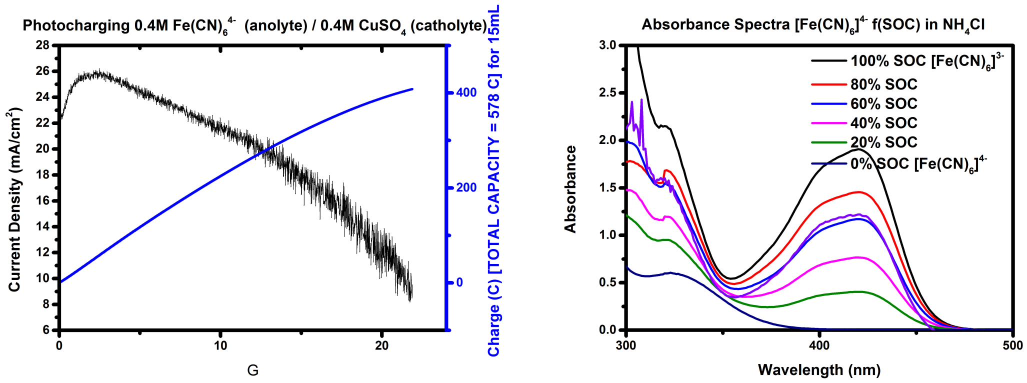

Figure 56: a) Chronoamperometry measurement for $CuSO_4/K_4[Fe(CN)_6] \cdot 3H_2O$ SRFB and b) measured achieved SOC after the photocharging.

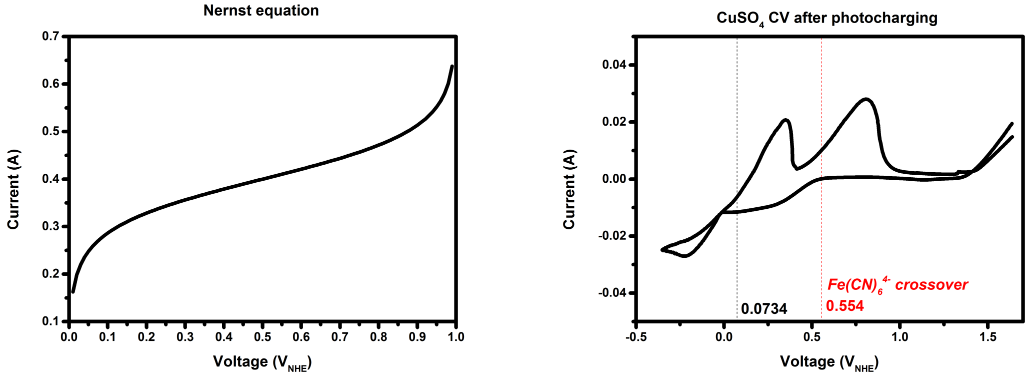

Figure 57: a) Theoretical cell voltage based on Nernst equation and b) CV measurement of the charged $CuSO_4$ after 20h of photocharging. Crossover of ferrous ions is visible.

TEMPO-sulfate / Potassium ferricyanide ($K_3[Fe(CN)_6]$) SRFB w/ photocathode $C/np^+ - Si/Au$ at high (25mL) electrolyte volume:

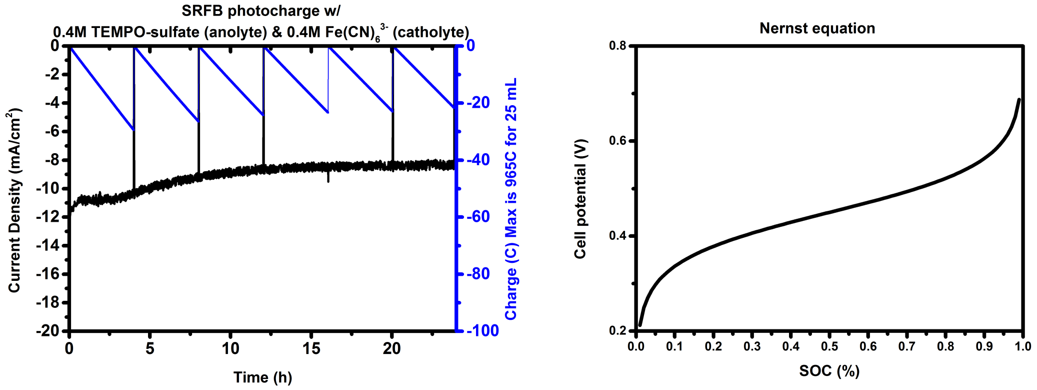

Figure 58: a) Chronoamperometry measurement for TEMPO-sulfate/$K_3[Fe(CN)_6]$ SRFB and b) theoretical cell voltage based on Nernst equation.

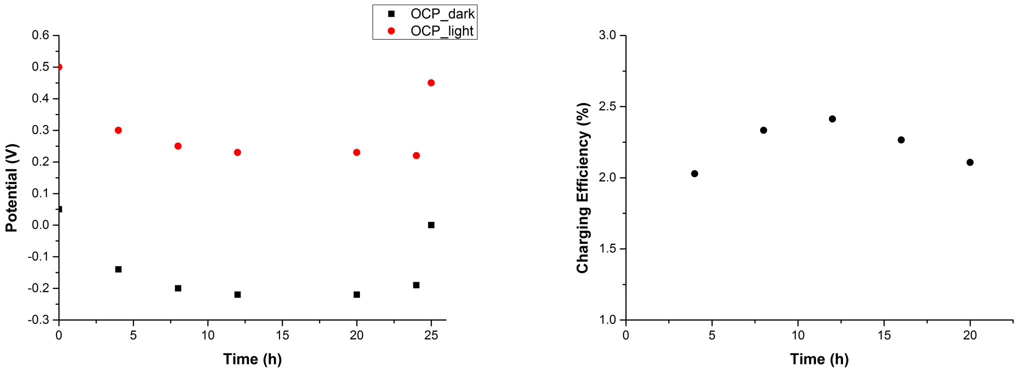

Figure 59: a) The measured Open Circuit Potential in dark and illuminated conditions of the dual-cell (TEMPO-sulfate/ferricyanide) during photocharging and b) the estimated charging efficiency measured during photocharging.

TEMPO-sulfate / Potassium ferricyanide ($K_3[Fe(CN)_6]$) SRFB w/ photocathode $C/np^+ - Si/Au$ at low (15mL) electrolyte volume:

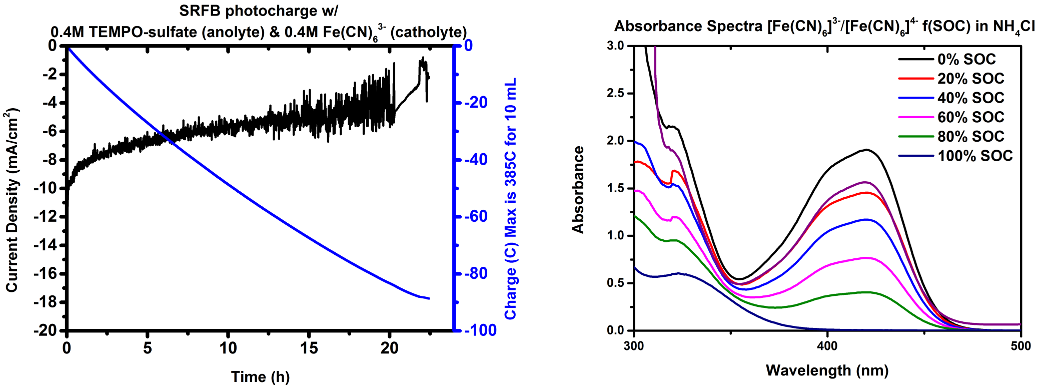

Figure 60: a) Chronoamperometry measurement for TEMPO-sulfate/$K_3[Fe(CN)_6]$ SRFB and b) measured achieved SOC after the photocharging.

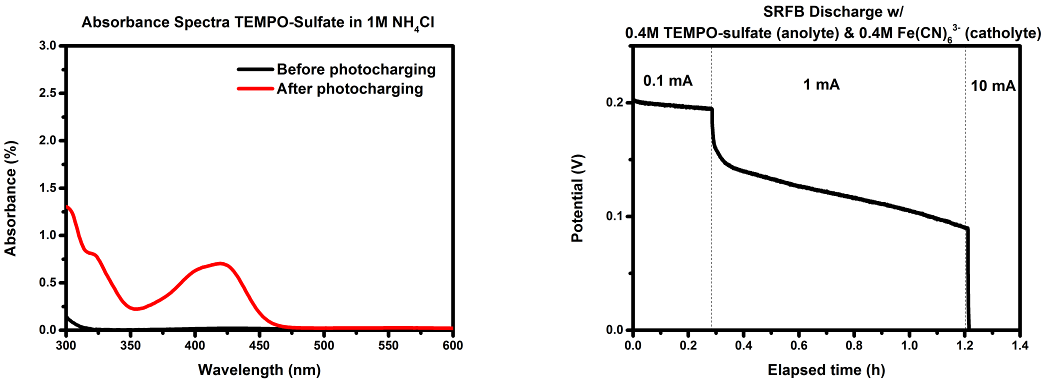

Figure 61: a) TEMPO-sulfate absorbance before and after the photocharging measurement and b) discharge curves with various currents of the photocharged cell.

Ammonium bromide (NH_4Br) / Potassium ferricyanide ($K_3[Fe(CN)_6]$) SRFB w/ photocathode $C/np^+ - Si/Au$:

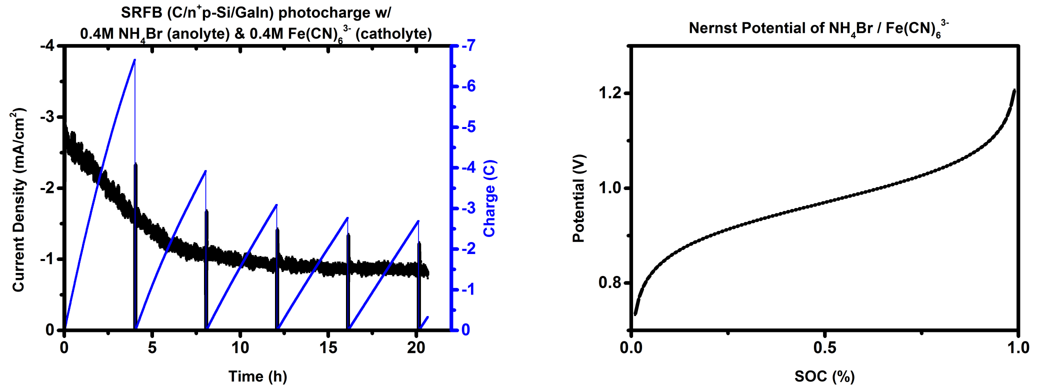

Figure 62: a) Chronoamperometry measurement for $NH_4Br/K_3[Fe(CN)_6]$ SRFB and b) theoretical cell voltage based on Nernst equation.

Tin (IV) chloride ($SnCl_4$) / Potassium ferrocyanide ($K_4[Fe(CN)_6] \cdot 3H_2O$) SRFB w/ photoanode $Pt/Ti/pn^+ - Si/Au$:

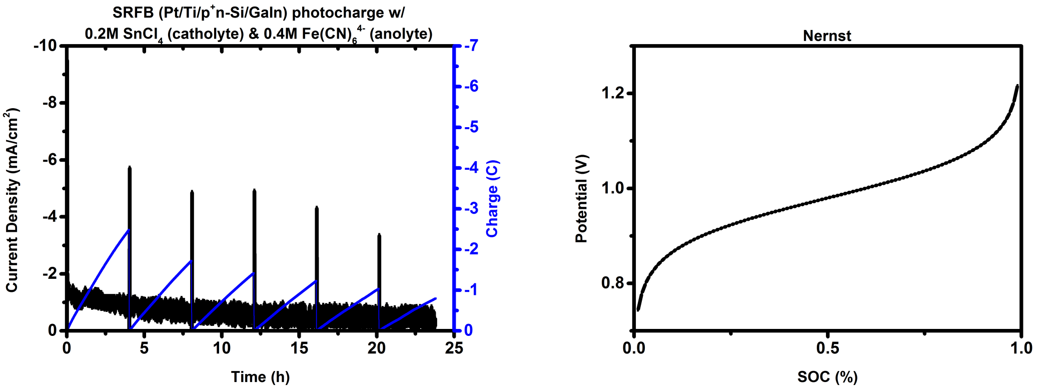

Figure 63: a) Chronoamperometry measurement for $SnCl_4/K_4[Fe(CN)_6] \cdot 3H_2O$ SRFB and b) theoretical cell voltage based on Nernst equation.

Appendix E: Supporting information on GaP-based SRFB

Figures 64 65 depict the optimization process of the GaP photoelectrodes in order to find the optimal configuration. Both n and p type GaP are used, combined with various prospective electron and hole transport layers, are incorporated in the half cell. The onset potential and photocurrent output are measured.

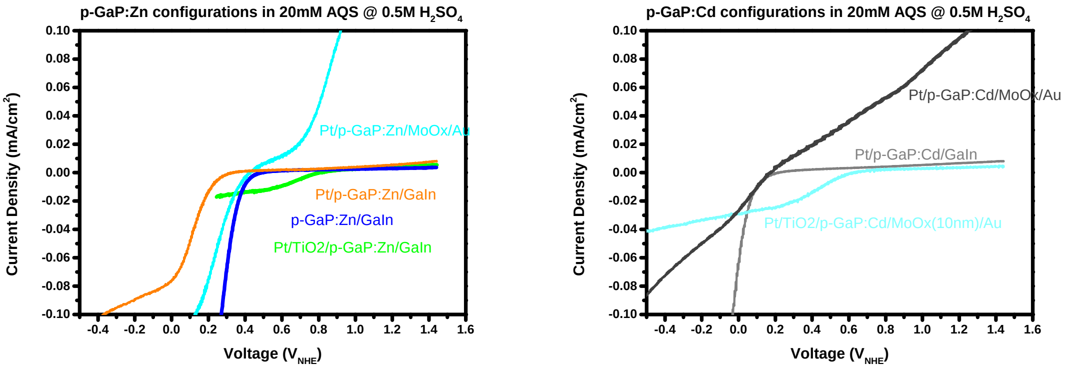

Figure 64: All p-type GaP a) Zn- and b) Cd-doped LSV's for onset potentials and current output.

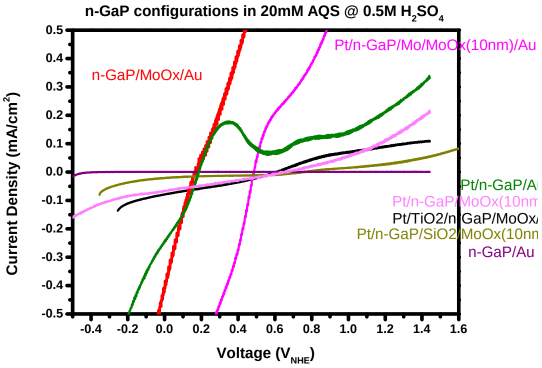

Figure 65: All n-type GaP LSV's for onset potentials and current output.

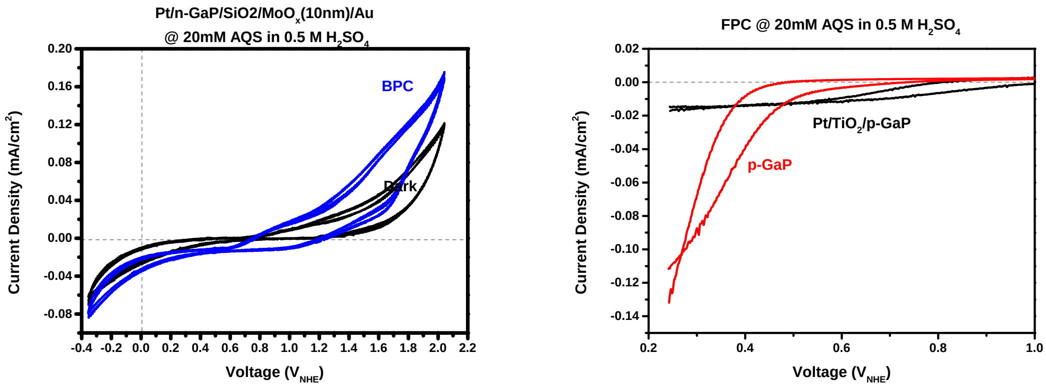

Figure 66: a) Influence of SiO_2 on GaP as high band gap oxide to prevent trap-state recombination and b) influence of Pt conducting layer and TiO_2 ETL on p-GaP.

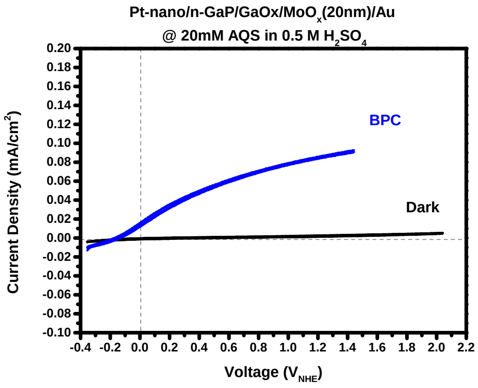

Figure 67: Influence of GaO_x native oxide on GaP surface.

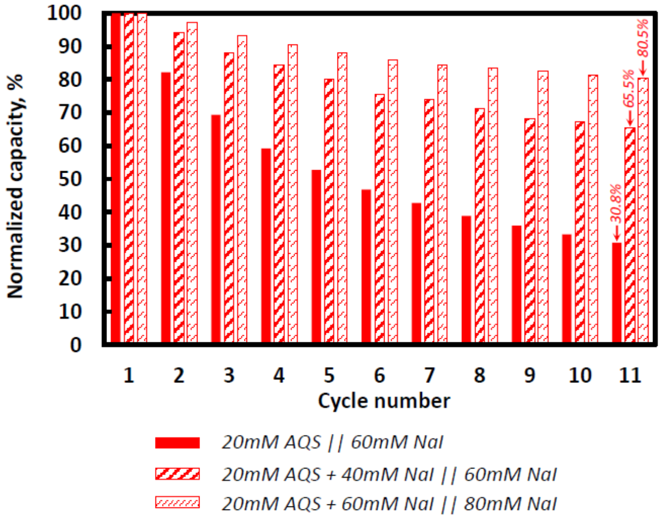

Figure 68: The AQS-NaI RFB capacity loss over the course of several cycles, for different electrolyte compositions.

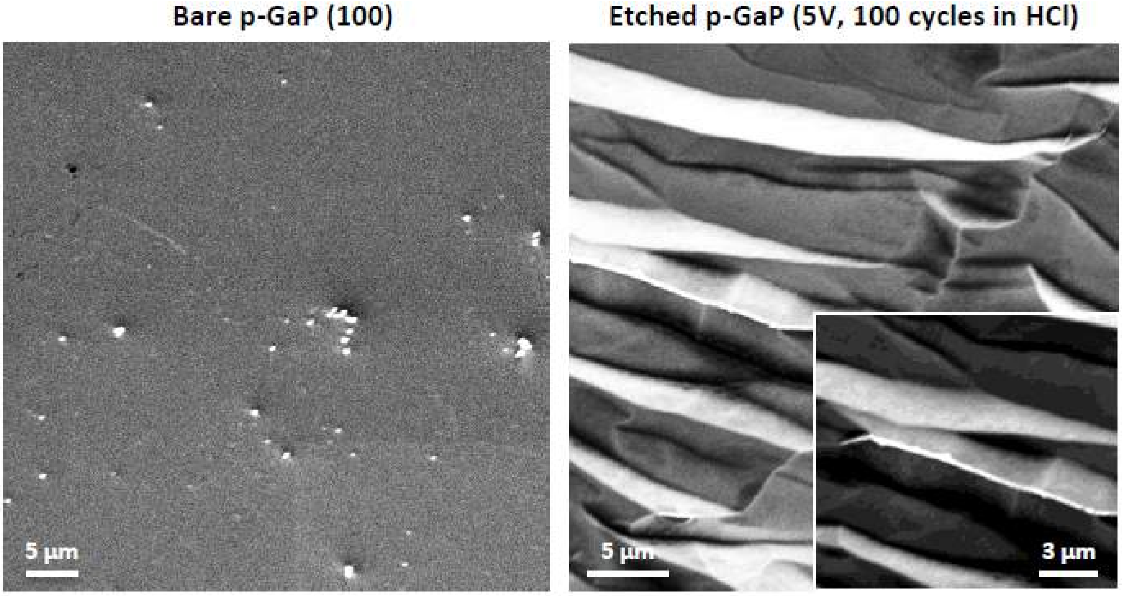

Figure 69: The SEM studies of GaP surface modification after applying cathodic current for several cycles in acidic environment.

Appendix F: Rightslink by Copyright Clearance Center

Copyright Clearance Center RightsLink®

Home | Account Info | Help

ACS Publications Most Trusted. Most Cited. Most Read.

Title: Solar Redox Flow Batteries with Organic Redox Couples in Aqueous Electrolytes: A Minireview

Author: Kristina Wedege, Dowon Bae, Wilson A. Smith, et al

Publication: The Journal of Physical Chemistry C

Publisher: American Chemical Society

Date: Nov 1, 2018

Logged in as:
Dowon Bae
Account #:
3001519177

LOGOUT

PERMISSION/LICENSE IS GRANTED FOR YOUR ORDER AT NO CHARGE

This type of permission/license, instead of the standard Terms & Conditions, is sent to you because no fee is being charged for your order. Please note the following:

- Permission is granted for your request in both print and electronic formats, and translations.
- If figures and/or tables were requested, they may be adapted or used in part.
- Please print this page for your records and send a copy of it to your publisher/graduate school.
- Appropriate credit for the requested material should be given as follows: "Reprinted (adapted) with permission from (COMPLETE REFERENCE CITATION). Copyright (YEAR) American Chemical Society." Insert appropriate information in place of the capitalized words.
- One-time permission is granted only for the use specified in your request. No additional uses are granted (such as derivative works or other editions). For any other uses, please submit a new request.

If credit is given to another source for the material you requested, permission must be obtained from that source.

BACK | CLOSE WINDOW

Copyright Clearance Center RightsLink®

Home | Account Info | Help | LIVE CHAT

ACS Publications
Most Trusted. Most Cited. Most Read.

Title: Effect of microscopic discontinuity of metal overlayers on the photovoltages in metal-coated semiconductor-liquid junction photoelectrochemical cells for efficient solar energy conversion

Author: Yoshihiro Nakato, Keiichi Ueda, Hiroyuki Yano, et al

Publication: The Journal of Physical Chemistry A

Publisher: American Chemical Society

Date: Apr 1, 1988

Logged in as:
Dowon Bae
Account #:
3001519177

LOGOUT

PERMISSION/LICENSE IS GRANTED FOR YOUR ORDER AT NO CHARGE

This type of permission/license, instead of the standard Terms & Conditions, is sent to you because no fee is being charged for your order. Please note the following:

- Permission is granted for your request in both print and electronic formats, and translations.
- If figures and/or tables were requested, they may be adapted or used in part.
- Please print this page for your records and send a copy of it to your publisher/graduate school.
- Appropriate credit for the requested material should be given as follows: "Reprinted (adapted) with permission from (COMPLETE REFERENCE CITATION). Copyright (YEAR) American Chemical Society." Insert appropriate information in place of the capitalized words.
- One-time permission is granted only for the use specified in your request. No additional uses are granted (such as derivative works or other editions). For any other uses, please submit a new request.

If credit is given to another source for the material you requested, permission must be obtained from that source.

BACK | CLOSE WINDOW

Appendix G: Unravelling the practical solar charging performance limits of redox flow batteries based on a single photon device system

Sustainable Energy & Fuels

PAPER

Cite this: *Sustainable Energy Fuels*, 2019, 3, 2399

Received 29th May 2019
Accepted 3rd July 2019

DOI: 10.1039/c9se00333a

rsc.li/sustainable-energy

Unravelling the practical solar charging performance limits of redox flow batteries based on a single photon device system†

Dowon Bae, ‡* Gerrit M. Faasse,‡ Gerasimos Kanellos and Wilson A. Smith *

In recent years, solar redox flow batteries have attracted attention as a possible integrated technology for simultaneous conversion and storage of solar energy. Unlike solar water splitting technologies which require at least 1.8 V for meaningful performance, a lesson learned from previous studies on solar redox flow batteries (SRFBs) is that even single-photon devices can demonstrate unbiased photo-charging owing to the flexibility of redox couple selection. Thus, in this paper, we present a theoretical model reflecting experimental parameters, such that we can highlight important parameters that merit the most attention in further studies towards the practical development of SRFBs. Importantly, the results clearly show how to choose an optimum combination of semiconductors and redox couples under unavoidable conditions that a practical system would encounter, including, but not limited to, optical loss by the electrolyte, overpotential, device architecture and chemical potentials.

1. Introduction

In 2017 the contribution from renewable sources to the electricity production in OECD countries totalled 23.7%, of which 26.9% was from solar energy (*i.e.*, photovoltaic (PV) and solar-thermal power).[1] However, continued implementation is facing challenges concerning the security of supplies because of the intermittent nature of sunlight. In this context, storing solar energy directly in hydrogen or other chemicals *via* photoelectrochemical (PEC) water splitting or CO_2 reduction has been regarded as a particularly attractive technology.[2–5] However, the sluggish reaction kinetics (*i.e.*, high overpotential) hampers their widespread implementation.[2,3] In terms of technological readiness, the most feasible approach to store solar energy would be a photovoltaic (PV) panel integrated with Li-ion batteries as an energy storage system (ESS), but this method faces critical issues related to frequent thermal runaway[6,7] and cost of the battery module.[8] Alternatively, solar rechargeable redox flow batteries (SRFBs) are being studied as a means of simultaneous storage of solar energy into chemicals, which can be readily utilized to generate electricity *via* reversible redox reactions.[9–11] Generally, redox flow batteries (RFBs) present facile reaction kinetics, which can be several orders of magnitude faster than water oxidation,[12] and are deemed safer than other solid-state batteries owing to their wide discharging voltage range.[13,14] Additionally, the system power rating and discharging time of RFBs surpass those of conventional batteries.[15,16]

The architectural concept of the SRFB is a combination of a redox flow battery (RFB) and a PEC or PV-assisted device, which may be fully integrated into a single cell or separated into an RFB and a solar charging component. Since the initial pioneering work in 1976 by Hodes *et al.*,[17] a lot of effort has been put into this field relatively recently[9,10,18–22] in the wake of the maturation of PEC water splitting materials which offer practical utilization of PV materials for electrochemical applications.[11] Unlike conventional PEC water splitting, SRFBs offer flexibility with respect to redox potential and solubility in a wide pH range. In recent studies, it is apparent that conventional inorganic redox chemicals combined with various organic chemicals allow an unprecedented wide selection of redox energy level matching with the photovoltage for an optimized charging reaction.[11,23,24] Despite the above-mentioned advantages, one of the major drawbacks is the relatively low solar-to-chemical efficiency (*i.e.*, charging efficiency, STC% hereinafter). An integrated system with a photo-anode and -cathode immersed in the PEC charging cell in a dual-bed or tandem device configuration (2-photon-device) leads to an increased photovoltage that is enough for the redox couples with a high cell voltage ($\geq$0.8 V).[10,18,20] Most recently, Urbain *et al.* reported a record-breaking STC% (12.3%) using a monolithic tandem a-Si/a-Si PV-assisted device which showed a high photovoltage (>2 V) owing to the wide bandgap of the two absorbing layers (*ca.* 1.95 eV).[18]

Materials for Energy Conversion and Storage (MECS), Department of Chemical Engineering, Delft University of Technology, Van der Maasweg 9, 2629 HZ Delft, The Netherlands. E-mail: d.bae@tudelft.nl; w.smith@tudelft.nl

† Electronic supplementary information (ESI) available. See DOI: 10.1039/c9se00333a

‡ These authors contributed equally to this work.

Nonetheless, the 2-photon-device approach is cost-advantageous only when both photo-absorbers have an ideal band-gap pairing and are made using technologies providing a similar cost per unit output power.[25] Another critical challenge is the demonstration of a wide band-gap top cell with a cost below \$100 per m^2 and an efficiency above 20%, which is essential for having a lower LCOE (levelized cost of electricity) than a single-photon-device.[25,26] Meanwhile, a lesson learned from previous SRFB studies is that even single-photon-devices can demonstrate unbiased photocharging owing to the flexibility of redox couple selection.

Previously published STC efficiencies for single photon devices are shown in Fig. 1, showing the efficiencies and the materials used. Initial studies in the eighties demonstrated meaningful charging efficiencies using n-WSe$_2$.[27,28] However, these references used a stationary redox chemical cell with a non-standard light source (*e.g.*, He–Ne laser; 150 mW cm^{-2}). Recently, McKone and co-workers[22] have demonstrated an SRFB under standard light conditions (AM 1.5 irradiation). A crystalline WSe$_2$ photocathode was used for charging an RFB with NaI and AQDS (2,7) redox couples with a cell voltage (V_{cell}) of 0.46 V with an STC% of 3.9%, which is one of the highest values among the SRFBs with an unbiased single PEC device.[22] Interestingly, examples with already proven PEC materials, such as c-Si, GaAs, DSSC, *etc.*,[19,29–31] exhibited quite low charging efficiencies. For the sake of consistency, all STC% data are calculated using the light-driven photocurrent measured at 0% state of charge (SOC%).

For an ideal case, *i.e.*, the Shockley–Queisser limit, one would expect a theoretical maximum efficiency of up to around 33%. However, Fig. 1 shows that the charging efficiencies are far from this maximum. There is even a precondition of sufficient solubility of the redox couples to balance the energy storage capacity, and thus there remains substantial room for improvement considering the gap between the performances of the SRFB with a single-photon-device and the state-of-the-art PV cell technology. The performance of the stationary redox cells in the bubble chart (Fig. 1) alone also highlights the experimental potential of SRFBs. In this respect, modeling the theoretical conversion efficiency for a PEC device containing SRFBs is useful as it can identify practical performance limits and aspects of material properties that need to be enhanced. A number of previous studies have addressed the theoretical performance limit for both single- and 2-photon PEC water splitting devices.[32–35] However, to the best of our knowledge, no study on theoretical device performance has been done for SRFB applications.

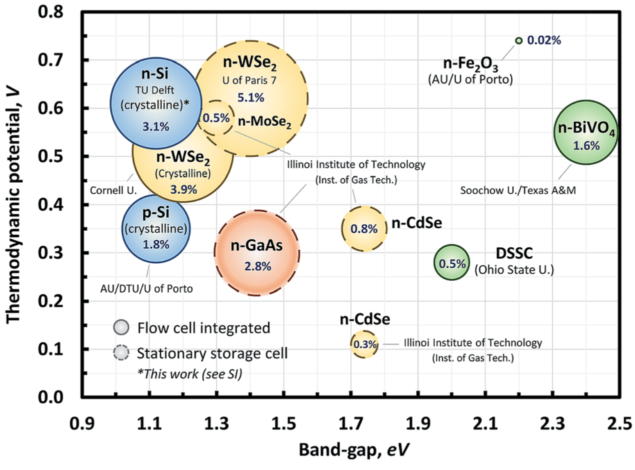

Fig. 1 Experimental STC% of several unbiased single photo-absorber cells is shown with different combinations of the photo-absorber band-gap and thermodynamic potential (defined as the difference between the redox potential of the respective oxidation and reduction couples). For clarity, Si-based materials are colored in blue; chalcogenides in yellow; III–V in orange; and metal-oxides in green. Note that the data point with the dashed line was subtracted from the experimental results in this work (this will be addressed later in the Results and discussion section). Detailed working conditions and citation information for the references for the chart can be found in the ESI (Table S1†).

In this work, we aim to provide a model for studying the charging performance of SRFBs by considering the inherent nature of SRFB operation, including, but not limited to, optical loss by the electrolyte and overpotential, to reveal the practical photo-charging performance limit of a single-device-based system. We emphasize that the calculations reflect experimental parameters from previous research studies and/or our own measurements (particularly, photocharging using c-Si with Fe(CN)$_6{}^{3-}$ and NH$_4$Br; Fig. 1, circle with an asterisk) so that we can highlight which properties merit the most attention in further studies towards the practical development of SRFBs.

It should be noted that for any PEC or PV-assisted device, there needs to be a corresponding energy level matching between the photo-device and redox couples as described in a previous study.[11] While understanding that these counter reactions is important, this work only focuses on the analysis of photo-charging performance with an assumption of appropriate energy matching. For readers interested in energy level matching and analysis on the electrochemical performance of RFBs we suggest previous studies by McCulloch *et al.*[30] and Wedege *et al.*[11] and technological review studies by Ye *et al.*[36] and Park *et al.*[23] It is also worthwhile to note that theoretical calculations are valid only if there is no positive photo-redox effect, such as modification of the redox properties owing to photo-excited states, as demonstrated in dye-sensitized PEC cells.[37,38]

2. Experimental

2.1. Theoretical modeling

In most instances in this work, photo-devices are assumed to possess the following properties: (I) photon absorptivity with an energy level lower than the band gap energy (E_g) is not considered (*i.e.*, light utilization by intermediate states is zero). (II) The device has ideal contact with both the counter electrode and the conducting layer at the solid/liquid interface. (III) The current output is not limited by mass transport (*e.g.*, flow or circulation rate of the electrolyte). (IV) Dynamics due to the state-of-charge ratio change is not considered. Under the given assumptions, the following diode equation is derived by Shockley and

Queisser,[39] in which the empirical ideality factor n was added later (*e.g.*, described by Green[40]) to calculate the voltage output as a function of the current density:

$$j = j_{\mathrm{max,ph}} - j_0\left[\exp\left(\frac{q(V + j\Omega_{\mathrm{s}})}{nkT}\right) - 1\right] - \frac{(V + j\Omega_{\mathrm{s}})}{\Omega_{\mathrm{sh}}} \tag{1}$$

where $j_{\mathrm{max,ph}}$ is the theoretical maximum photocurrent density, q is the elementary charge, V is the voltage, k is Boltzmann's constant, T is the temperature and Ω_{s} and Ω_{sh} are the series and shunt resistances, respectively. j_0 is the dark saturation current density determined *via* the following equation simplified by Green[40] based on black-body emission theory:

$$j_0 = nqA_{\mathrm{ph}}\left(\frac{2\pi kT}{h^3c^2}\right)\left[{E_{\mathrm{g}}}^2 + 2kTE_{\mathrm{g}} + 2(kT)^2\right]\exp\left(\frac{-E_{\mathrm{g}}}{kT}\right) \tag{2}$$

where A_{ph} is the emitting area of the photo-absorber relative to the absorbing area (*e.g.* in the case of a regular slab of material, this would be a factor of 2). h is Planck's constant, c is the speed of light, and E_{g} is the band gap of the photo-absorber material. It is worth noting that eqn (1) and (2) depend on the ideality factor (n). To compensate for non-idealities, like non-radiative and Auger recombination, refractive index and other losses, the ideality factor n could be varied from 1 to 2.[41] Although this factor could be easily implemented in eqn (1), changing n solely in eqn (1) and (2) would lead to misleading and non-physical results, since calculations show that it would increase the open circuit voltage of the device, while in practice, a higher ideality factor leads to a lower open circuit voltage as described elsewhere.[33] Therefore, this work will not take into account the impact of the ideality factor on the modeled STC%.

One important point to discuss is how $j_{\mathrm{max,ph}}$ can be defined. While conventional studies on PVs and solar-fuel use standard air mass 1.5 (*i.e.*, AM 1.5) as an incident photon source, most SRFBs use electrolytes with distinctive colours which can lead to a significant loss in $j_{\mathrm{max,ph}}$ due to parasitic light absorption. So far, nearly all studies have employed front-side illumination despite the inevitable optical-loss by the electrolyte.[10,19,20,42,43] Only a few studies have been performed using back-side illumination, which allows direct photon absorption on a dry surface.[9,18,44] Döscher[35] and Seger[33] demonstrated a method to model solar water splitting technologies by using a detailed balance between the PEC device and optical losses by water with various overpotentials of the catalysts. However, light absorption by the electrolyte of SRFBs is incomparably high and has a strong dependence on the type of redox couples used. Unfortunately, experimentally measured absorbance data cannot be directly applied to the model, since all PEC systems have different electrolyte thicknesses and redox chemical concentrations. Hence, instead, the molar absorptivity (molar extinction coefficient, ε) data are employed for the modeling work. Simultaneously, practical effects, including reflection losses at the light-illuminated surface, are taken into account. According to the analysis by Frijnts *et al.*,[45] the contribution of optical loss by direct reflection in the case of a flat c-Si device without an anti-reflection (ARF) layer reaches over 5.8 mA cm^{-2}, whereas the textured device with an ARF layer showed a loss of only 3.4 mA cm^{-2}. Therefore, losses due to both reflection and parasitic absorption are considered, by including their effects on the absorbed solar flux, and consequently on $j_{\mathrm{max,ph}}$ (detailed equations are shown in Section S2 of the ESI†).

For the back-illuminated case, total reflectance of the device is simply the reflectance spectrum of the photo-absorber (covered with any available ARF layer). In the case of front-side illumination, there are three reflection interfaces: the air–window, window–electrolyte and electrolyte–electrode interface. For each interface, the reflectance (R) is calculated using the Fresnel equation:

$$R = \frac{|n_2 - n_1|^2}{|n_2 + n_1|^2} \tag{3}$$

in which n_1 and n_2 are the (complex) indices of refraction of the substances in front of/behind the respective interfaces. In this equation, $n_{\mathrm{air}} \approx 1$, $n_{\mathrm{glass}} \approx 1.5$ and $n_{\mathrm{electrolyte}} \approx 1.33$. It is worth noting that the complex part of the index of refraction is negligible since calculations show very low numbers (*i.e.*, 10^{-4} to 10^{-7}). For the $n_{\mathrm{electrode}}$, the only data used in this work is the refractive index of the well-documented silicon photo-absorber,[46] from which the experimental absorptivity (α [cm^{-1}]) is obtained. For the contour plots (shown in the results of this work), by continuously varying the bandgap energy, the reflection at the electrode surface, although significant, is not considered in detail, but rather a constant reflection percentage is assumed.

The effect of Ω_{sh} is assumed to be negligible, since commercially available PV devices have Ω_{sh} with triple digits (>2 kΩ cm^{-2}).[47,48] Typically, power losses caused by the presence of a shunt resistance are due to manufacturing defects, rather than poor device design. However, a fill factor loss due to the presence of Ω_{s} cannot be eliminated. Unlike conventional PV systems with Ω_{s} in the range of 3–10 Ω cm^{-2},[45,49] PEC or PV-assisted systems have additional interfaces at the liquid side to protect devices from corrosion, and this interlayer with a conducting material causes an increased resistance. In addition, electrochemical losses due to redox reactions at the solid/liquid interfaces as well as ionic charge transport (*i.e.*, solution resistance, R_{sol}) are taken into account as one of the contributing factors to the overpotential (*i.e.*, resistance overpotential, η_{r}) to satisfy the following basic condition for unbiased photo-charging:

$$E_{\mathrm{ph}} \geq E_{\mathrm{redox}} + E_{\mathrm{dev.\ loss}} + \eta_{\mathrm{redox}} \tag{4}$$

where E_{ph} is the photovoltage derived by the photo-device, $E_{\mathrm{dev.\ loss}}$ is the device losses due to factors mentioned above (electrical resistance, reflection, *etc.*), and η_{redox} is the redox overpotential. E_{redox} is the thermodynamic potential which is equivalent to the difference between the redox potentials of redox couples (*i.e.*, $|\varphi_{\mathrm{red}} - \varphi_{\mathrm{ox}}|$). In general, E_{redox} is a function of the state of charge (SOC) of the SRFB, governed by the Nernst equation, rewritten in terms of the SOC:

$$E_{\mathrm{redox}} = E^0_{\mathrm{redox}} + \frac{RT}{n_{\mathrm{electrons}}F}\ \ln\ \frac{\mathrm{SOC}^2}{(1 - \mathrm{SOC})^2} \tag{5}$$

in which E^0_{redox}, is the experimentally observed redox potential (at 50% SOC), R is the gas constant, $n_{\text{electrons}}$ is the number of electrons participating in the reaction and F is Faraday's constant.

The operating current j_{op} can be obtained as the maximum possible current density in the current–voltage characteristic of eqn (1) at a voltage that also satisfies the condition in eqn (4). It is worth noting that the experimental j_{op} ($j_{\text{op,exp}}$) is defined by the photocurrent at zero bias voltage using a two-electrode setup. Knowing the operating current, the STC% can be calculated using the following equation:

$$\text{STC\%} = \frac{j_{\text{op}} \times E_{\text{redox}}}{P_{\text{input}}} \times 100 \tag{6}$$

in which P_{input} is the input power of the incoming solar radiation. Knowing the efficiency, the effect of several factors, such as the solution resistance, kinetic overpotentials and electrode positioning (*i.e.*, front- or backlit configuration) can be modeled.

2.2. Sample preparation

Front-side illuminated photocathodes (pn$^+$–Si) were prepared as described elsewhere[19,50–52] and used with further optimization. In the case of the back-illuminated sample (Fig. 2a), a shallow np$^+$-junction was formed at the surface of n-type c-Si wafers. Pt thin films were also sputtered at room temperature as a conducting layer with a Ti adhesion layer. Further experimental information can be found in the ESI (Section S3†).

In addition to Pt, various materials, such as carbon, Ti, TiO_2, and Au, have been used to provide experimental overpotentials and exchange current densities for the verification of the theoretical model. All conducting layers have been deposited using the same sputtering technique as previously mentioned at room temperature. Fabricating an SRFB requires careful selection of the conducting material since some redox potentials, such as $V^{3+/2+}$, are favourable for the hydrogen evolution reaction (HER) that can lead to mechanical damage to the system.[11]

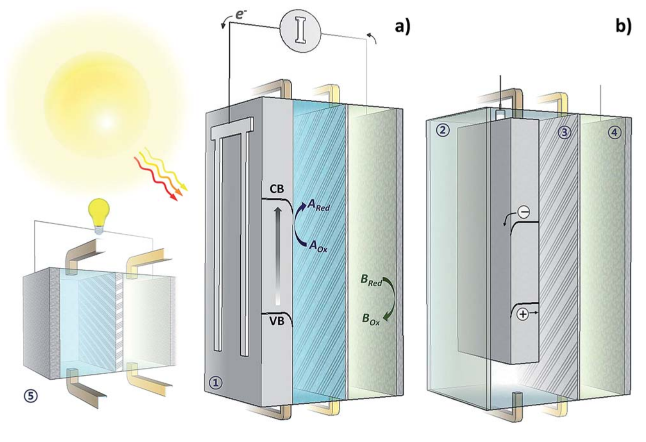

Fig. 2 Schematic of solar charging compartments for the SRFB system. (a) Charging cell with a back-side illuminated device and (b) cell with a front-side illuminated device (*i.e.*, illuminated through the window (2) and the electrolyte). The photocathode (1) in the catholyte (with redox couple A) and a polarizable counter electrode (4) in the anolyte (with redox couple B) are separated by an ion exchange membrane (3). In practical applications, an RFB stack (5) is connected in series with storage tanks and pumps (not shown) for discharging the solar charged electrolytes. Subscripts (Ox and Red) denote the oxidized form and reduced form of the redox couples. CB and VB correspond to the conduction and valence band edges of the semiconductor, respectively. Note that the illustration is not to scale.

2.3. Characterization

The electrochemical measurements of the photoelectrodes were conducted using a three-electrode and a two-electrode configuration. Solar charging has been done under simulated AM1.5 solar irradiation (100 mW cm^{-2}) for both back- and front-illuminated cases (Fig. 2a and b). During the measurements, 40 mL of the electrolyte was continuously circulated using a peristaltic pump at 70 mL min^{-1}. Linear sweep voltammetry (LSV), chronovoltammetry measurements were performed with a carbon felt counter electrode. The solutions were purged with nitrogen before and during measurements. The absorbance and reflectance spectra were recorded by using a UV-vis spectrometer to estimate parasitic absorption by the electrolyte and reflection loss at the sample surface. Further experimental information can also be found in the ESI (S3†).

3. Results and discussion

When varying the cell voltage (*i.e.*, thermodynamic potential to drive the redox reaction) as well as the band-gap of the photoabsorber, a 2D contour-plot of the STC efficiency is obtained. This format will be used to assess several parameters. In Fig. 3a the ideal case is shown, in which no losses, for instance, due to parasitic light absorption, reflection or resistances, are taken into account. It is found that the theoretical maximum STC efficiency for a single-photo-absorber device is 32.4%, which concurs with literature estimations for PV solar cells.[39,53] However, the SRFB system allows a wider operational range than the PEC water splitting system which has a fixed thermodynamic energy barrier for driving the redox reaction (*i.e.*, water oxidation at 1.23 V). The top left of the plot shows no efficiency data, due to the limited photovoltage with respect to E_{redox}. When moving towards a higher bandgap energy, the STC% is limited by the number of incoming photons only with an energy higher than E_g. This figure indicates that there is an optimum thermodynamic potential depending on the band-gap of the absorber material, and finding this optimum could drastically enhance the solar charging performance of SRFBs.

In Fig. 3b and c, the effect of parasitic light absorption by the electrolyte $[Fe(CN)_6]^{3-}$ and V^{3+} (in 1 M NH_4Cl and HCl, respectively) is shown for a concentration of 0.3 M and a path length of 1 cm. These figures mimic the working environment of a PEC compartment where the photoelectrode is directly immersed in the electrolyte. As shown in these figures, the maximum STC% decreases to 27.2% and 17.2% for $[Fe(CN)_6]^{3-}$ and V^{3+} respectively. Moreover, the shape of the efficiency-landscape changes depending on the exact absorption spectrum of a given electrolyte (see also Fig. S1† for the AQS/$AQSH_2$ and I^-/I_3^- cases).

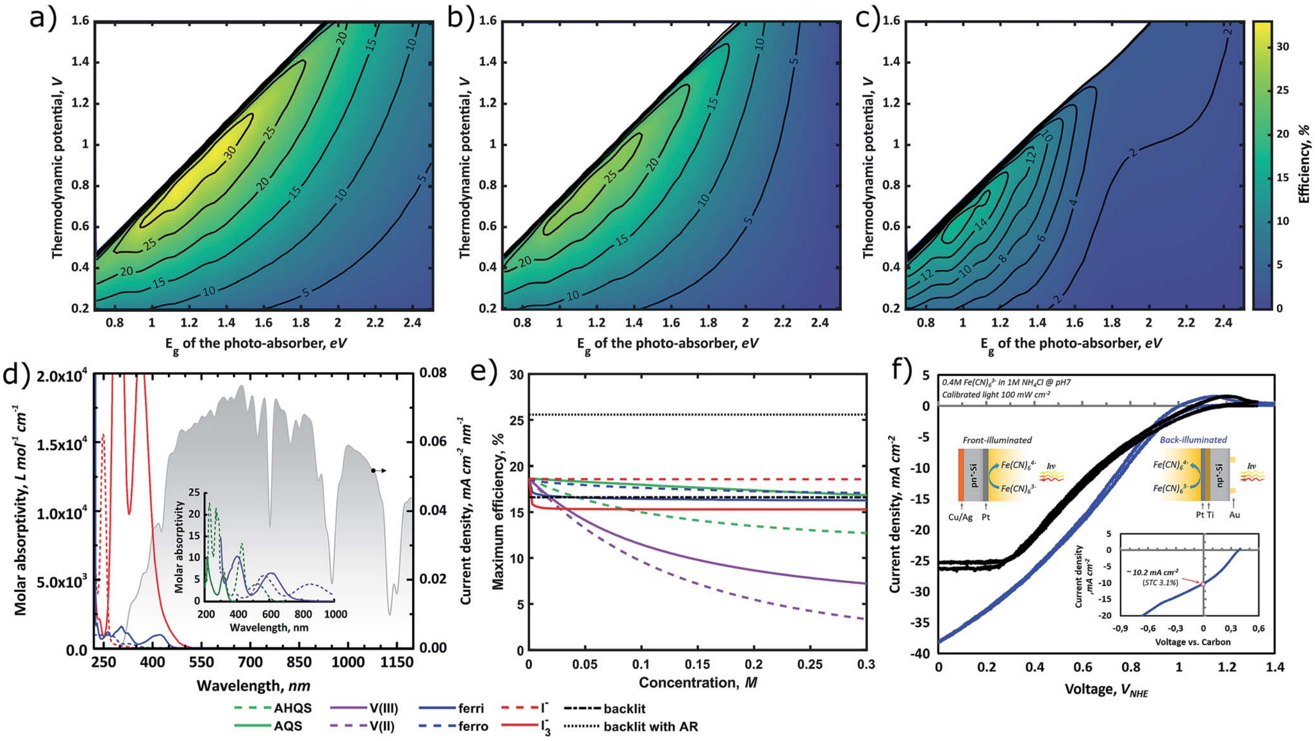

Fig. 3 Efficiency plotted as a function of the thermodynamic potential and the bandgap of the photo-absorber. (a) The ideal case without any kinetic, resistance, or parasitic light absorption/reflection losses. The same plot in (b) and (c), but the reflection from the window and parasitic light absorption of 0.3 M ferricyanide and V^{3+} (with an optical path length of 1 cm) respectively are taken into account. (d) Experimental absorption spectra of several electrolytes overlapped with the photon flux of the AM1.5 spectrum (depicted by the shaded area). (e) The concentration dependence of the maximum efficiency for a 350 μm c-Si photo-absorber. The experimental LSV curve in (f) shows that in the case of a 0.4 M ferricyanide electrolyte, a front-side illuminated configuration results in a significantly lower saturation photo-current, which concurs with the modeled trends. The inset shows the LSV for a dual-electrolyte cell (*i.e.*, 2-electrode configuration), resulting in a current density of 10.2 mA cm^{-2}, corresponding to an estimated STC of 3.1% at a cell voltage of ~300 mV.

This makes finding the optimum $E_{\text{redox}}/E_{\text{g}}$ combination extensively more complex. In Fig. 3d, the experimental absorption spectra, based on the literature[54–56] and experimental measurements, overlap with the photon flux (in current density) converted from the standard AM1.5 spectrum, showing the impact of electrolyte selection on the incoming solar spectrum. Note that this result does not take into account the individual effect of the supporting electrolyte since there is no significant loss up to 10 cm of water thickness in the case of a single-photon device.[35] Overall, the reduced incoming-photon flux shifts the optimum $E_{\text{redox}}/E_{\text{g}}$ combination towards a smaller value such that an electrolyte with a high concentration is required for balancing the discharging capacity.

Another factor used to differentiate between the efficiency of the back- and front-side illumination configurations is the possibility of introducing an antireflective treatment (*e.g.*, AR coating). In the case of the electrode being immersed in the electrolyte, some corrosion protective layers for photoelectrodes (*e.g.*, TiO_2 with c-Si) show anti-reflective properties; however, typical AR treatments, such as MgF_2 and SiO_2 layers, are not applicable in this case due to their stability which is pH dependent.[3] To account for this, the reflectance spectrum of c-Si with and without an AR coating is used for modeling the back-illuminated efficiency, while the (complex) refractive indices of air, glass, electrolyte and bare silicon are used to model the front-illuminated efficiencies. As shown by the dash-dot line in Fig. 3e, almost 8% efficiency loss is expected in the case of bare c-Si indicating the importance of having an AR treatment to minimize reflection losses. It is interesting to note that the back-illuminated bare c-Si case shows slightly lower charging efficiency than the front-illuminated cases in the low concentration range. According to the Fresnel equation (eqn (3)), the higher refractive index of the electrolyte with respect to air leads to reduced reflection of bare silicon for a front-illuminated configuration (also see Fig. S2 in the ESI†) with respect to back illumination, resulting in higher efficiencies in the cases where this effect is more dominant than electrolyte absorption.

The concentration dependency of the electrolyte on the STC% in Fig. 3e highlights that conventional vanadium-based redox couples with a front-illumination architecture cannot be considered as an efficient charging method for a high storage capacity system (*i.e.* high concentration) due to their high molar absorptivity in the high wavelength range (see the inset of Fig. 3d). On the other hand, the STC% with an iodide electrolyte is relatively less sensitive to the concentration but it showed drastic molar absorptivity in the short wavelength region (Fig. 3d). This study of the absorption spectra is particularly important for the wide band gap semiconductor-based device.

For instance, GaP (2.24 eV) has a large absorption spectral overlap with the AQS electrolyte, leading to a drastic drop in J_{ph} upon the addition of AQS into H_2SO_4 (Fig. S3 in the ESI†). The experimental LSVs in Fig. 3f support the modeled trends of the expected higher photo-currents (and thus efficiencies) for a back-illuminated configuration. The saturation current of the front-side illuminated device is significantly lower than that of the back-illuminated case, despite an otherwise almost identical setup (see Fig. S4 in the ESI† for detailed charging/discharging in RFB mode).

In a practical model, kinetic overpotentials should be considered, as the electron transfer between the photo-absorber and the electrolyte is never perfect. In general, an RFB presents facile kinetics, which can be several orders of magnitude faster than water oxidation that requires a high overpotential.[12] In Fig. 4a and b, the effects of fixed kinetic overpotentials (η_k) of 0.2 V and 0.6 V on the efficiency-landscapes respectively are shown. First, it can be seen that the maximum STC%, as opposed to the previous electrolyte concentration effect case in Fig. 3a–c, shifts to higher E_g and lower E_{redox}, due to the kinetic overpotential effectively increasing the voltage needed to drive the reaction (eqn (4)).

Moreover, owing to the shift of the contour-plot to higher bandgap energies, the STC% decreases due to reduced absorbed solar flux (as shown more clearly in Fig. 4c). An important aspect is the selection of a conducting material at the solid/liquid interface. Conventionally, high overpotentials arise from the photoelectrode while the counter electrode shows quite fast kinetics. Experimental linear sweep voltammograms (LSVs) of n-type Si electrodes under dark conditions for the cathodic charging of $Fe(CN)_6{}^{3-}$ (Fig. 4d) show how the overpotential varies with the type of conducting layer. The inset shows the LSVs for a carbon felt electrode submerged in an anolyte (NaI and TEMPO-sulfate in this case) which exhibits a negligible overpotential owing to the sufficient active area of carbon felt. Unlike typical RFB systems in which the metallic electrodes or carbon is directly connected to a wire, SRFBs require integration of semiconductors with the conducting layer which may form an energy barrier with unfavourable band-bending at the semiconductor/metal junction. As shown in Fig. 4d, Pt shows outstanding kinetics; however, noble metals like Pt are not recommended for RFB applications since the formation of bubbles due to the concurrent hydrogen evolution reaction may lead to mechanical damage of the system. Addressing designing rules for efficient charge transfer at the solid/liquid interface is beyond the scope of this work.

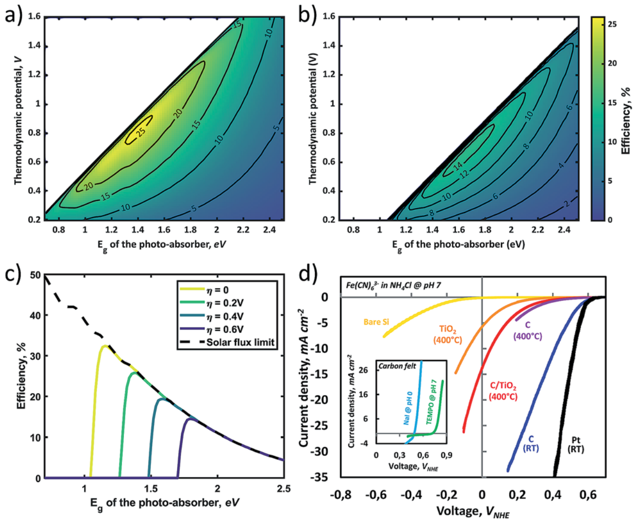

Fig. 4 Efficiency plotted as a function of the thermodynamic potential and the bandgap of the photo-absorber. (a and b) The effect of 0.2 V and 0.6 V kinetic overpotential respectively. In (c) the STC% is plotted as a function of the bandgap-energy for various overpotentials. The dashed black line shows the maximum theoretical efficiency based on the AM1.5 spectrum. In (d), experimental LSV data are plotted for a single silicon photo absorber with various conducting layers, submerged in a $[Fe(CN)_6]^{3-}$ electrolyte (in NH_4Cl at pH 7), showing that the overpotential is strongly dependent on the type of conducting material. The inset depicts the LSV data for a carbon felt electrode, immersed in analytes (NaI and TEMPO-sulfate at pH 0 and 7, respectively).

Fig. 5a and b display the effects of the overpotential and electrolyte resistance, respectively, on the photocharging efficiency landscape for the c-Si case ($E_g = 1.12$ eV). The dashed lines represent the efficiency curves for which surface reflection and shading by the front contact grid (*i.e.*, a dead area of 4% of the total active area[57]) are taken into account. Interestingly, the efficiency loss due to the reflection and shadowing in the case of a photo-absorber with appropriate treatment (*i.e.*, AR and optimized front grid) is limited. Fig. 5a shows the sensitivity analysis by plotting the charging efficiency against the thermodynamic potential. Naturally, it shows a similar trend to that found in Fig. 4c for overpotential variation; an increased overpotential greatly decreases the performance limit and threshold cell voltage (*i.e.*, the potential differential between the catholyte and anolyte). As mentioned earlier, electrolyte resistance (R_{sol}) is one of the dominant contributors to the overpotential, and the plots in Fig. 5b were obtained from calculations with various resistance overpotentials at zero kinetic overpotential. Fig. 5b shows a relatively low sensitivity of the STC% to the electrolyte resistance variation. While a negative shift of the optimum thermodynamic potential is seen along with increasing solution resistance, the threshold potential below which achievable STC% is observed remains almost constant. The solution resistance is often a significant factor under practical working conditions where ionic transfer pathways are on the order of centimeters. Generally, the resistance of an ionic solution depends on the ionic concentration, type of ions, temperature, and geometry in which the current is carried. This is made evident in Fig. 5c, where the conductivity of the electrolytes is highly dependent on the electrolyte type and concentration. For example, for a system with a 1 M NH_4Cl supporting electrolyte and an estimated conductivity of 75 mS cm^{-1} for the redox electrolyte, the total electrolyte resistance for a 2 cm path length (*e.g.*, 1 cm each for catholyte and anolyte) is 11.35 Ω cm^2 (see Section S5 in the ESI† for explicit calculations), implying that the impact of the electrolyte resistance should not be neglected in practical models. The plots for various electrolytes in Fig. 5c were calculated based on data found in the literature,[58–61] where

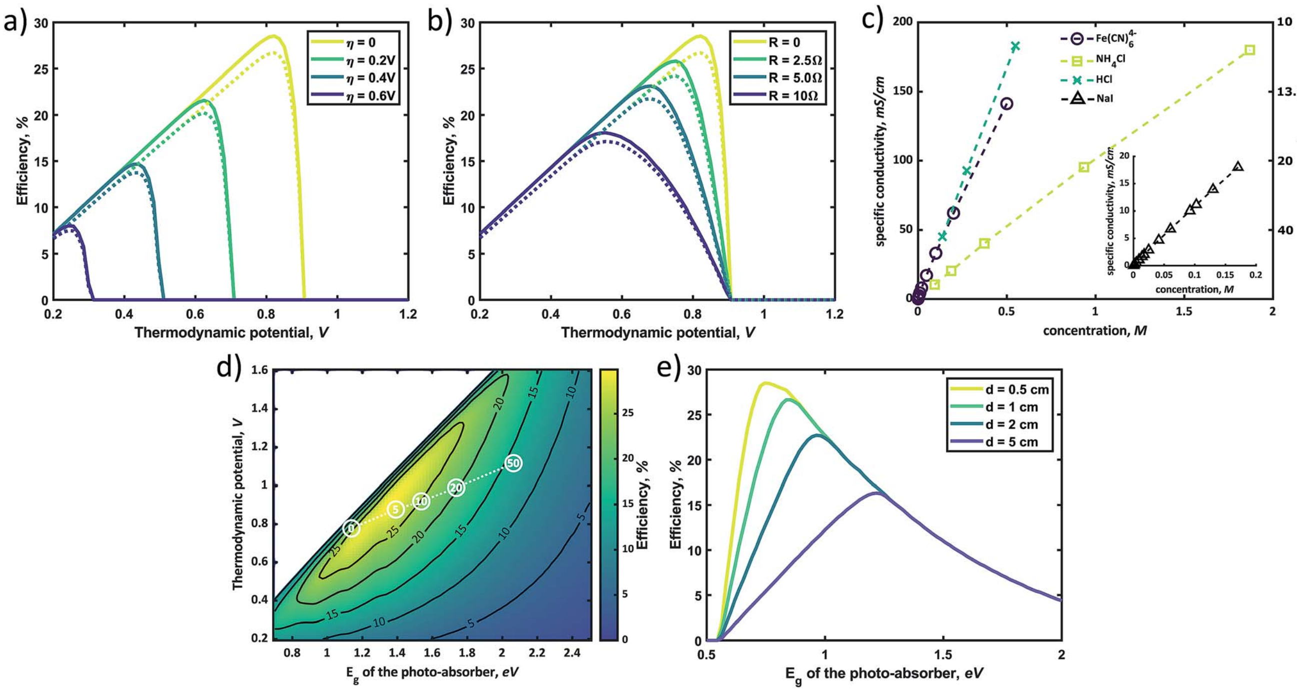

Fig. 5 Sensitivity analysis for each type of loss. The charging efficiency is plotted as a function of the thermodynamic potential in the back-lit configuration for different kinetic overpotentials (a) and solution resistances (b), respectively. The dashed line represents the case in which surface reflection (by AR treated silicon) and contact shading are taken into account. Data found in the literature for the specific concentration are plotted *versus* the concentration of various electrolytes (c). In (d), a contour-plot of the efficiency landscape for an electrolyte resistance of 2.5 Ω cm^2 is shown. The white circles indicate the optimum location (*i.e.*, the optimum bandgap-thermodynamic potential combination) for electrolyte resistances of 0, 5, 10, 20 and 50 Ω cm^2 respectively, showing a shift towards a higher bandgap and higher thermodynamic potential with increasing resistance. The same trend is observed in (e), where the STC efficiency is plotted *versus* the photo-absorber band-gap at a thermodynamic potential of 0.8 V, for various distances between the electrodes, effectively increasing the electrolyte resistance.

the measurements were conducted under precisely controlled conditions (*e.g.*, temperature, electrode distance, purification treatment, *etc.*). As demonstrated in Fig. 5c, it is relatively easy to reduce the solution resistance simply *via* concentration control, whereas a reduction in the overpotential requires careful selection of conducting materials along with electrical and morphological design to provide sufficient conductivity and active sites over the whole surface.

As shown in Fig. 5d, the optimum point shifts towards lower E_g with decreasing solution resistance (white circles). In the extremely low solution resistance case, a lowered optimum point (E_g of 1.2–1.6 eV with an E_{cell} of ~0.6–0.9 V) makes the use of commercial PV materials (*e.g.*, c-Si, CIGSe, and GaAs)[3,62] promising. However, the high ionic strength may potentially lead to corrosion of the materials, which will mostly likely require an additional protection layer. For instance, a solution resistance of 2.5 Ω cm^{-2} corresponds to highly acidic supporting electrolytes (*e.g.*, a 3 M HCl solution). These extremely harsh conditions are not practical considering that most studies in the PEC water splitting field have been conducted in the pH range of 0–14, and still suffer from poor long term stability.[3] Alternatively, minimizing the distance between the electrodes also can be an option to decrease solution resistance. Fig. 5e plots the STC efficiency *versus* the photo-absorber band-gap for which the distance between the electrodes decreases in magnitude, showing that a shorter electrode–electrode distance leads to a shift of the optimum band-gap towards lower values with a higher overall conversion efficiency. Again, we emphasize that this theoretical estimation has been conducted without the consideration of the possible photo-redox effect under the assumption that electrolytes are completely isolated from light due to the back-side illuminated architecture (*e.g.*, Fig. 2a). In the front-illuminated design (*e.g.*, Fig. 2b) case, reduction of the electrolyte thickness may increase the photo-redox effect of some specific redox couples, such as anthraquinones.[37] Furthermore, the reduction of the electrode distance (*i.e.*, channel size) may result in a notable mass transport phenomenon that can lead to a decrease in the obtainable STC% at a certain electrolyte flow rate,[22,63] and this must be addressed using the Butler–Volmer model.

In general, the standard redox potential (E^0_{redox}) is defined as 50% state of charge (SOC), but this SOC-effect should be taken into account for optimizing an SRFB. Fig. 6 exhibits the maximum practical STC efficiency for a set of parameters: R_{sol} = 2.5 Ω cm^2 (corresponding to a highly conductive, but useable electrolyte with an optimized path length of ~ 1 cm), an internal series resistance of 3 Ω cm^2, η_{redox} = 0.25 V with a constant parasitic light loss at the photo absorber of 5% and a contact shading of 4% of the active area. This is done for 10% and 90% SOC to show the effect of charging on the efficiency landscape

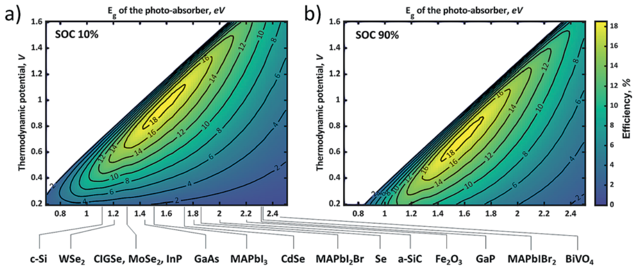

Fig. 6 The efficiency landscape for a realistic set of parameters: $R_{sol} = 2.5\ \Omega\ cm^2$, $\eta_k = 0.25$ V with a constant parasitic light loss at the absorber of 5%, a contact shading of 4% of the active area, an internal series resistance of 3 Ω cm^2 and 10% SOC (a) and the same plot with similar parameters, but with an SOC of 90% (b). Both plots assume a back-lit configuration. Several photo-absorbers are indicated in (a) to point out the possibilities of choosing an optimal photo-absorber.

(Fig. 6a and b, respectively). These plots highlight a shift of the entire STC shape towards a lower thermodynamic potential due to the potential polarization in accordance to the Nernst equation (eqn (5)).[11]

It is expected that an STC% of ~16% can be obtained if the band-gap of the absorber material is within 1.6–1.8 eV and the thermodynamic cell voltage is around 0.9 V and 0.7 V for an SOC of 10% and 90%, respectively. To improve the STC, averaged over the entire charging cycle, this SOC-dependent shift should be taken into account when choosing optimal redox couples. Considering the fact that changing the redox couples during the operation is not unrealistic, these figures with SOC variance also imply that one should choose a photo-absorber material with a larger photovoltage than needed to allow operational flexibility. As discussed in a previous report, Wedege *et al.* demonstrated 95% SOC using a c-Si photocathode which exhibits a photovoltage exceeding the thermodynamic cell voltage by approximately 30%.[19]

When comparing Fig. 6 to Fig. 1, it can be seen that while practical parameters are taken into account for modeling the photo-charging performance, most experimental data are still far below the theoretical limit. It is partly because of the fact that most of these experimental studies have been demonstrated using a front-illuminated configuration showing a decrease of up to 34% in the theoretical photo-charging limit with respect to the back-illuminated configuration as shown earlier in Fig. 3. In this sense, the c-Si sample with ferricyanide/NH_4Br (at pH 7) results in an STC% of around 3.1% with back-side illumination (Fig. 3f) which can be considered as a promising result. There is still, however, the possibility of degradation of bromine and ferricyanide molecules to form toxic side products, such as bromic acid and hydrogen cyanide gas, respectively,[64,65] and this needs to be addressed for further development. Although the demonstrated theoretical model can be used to perform several sensitivity analyses and identify general trends, it is not yet suited to cover all specific experimental conditions in a single figure. As a remedy for this drawback, video clips showing dynamic contour plots with continuous parameter changes are presented in the ESI† to help the readers in tracking optimum combinations of thermodynamic potentials and band-gaps of the semiconductors.

4. Conclusions

In this work, the necessity of accurately matching the photo-absorber bandgap-energy with the thermodynamic potential of the respective redox reaction in an SRFB is emphasized along with supporting experimental evidence. The key advancement of the present work is the incorporation of realistic losses and assumptions based on the experimental studies in the field. The optimum solar-to-chemical efficiency is shown to shift significantly in the efficiency landscape depending on the kinetic overpotential, electrolyte resistance, state-of-charge and compartment architecture (*i.e.*, front- or backside illumination).

The model used in this work identifies these trends and shows that in addition to reducing the respective losses in an SRFB, photo-absorber/redox-couple matching should be carried out carefully for maximizing the obtainable STC efficiency for a single absorber system. A baseline single absorber SRFB system can achieve a maximum STC efficiency of ~18%, which decreases with increasing SOC at a certain E_g and cell voltage (*i.e.*, thermodynamic potential). This value surpasses the theoretical conversion efficiency for PEC water splitting (~11% for the single-absorber case) owing to the flexibility of the redox potential design and relatively fast redox kinetics. As the field explores new and higher performance materials (*e.g.*, additives for increasing the solution conductivity, non-Pt conducting materials with higher conductivity, *etc.*), our model indicates that higher STC efficiencies (>20%) can be achieved.

Although this model is a strong tool to identify general trends and sensitivities, the accuracy and predicted value could be increased by including certain effects, for instance, the photo-redox effect which has not been considered in this study. Furthermore, implementation of the dynamic overpotential as a function of the current density and mass-transport phenomena, which are governed by the Butler–Volmer model, can enhance the accuracy of the model further.

To aid further development of the field, we suggest here a range of recommendations that can be undertaken to make SRFB development competitive with other solar utilization systems:

- Back-side illumination is highly recommended unless there is no significant overlap between the light absorption spectra of the chosen electrolyte and photo-absorber, and no anti-reflective layer is needed.
- It is necessary that the electrolyte has a sufficiently low resistance (<2.5 Ω cm^2) such that implementation of commercially available, mature, but low band-gap PV materials, such as Si and CIGSe, are possible.
- In the same manner, the overall distance between the electrodes should be minimized. For example, a reduction of 1 cm in distance corresponds to a reduction of ~50% of the solution resistance.
- Albeit forming a porous conducting layer with an extremely high surface area at the surface of a photoelectrode is technically possible, individual evaluation of intrinsic activity of the

conducting layer should be conducted in order to minimize the kinetic overpotential.

- In the case of wide band-gap materials, such as a-SiC and Fe_2O_3, which require redox couples with a quite high potential gap (>1.3 V) to obtain a feasible STC%, care must be taken to avoid the risk of having a competitive reaction (*e.g.*, water splitting).

Conflicts of interest

There are no conflicts to declare.

Acknowledgements

This work was supported by the LEaDing Fellowship grant from the European Union's Horizon 2020 research and Innovation Programme under the Marie Sklodowska-Curie grant agreement no. 707404. The authors also thank Dr Kristina Wedege and Dr D. N. Østedgaard-Munck at Aarhus University for assistance in preparing the carbon felt electrodes and redox flow cell operation, and Joost Middelkoop and Herman Schreuders at the MECS group of TU Delft for preparation of the flow cell and assistance with training for use of the vacuum deposition system.

References

1 Key electricity trends 2017 based on monthly data, 2018.
2 P. C. K. Vesborg and B. Seger, *Chem. Mater.*, 2016, **28**, 8844–8850.
3 D. Bae, B. Seger, P. C. K. Vesborg, O. Hansen and I. Chorkendorff, *Chem. Soc. Rev.*, 2017, **46**, 1933–1954.
4 I. A. Digdaya, G. W. P. Adhyaksa, B. J. Trześniewski, E. C. Garnett and W. A. Smith, *Nat. Commun.*, 2017, **8**, 15968.
5 S. Ardo, D. Fernandez Rivas, M. A. Modestino, V. Schulze Greiving, F. F. Abdi, E. Alarcon Llado, V. Artero, K. Ayers, C. Battaglia, J. P. Becker, D. Bederak, A. Berger, F. Buda, E. Chinello, B. Dam, V. Di Palma, T. Edvinsson, K. Fujii, H. Gardeniers, H. Geerlings, S. M. Hashemi, S. Haussener, F. Houle, J. Huskens, B. D. James, K. Konrad, A. Kudo, P. P. Kunturu, D. Lohse, B. Mei, E. L. Miller, G. F. Moore, J. Muller, K. L. Orchard, T. E. Rosser, F. H. Saadi, J. W. Schüttauf, B. Seger, S. W. Sheehan, W. A. Smith, J. Spurgeon, M. H. Tang, R. Van De Krol, P. C. K. Vesborg and P. Westerik, *Energy Environ. Sci.*, 2018, **11**, 2768–2783.
6 H.-W. Nam, *The Korean Times*, 2018.
7 X. Liu, D. Ren, H. Hsu, X. Feng, G. L. Xu, M. Zhuang, H. Gao, L. Lu, X. Han, Z. Chu, J. Li, X. He, K. Amine and M. Ouyang, *Joule*, 2018, **2**, 2047–2064.
8 N. S. Lewis, *Science*, 2016, **351**, aad1920.
9 W. Li, H.-C. Fu, L. Li, M. Cabán-Acevedo, J.-H. He and S. Jin, *Angew. Chem., Int. Ed.*, 2016, **55**, 13104–13108.
10 Q. Cheng, W. Fan, Y. He, P. Ma, S. Vanka, S. Fan, Z. Mi and D. Wang, *Adv. Mater.*, 2017, **29**, 1700312.
11 K. Wedege, D. Bae, W. A. Smith, A. Mendes and A. Bentien, *J. Phys. Chem. C*, 2018, **122**, 25729–25740.
12 E. H. Calderon, A. Katsaounis, R. Wüthrich, P. Mandin, G. Foti and C. Comninellis, *J. Appl. Electrochem.*, 2009, **39**, 1827–1833.
13 M. Uhrig, S. Koenig, M. R. Suriyah and T. Leibfried, *Energy Procedia*, 2016, **99**, 35–43.
14 M. Paiss, *Energy Storage System Safety*, 2017.
15 W. Wang, Q. Luo, B. Li, X. Wei, L. Li and Z. Yang, *Adv. Funct. Mater.*, 2013, **23**, 970–986.
16 J. Wang, K. Lu, L. Ma, J. Wang, M. Dooner, S. Miao, J. Li and D. Wang, *Energies*, 2017, **10**, 991.
17 G. Hodes, J. Manassen and D. Cahen, *Nature*, 1976, **261**, 403–404.
18 F. Urbain, S. Murcia-López, N. Nembhard, J. Vázquez-Galván, C. Flox, V. Smirnov, K. Welter, T. Andreu, F. Finger and J. R. J. R. Morante, *J. Phys. D: Appl. Phys.*, 2019, **52**, 044001.
19 K. Wedege, D. Bae, E. Dražević, A. Mendes, P. C. K. Vesborg and A. Bentien, *RSC Adv.*, 2018, **8**, 6331–6340.
20 S. Liao, X. Zong, B. Seger, T. Pedersen, T. Yao, C. Ding, J. Shi, J. Chen and C. Li, *Nat. Commun.*, 2016, **7**, 11474.
21 G. Kim, M. Oh and Y. Park, *Sci. Rep.*, 2016, 1–9.
22 J. R. McKone, F. J. DiSalvo and H. D. Abruña, *J. Mater. Chem. A*, 2017, **5**, 5362–5372.
23 M. Park, J. Ryu, W. Wang and J. Cho, *Nat. Rev. Mater.*, 2016, **2**, 1–18.
24 K. Wedege, J. Azevedo, A. Khataee, A. Bentien and A. Mendes, *Angew. Chem., Int. Ed.*, 2016, **55**, 7142–7147.
25 I. M. Peters, S. Sofia, J. Mailoa and T. Buonassisi, *RSC Adv.*, 2016, **6**, 66911–66923.
26 Z. J. Yu, J. V. Carpenter and Z. C. Holman, *Nat. Energy*, 2018, **3**, 747–753.
27 B. Keita and L. Nadjo, *J. Electroanal. Chem.*, 1984, **163**, 171–188.
28 B. Keita and L. Nadjo, *J. Electroanal. Chem.*, 1983, **151**, 283–288.
29 Y. Zhou, S. Zhang, Y. Ding, L. Zhang, C. Zhang, X. Zhang, Y. Zhao and G. Yu, *Adv. Mater.*, 2018, **30**, 1–7.
30 W. D. McCulloch, M. Yu and Y. Wu, *ACS Energy Lett.*, 2016, **1**, 578–582.
31 P. G. P. Ang and A. F. Sammells, *Faraday Discuss. Chem. Soc.*, 1980, **70**, 207–222.
32 M. F. Weber, *J. Electrochem. Soc.*, 1984, **131**, 1258.
33 B. Seger, O. Hansen and P. C. K. Vesborg, *Sol. RRL*, 2017, **1**, e201600013.
34 J. D. Benck, L. C. Seitz, B. A. Pinaud, T. F. Jaramillo, A. J. Forman and Z. Chen, *ChemSusChem*, 2014, **7**, 1372–1385.
35 H. Döscher, J. F. Geisz, T. G. Deutsch and J. a. Turner, *Energy Environ. Sci.*, 2014, **7**, 2951–2956.
36 R. Ye, D. Henkensmeier, S. J. Yoon, Z. Huang, D. K. Kim, Z. Chang, S. Kim and R. Chen, *J. Electrochem. Energy Convers. Storage*, 2017, **15**, 010801.
37 G. O. Phillips, N. W. Worthington, J. F. McKeller and R. R. Sharpe, *J. Chem. Soc. A*, 1969, 767–773.
38 E. A. Gibson, L. Le Pleux, J. Fortage, Y. Pellegrin, E. Blart, F. Odobel, A. Hagfeldt and G. Boschloo, *Langmuir*, 2012, **28**, 6485–6493.

39 W. Shockley and H. J. Queisser, *J. Appl. Phys.*, 1961, **32**, 510–519.

40 M. A. Green, *Third Generation Photovoltaics – Advanced Solar Energy Conversion*, Springer, Heidelberg, 2008.

41 P. M. Cuce and E. Cuce, *Int. J. Low-Carbon Technol.*, 2012, **7**, 159–165.

42 C. Flox, S. Murcia-López, N. M. Carretero, C. Ros, J. R. Morante and T. Andreu, *ChemSusChem*, 2018, **11**, 125–129.

43 K. Wedege, J. Azevedo, A. Khataee, A. Bentien and A. Mendes, *Angew. Chem., Int. Ed.*, 2016, **55**, 7142–7147.

44 D. Liu, Z. Wei, C. J. Hsu, Y. Shen and F. Liu, *Electrochim. Acta*, 2014, **136**, 435–441.

45 T. Frijnts, S. Kühnapfel, S. Ring, O. Gabriel, S. Calnan, J. Haschke, B. Stannowski, B. Rech and R. Schlatmann, *Sol. Energy Mater. Sol. Cells*, 2015, **143**, 457–466.

46 M. A. Green, *Sol. Energy Mater. Sol. Cells*, 2008, **92**, 1305–1310.

47 S. Correiaa, J. Lossena, M. Bährb and E. S. S. E. Ag, *Sol. Cells*, 2006, **2**, 1–4.

48 L. Ma, L. Xu, K. Zhang, W. Wu and Z. Ma, *2011 Int. Conf. Electr. Control Eng. ICECE 2011 – Proc.*, 2011, pp. 2711–2714.

49 D. Bae, J. Gho, M. Shin and S. Kwon, *Thin Solid Films*, 2013, **535**, 162–165.

50 D. Bae, T. Pedersen, B. Seger, M. Malizia, A. Kuznetsov, O. Hansen, I. Chorkendorff and P. C. K. Vesborg, *Energy Environ. Sci.*, 2015, **8**, 650–660.

51 D. Bae, T. Pedersen, B. Seger, B. Iandolo, O. Hansen, P. C. K. Vesborg and I. Chorkendorff, *Catal. Today*, 2017, **290**, 59–64.

52 D. Bae, B. Seger, O. Hansen, P. C. K. Vesborg and I. Chorkendorff, *ChemElectroChem*, 2019, **6**, 106–109.

53 A. Polman, M. Knight, E. C. Garnett, B. Ehrler and W. C. Sinke, *Science*, 2016, **352**, aad4424.

54 N. H. Choi, S. Kwon and H. Kim, *J. Electrochem. Soc.*, 2013, **160**, A973–A979.

55 X. T. Yang, X. S. Chai, Q. X. Hou, J. Y. Zhu and L. G. Danielsson, *Anal. Chim. Acta*, 2002, **474**, 69–76.

56 J. M. Gardner, M. Abrahamsson, B. H. Farnum and G. J. Meyer, *J. Am. Chem. Soc.*, 2009, **131**, 16206–16214.

57 M. F. Stuckings and A. W. Blakers, *Sol. Energy Mater. Sol. Cells*, 1999, **59**, 233–242.

58 P. A. Lasselle and J. G. Aston, *J. Am. Chem. Soc.*, 1933, **55**, 3067–3071.

59 C. R. C. Handbook, C. R. C. Press, B. Raton, A. Solutions and B. Fluids, *Handb. Chem. Physics*, CRC Press, 95th edn, 1989, p. 178.

60 G. Jones and F. C. Jelen, *J. Am. Chem. Soc.*, 1936, **58**, 2561–2565.

61 W. M. Haynes, *CRC Handbook of Chemistry and Physics*, 95th edn, 2014–2015, CRC Press, 95th edn, 2014.

62 M. G. Mali, H. Yoon, B. N. Joshi, H. Park, S. S. Al-Deyab, D. C. Lim, S. Ahn, C. Nervi and S. S. Yoon, *ACS Appl. Mater. Interfaces*, 2015, **7**, 21619–21625.

63 T. Sawant and J. McKone, ChemRxiv, DOI: 10.26434/chemrxiv.6203297.v1.

64 S. Mubeen, J. Lee, N. Singh, M. Moskovits and E. W. McFarland, *Energy Environ. Sci.*, 2013, **6**, 1633.

65 O. Scialdone, C. Guarisco, S. Grispo, A. D. Angelo and A. Galia, *J. Electroanal. Chem.*, 2012, **681**, 66–75.